Håkon Dahle
Ole Kristian Rønning

Thermomechanical Response of Virgin and Degraded PA11

Master's thesis in Civil and Environmental Engineering
Supervisor: Arild Holm Clausen
June 2019

Master's thesis

NTNU
Norwegian University of Science and Technology
Faculty of Engineering
Department of Structural Engineering

NTNU
Norwegian University of
Science and Technology

Håkon Dahle
Ole Kristian Rønning

Thermomechanical Response of Virgin and Degraded PA11

Master's thesis in Civil and Environmental Engineering
Supervisor: Arild Holm Clausen
June 2019

Norwegian University of Science and Technology
Faculty of Engineering
Department of Structural Engineering

NTNU
Norwegian University of
Science and Technology

Department of Structural Engineering
Faculty of Engineering
NTNU - Norwegian University of Science and Technology

Accessibility:
Limited

MASTER THESIS 2019

Subject area:	Date:	Number of pages:
Computational mechanics	6th of June 2019	19+95+28

Title:

Thermomechanical Response of Virgin and Degraded PA11

Termomekanisk respons av ubrukt og degradert PA11

By:

Håkon Dahle

Ole Kristian Rønning

Summary:

In this thesis, experimental and numerical studies of polyamide 11 (PA11) have been carried out to address the thermomechanical behavior under triaxial stress states and the effects of material degradation. PA11 is a semi-crystalline thermoplastic, which is commonly used as liners in flexible risers for transporting oil and gas.

The virgin and degraded material has been examined through tensile tests with and without notches at room temperatures and at -20°C. Additionally, tension tests with different strain rates and compression tests were conducted. Elastic and plastic material parameters have been analytically identified and optimized through numerical simulations and visual inspection. Furthermore, assumptions regarding strain rate and pressure sensitivity have been studied.

The virgin and degraded specimens showed different mechanical behavior. Degraded PA11 with a reduction of plasticizer content and molecular weight made the test specimens stiffer, increased the tensile strength, and decreased the ductility. Moreover, a global softening effect and a loss of the locking effect were seen from the degraded test results. Furthermore, an increase in volumetric strain and a whitening effect of the fracture surface indicated void growth. Void growth may be the reason for the increased fracture tendency of the degraded materials.

Under all test conditions, the stress triaxiality had a significant impact on the behavior of PA11. A smaller notch radius increased the damage in the specimen. The volumetric strain increased with a decreasing notch radius and should be considered a damage mechanism due to the indications of void growth. Further, for small notch radiuses, the test specimen behaved more brittle as a component, but locally it still behaved highly ductile. Hence, the presence of triaxial stress states and chemical agents challenge the structural integrity of flexible risers.

Non-linear finite element simulations were done using Abaqus together with the SIMLab Polymer Model. A unique material model has been established for each material variation under cold and warm conditions. Common tendencies across the material models were that the response was either too soft for the specimens with low triaxiality or too stiff for the specimens with high triaxiality. The diameter reduction was too low for the specimens with low triaxiality. The discrepancy in diameter reduction was due to the plastic dilation being independent of the stress state in the model. This independence was the greatest weakness of the conducted simulations.

Responsible teacher: Professor Arild Holm Clausen

Supervisors: Professor Arild Holm Clausen, PhD Candidate Sindre Nordmark Olufsen and PhD Candidate Einar Schwenke

Carried out at: Department of Structural Engineering, NTNU

NORGES TEKNISK-NATURVITENSKAPELIGE UNIVERSITET
INSTITUTT FOR KONSTRUKSJONSTEKNIKK

MASTER THESIS 2019

Håkon Dahle og Ole Kristian Rønning

Thermomechanical response of PA11

(Termomekanisk respons av PA11)

At least 50% of the oil production in Norway depends on flexible pipes and risers. The pressure in such structures is held by the polymer liner made of PA11. The liner in flexible pipes and risers is locked between two steel layers (carcass and pressure armour) and is subject to multiaxial stresses.

The thesis work will involve a typical PA11 material taken from a flexible pipe. The candidate is supposed to do the required material tests on this PA11 in order to calibrate the material model. As most polymers are pressure sensitive, it is of particular interest to evaluate states with increased stress triaxiality. A common way to do this is to apply notched samples. Subsequently, the calibrated model is to be validated against laboratory tests on an appropriate sample. If time allows, it is also of interest to compare the numerical predictions with those obtained with a different material model.

An important governing mechanism for plastic deformation and ductile failure of polymers is formation of voids and subsequent void growth, leading to an increase of the volume. This feature can be further explored by X-ray computer tomography (CT). Provided that an *in situ* tension test rig adapted to the CT apparatus is available, such tests are also relevant to incorporate in the master's thesis.

Possible keywords for activities in this master thesis research work may include:

- Literature review: Polymeric materials, material models.
- Experimental work: Material tests, *in situ* CT tests and validation tests. Presentation of test results.
- Numericial model: Calibration of material model. Modelling and simulation of material tests.
- Validation: Comparison of experimental and numerical results. Evaluation of the model. Comparison with results obtained with other material models.

The candidate may agree with the supervisors to pay particular attention to specific parts of the investigation, or include other aspects than those already mentioned.

The thesis is to be organized as a research report, recognising the guidelines provided by Department of Structural Engineering.

Supervisor at NTNU: Arild Holm Clausen, Einar Schwenke, Sindre Olufsen

The report is to be handed in no later than 11 June 2019.

NTNU, 23 January 2019

Arild Holm Clausen

Abstract

In this thesis, experimental and numerical studies of polyamide 11 (PA11) have been carried out to address the thermomechanical behavior under triaxial stress states and the effects of material degradation. PA11 is a semi-crystalline thermoplastic, which is commonly used as liners in flexible risers and pipes for transporting oil and gas.

The virgin and degraded material has been examined through tensile tests with and without notches at room temperatures and at -20°C. Additionally, tension tests with different strain rates and compression tests were conducted. Elastic and plastic material parameters have been analytically identified and optimized through numerical simulations and visual inspection. Furthermore, assumptions regarding strain rate and pressure sensitivity have been studied.

The virgin and degraded specimens showed different mechanical behavior. Degraded PA11 with a reduction of plasticizer content and molecular weight made the test specimens stiffer, increased the tensile strength, and decreased the ductility. Moreover, a global softening effect and a loss of the locking effect were seen from the degraded test results. Furthermore, an increase in volumetric strain and a whitening effect of the fracture surface indicated void growth. Void growth may be the reason for the increased fracture tendency of the degraded materials.

Under all test conditions, the stress triaxiality had a significant impact on the behavior of PA11. A smaller notch radius increased the damage in the specimen. The volumetric strain increased with a decreasing notch radius and should be considered a damage mechanism due to the indications of void growth. Further, for small notch radiuses, the test specimen behaved more brittle as a component, but locally it still behaved highly ductile. Hence, the presence of triaxial stress states and chemical agents challenge the structural integrity of flexible risers.

Non-linear finite element simulations were done using Abaqus together with the SIMLab Polymer Model. A unique material model has been established for each material variation under both cold and warm conditions. Common tendencies across the material models were that the response was either too soft for the specimens with low triaxiality or too stiff for the specimens with high triaxiality. The diameter reduction was too low for the specimens with low triaxiality. The discrepancy in diameter reduction was due to the plastic dilation being independent of the stress state in the material model. This independence was the greatest weakness of the conducted simulations.

Sammendrag

I denne masteroppgaven har det blitt gjennomført eksperimentelle og numeriske studier på polyamid 11 (PA11). Arbeidet er utført for å undersøke den termomekaniske oppførselen ved varierende grad av triaksiel spenningstilstand og effekten av materialnedbrytning. PA11 er en semi-krystallinsk termoplast som blir brukt i fleksible olje- og gassrør.

Det ubrukte og nedbrutte materialet har blitt undersøkt ved gjennomføring av strekktester på aksesymmetriske prøvestykker, med og uten kjerv, ved romtemperatur og -20°C. I tillegg har strekktester med forskjellige tøyningshastigheter og trykktester blitt gjennomført på det ubrukte materialet. Elastiske og plastiske materialparametere har blitt funnet analytisk og deretter optimalisert gjennom numeriske simuleringer og visuell inspeksjon. Antagelser i materialmodellen angående tøyningsrate- og trykksensitivitet har blitt undersøkt.

De ubrukte og nedbrutte prøvestykkene viste forskjellig mekanisk oppførsel. En reduksjon i myknerinnhold og molekylær vekt gjorde prøvestykkene stivere, økte styrken i strekk og reduserte duktiliteten. Dessuten ble en global mykningseffekt og et tap av låsningsoppførselen observert i de degraderte prøvestykkene. Det ble observert blekning av bruddflaten og økte volumtøyninger etter degradering. Disse observasjonene indikerer porevekst og kan være grunnen til den økte bruddtendensen for degraderte prøvestykker.

Spenningstriaksialitet hadde et vesentlig utslag på oppførselen til PA11. For kortere kjervradier oppførte prøvestykkene seg sprøere som komponenter, men fremdeles duktile lokalt. En kortere kjervradius økte skaden i prøvestykket. Skademekanismen kommer sannsynlighvis av økt porvekst som er blitt indikert av økte volumtøyninger ved kortere kjervradius. Funnene i denne oppgaven konkluderer at tilstedeværelsen av fleraksielle spenningstilstander og kjemiske midler i fleksible rør er en utfordring for rørenes konstruksjonsstyrke.

Ikkelineære elementanalyser ble gjort i Abaqus sammen med SIMLab Polymer Model. En unik materialmodell ble laget for alle materialvariantene ved varme og kalde forhold. Observerte tendenser på tvers av materialmodellene var at spenningen enten var for myk for prøvestykkene med lite triaksialitet eller for stiv for prøvestykkene med høy triaksialitet. Diameterreduksjonen var for lav for prøvestykkene med lite triaksialitet. Uovernsstemmelsen av diameterreduksjonen skyldtes at plastisk utvidelse var uavhengig av spenningstilstanden i materialmodellen. Mangel på denne avhengigheten var den største svakheten ved simuleringene.

Preface

This master thesis is the result of work done in the spring of 2019, as the final part of the five-year master's degree program Civil and Environmental Engineering. The thesis is written for and carried out at the Departement for Structural Engineering at the Norwegian University of Science and Technology in Trondheim, Norway. The primary supervision has been provided by the Head of Programme Polymeric Materials, Professor Arild Holm Clausen.

The topic for this thesis was chosen because of an interest in how polymeric materials behave, which was mainly unknown for both of us, as well as an interest in experimental work and numerical modeling.

Acknowledgements

We want to express our gratitude to our supervisor, Professor Arild Holm Clausen, for his guidance and support, which has been above and beyond what was expected of him. His enthusiasm and knowledge have been a great help to us. We also want to thank PhD Candidate Sindre Nordmark Olufsen for being available for educational discussions, helping us perform CT-scans and making sense of odd results. The experimental work has been carried out with the help of Senior Engineer Trond Auestad, who we are grateful to for providing us with his expertise, time, and knowledge. We also want to thank PhD Candidate Einar Schwenke, Researcher Torodd Berstad and Associate Professor David Morin for helping us and being available for questions.

This project has been performed in cooperation with Equinor, which has provided the material, performed the degradation procedures, and has been easy to get in touch with for questions. We would especially express our gratitude to Per Nygård.

We also want to thank each other for great collaboration and our families for their support.

Contents

Nomenclature **xvii**

Abbreviations **xix**

I Introdcution **2**

1 Introduction **4**

1.1 Background 5

1.2 Objective 5

1.3 Scope 5

1.4 Thesis Layout 6

2 Theoretical Background **7**

2.1 Material Behavior of Polymers 7

2.1.1 Structure of Polymers 7

2.1.2 Mechanical Properties 9

2.2 SIMLab Polymer Model 13

2.2.1 General Formulation 13

2.2.2 Elasticity and Plasticity 13

2.3 Extended Drucker-Prager Material Model 17

2.4 Digital Image Correlation 18

2.5 CT-Scanning 18

3 Material and Degradation **20**

3.1 The Material Used in This Study: Polyamide 11 20

3.2 Degradation Procedures and Goals 21

3.2.1 Procedure 1 - Reduction of Plasticizer Content (P) 21

3.2.2 Procedure 2 - Reduction of Plasticizer Content and Molecular Weight (PW) 21

3.2.3 Procedure 3 - Reduction of Molecular Weight 22

II Experimental Work and Calibration 24

4 Material Testing 26

4.1 General Experimental Setup for Tension and Compression Tests 26
4.2 Post-Processing 31
4.3 Uniaxial Tension and Compression Results 34
4.3.1 Effect of Notch Radius 35
4.3.2 Effect of Temperature 37
4.3.3 Effect of Nominal Strain Rates 39
4.3.4 Effect of Degrading 40
4.3.5 Compression Tests 44
4.4 CT-Scanning 45
4.5 Sources of Error 47
4.6 Discussion and Conclusion 48

5 Calibration 50

5.1 Abaqus Model 50
5.2 Calibration of the SIMLab Polymer Model 53
5.2.1 General Calibration Procedure 54
5.2.2 Virgin PA11 (V-H) 57
5.2.3 PA11 with Reduced Plasticizer Content (P-H) 61
5.2.4 PA11 with Reduced Plasticizer Content and Reduced Molecular Weight (PW-H) 62
5.2.5 PA11 with Reduced Molecular Weight (W-H) 63
5.2.6 Virgin PA11 at -20°C (V-C) 64
5.2.7 PA11 with Reduced Plasticizer Content at -20°C (P-C) 65
5.2.8 PA11 with Reduced Plasticizer Content and Molecular Weight at -20°C (PW-C) 66
5.3 Calibration of the Drucker-Prager Model for Virgin PA11 (V-H) 67
5.4 Sources of Error 68
5.5 Discussion and Conclusion 68

III Validation and Conclusion **72**

6 Validation: Numerical Simulation **74**

6.1 Validation of the SIMLab Polymer Model 74

6.1.1 Virgin PA11 (V-H) 74

6.1.2 PA11 with Reduced Plasticizer Content (P-H) 77

6.1.3 PA11 with Reduced Plasticizer Content and Molecular Weight (PW-H) . 78

6.1.4 PA11 with Reduced Molecular Weight (W-H) 79

6.1.5 Virgin PA11 at -20°C (V-C) 80

6.1.6 PA11 with Reduced Plasticizer Content at -20°C (P-C) 81

6.1.7 PA11 with Reduced Plasticizer Content and Molecular Weight at -20°C (PW-C) 82

6.2 Validation of the Drucker-Prager Model for Virgin PA11 (V-H) 83

6.3 Validation of the Abaqus Model 84

6.4 Sources of Error 86

6.5 Discussion and Conclusion 87

7 Conclusion and Further Work **88**

7.1 Conclusion 88

7.2 Recommended Further work 89

References **92**

A Appendix **A-1**

Nomenclature

A_0	Initial area
A_C	Current area
C	Rate sensitivity
D_0	Initial diameter
D_C	Current diameter
E	Young's modulus
F	Force
α	Pressure sensitivity parameter
β	Plastic dilation parameter
ε_L	Log. longitudinal strain
ε_T	Log. transverse strain
ε_V	Log. volumetric strain
$\dot{\varepsilon}$	Nominal strain rate
ε_L^p	Log. longitudinal plastic strain
ε_T^p	Log. transverse plastic strain
p	Equivalent plastic strain
$\dot{p}$	Equivalent plastic strain rate
$\dot{p}_0$	Reference equivalent plastic strain rate
σ_y	Yield stress
σ_T	Uniaxial tension yield stress
σ_C	Uniaxial compression yield strength
σ	True stress
σ_0	Nominal stress
ν	Poisson's ratio

$\hat{\boldsymbol{\sigma}}$	Corotaional stress tensor
$\boldsymbol{\sigma}$	Cauchy stress tensor
$\dot{\hat{\boldsymbol{\sigma}}}$	Time derivative of the stress tensor
$\mathbf{D}$	Deformation rate tensor
$\hat{\mathbf{D}}$	Corotational deformation rate tensor
$\mathbf{D}^e$	Elastic deformation rate tensor
$\mathbf{D}^p$	Plastic deformation rate tensor
$\mathfrak{D}_{vp}$	Visco-plastic dissipation per unit volume
$\mathfrak{D}_i$	Inelastic dissipation per volume
$\mathbf{R}$	Rotation tensor
$\hat{\mathbf{C}}^\sigma$	Elasticity tensor
$\hat{\mathbf{S}}^\sigma$	Flexibility tensor
$f(\hat{\boldsymbol{\eta}}, R)$	Yield function of the SPM
$\hat{\boldsymbol{\eta}}$	Corotational overstress
$\hat{\boldsymbol{\chi}}$	Corotational backstress
$\varphi(\hat{\boldsymbol{\eta}})$	Raghava yield function
g	Flow potential
R	Isotropic hardening
θ_{Ri}	Initial hardening modulus
Q_{Ri}	Saturation value of the term R_i
F_{DP}	Yield criterion for Drucker-Prager
β_{DP}	Friction angle
q	Mises equivalent stress
r	Third stress invariant
d	Cohesion
a	Material parameter (Drucker-Prager)
b	Material parameter (Drucker-Prager)
K	Ratio between triaxial tension and compression yield stress

Abbreviations

PA11	Polyamide 11
V	Virgin polyamide 11
P	Degraded polyamide 11 with reduced plasticizer content
W	Degraded polyamide 11 with reduced molecular weight
PW	Degraded polyamide 11 with reduced molecular weight and reduced plasticizer content
S	Smooth specimen
R20	Specimen with a notch radius of 20mm
R5	Specimen with a notch radius of 5mm
R2	Specimen with a notch radius of 2mm
Cy	Cylindric specimen
H	Experiment at room temperature
C	Experiment at -20°C
Ra2	Experiment with nominal strain rate of $10^{-2}s^{-1}$
Ra3	Experiment with nominal strain rate of $10^{-1}s^{-1}$
SPM	SIMLab Polymer Model
DP	Drucker-Prager
FEA	Finite element analysis
DIC	Digital image correlation
eCorr	A software for DIC analyses
CT	Computed Tomography
BESNO P40TL	Polyamide 11 produced by Rilsan (Arkema)
CIV	Corrected inherent viscosity
ESV	Plasticizer content
XRF	X-ray fluorescence
SIMLab	The Structural Impact Laboratory
NTNU	The Norwegian University of Science and Technology
CASA	Center for Advanced Structural Analysis

Part I

Introdcution

1 Introduction

In 2013 there were over 300 flexible risers responsible for secure transport of oil and gas outside the Norwegian coast (4Subsea 2013). These structures transport the oil and gas from the bottom of the sea to the surface, and in certain situations from the surface to the seabed. The structure of these risers consists of a polymer sheath located between the inner carcass and a pressure armor. This liner is often made of polyamide 11 (PA11), a semi-crystalline thermoplastic, which is subjected to various stress states, including multiaxial stresses. Additionally, the pressure sheath is subjected to extreme conditions, i.e., high temperature, dynamic loads, and degrading processes. Because of this, and a lack of understanding of the material's behavior at these conditions, the rate of failure has increased steadily from 1995 till 2013 (4Subsea 2013).

The size of flexible risers varies, but in general, they are too large to test in terms of time and economy. Therefore, simulations and numerical models as a tool to predict the behavior of these risers have become a priority for operators, such as Equinor. The Structural Impact Laboratory (SIMLab) at NTNU has developed a constitutive model for polymers, but finite element analyses of polymers is a rather new area of focus. Thus, the models are less refined than others, e.g., metals.

The main focus of this master thesis is to conduct mechanical testing on virgin and degraded PA11 specimens, with and without notches, at room temperature and -20°C. The results from these tests will subsequently be used to calibrate the mechanical properties of the material to establish a numerical model for the different variations of degradation and temperature. Tension tests with different strain rates and compression tests will also be conducted to calibrate the material model and as a control of the underlying model assumptions. Further, the numerical models will be validated against a specimen with a different stress state. The mechanical testing will consist mainly of tensile testing of notched and smooth specimens, and compression tests of smooth cylinders. If substantial volume growth is observed, in-situ CT-scans of the tension tests will be performed to determine if the volume growth is a result of the formation and growth of voids.

The materials that will be tested are virgin PA11, PA11 with reduced plasticizer content, PA11 with reduced molecular weight, and PA11 with both reduced molecular weight and plasticizer content. All the specimens are cut out from a part of an unused pipe supplied by Equinor,

before the degradation process and testing have been performed. Both the calibration and validation will be done in Abaqus to further understand the capabilities and limitations of the SIMLab Polymer Model.

1.1 Background

SIMLab is located at the Department of Structural Engineering, NTNU, and hosts the Centre for Advanced Structural Analysis (CASA). SIMLab's objective is to understand how materials, e.g., polymers, metals, and glass, work under extreme conditions. The program for polymers at SIMLab has as objective to develop computer models which can be used to simulate different polymer's behavior. This is a motivation for Equinor, which is one of CASA's partners, to engage in this project. SIMLab's motivation for this thesis is a continuation of testing the capabilities and limitations of the SIMLab Polymer Model (SPM). Herein the ability to simulate models with a different degree of triaxiality at different temperatures. Another motivator is the possibility of a successful in-situ CT-scan, which will be able to capture void growth in a specimen during a tensile test, which has not been done before.

1.2 Objective

This thesis concerns experimental and numerical studies of PA11. The objectives of the research are:

- To conduct experimental tests of PA11 specimens, both virgin and degraded, with different degrees of triaxiality at room temperature and at -20°C.
- To conduct in-situ CT-scans of tension tests.
- To explore the limitations and capabilities of the SPM by numerical simulations of the experimental tests.

1.3 Scope

The scope set for this thesis has been done in collaboration with the involved actors of this thesis. Four different materials will be tested, virgin PA11 and three degraded variations of

PA11, at room temperature and at -20°C. The specimens are limited to three notched specimens with different notch radius, i.e., 2 mm, 5 mm and 20 mm, a smooth specimen, and a cylinder. Most of the tests have only been performed once for each variation. Almost all the tests have had a quasi-static strain rate, except for the ones to explore the effects of strain rate on the virgin material. Neither damage nor strain rate is taken into account in the simulations. Lastly, creep is not considered.

1.4 Thesis Layout

The thesis has three parts. Part I, Introduction, is an introduction to the thesis and contains three chapters. Chapter 1 gives an introduction by presenting the background, the objective, the limitations, and the structure of the thesis. Chapter 2 introduces the theory applied. The material used in this thesis, along with the different degraded variations, is presented in Chapter 3.

Part II, Experimental Work and Calibration, contains two chapters. Chapter 4 presents the experimental work and its results, along with a discussion and possible errors of the results. Chapter 5 presents the process of calibrating the material parameters used in the numerical models and discusses the results and possible errors.

Part III, Validation and Conclusion, contains two chapters as well. Chapter 6 presents the work done to validate the numerical models established. Chapter 7 concludes this thesis and suggests further work.

2 Theoretical Background

This chapter introduces the relevant theory to understand the obtained results, the models created, the discussions and the conclusions presented in this thesis.

2.1 Material Behavior of Polymers

The mechanical properties and structure of polymers are presented in this section.

2.1.1 Structure of Polymers

A polymer is a chemical compound made up of many molecules bonded together in long, repeating chains. These types of materials can be natural (found in nature) or synthetic (human-made). Cellulose and DNA are examples of natural polymers, while polytetrafluoroethylene (teflon) and polyamide (nylon) are examples of synthetic polymers. Polymers have a complex structure since they consist of several thousand molecule units, which are organized in an extensive network of chains. Most commonly do chains consist of a strong backbone of carbon atoms with covalent bonds. These carbon atoms can also have different kind of side groups attached to them. These side groups can be atoms, groups of atoms, or another attached polymer chain. Hence, there exist several different types of polymers. A typical classification of polymers is by; thermal behavior, route of chemical synthesis, and structural organization.

Some polymers soften upon heating and can flow when stresses are applied. When cooled again, they can reversibly go back to their original solid or rubbery nature. These polymers are called thermoplastics and consist only of weak van der Waals bonds between the molecular chains. Not all polymers can reverse to their original nature after being heated. These polymers are called thermosets, due to the irreversible hardening from the curing reaction from the heating process.

The process of linking the molecules together into a covalent bonded chain or network is called polymerization. All molecules that can undergo polymerization are monomers, and several monomers bonded together result in a polymer chain. The most common polymerization mechanisms are condensation and addition processes. Under a condensation process, a small molecule (most often water) is split out. This is seen in Figure 2.1, where diamine reacts with a diacid,

which results in polyamide (nylon) and water. Under an addition process, the polymerization reaction involves the opening of a double bond, and no molecule is split out.

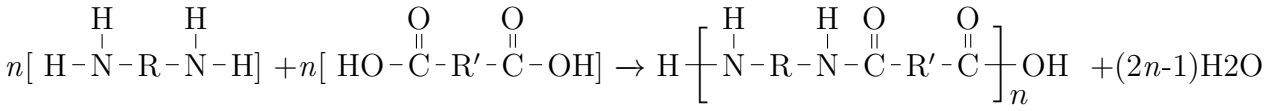

Figure 2.1: Schematic description of the condensation process of diamine and diacid, which results in polyamide and water.

Polymers can have different structural organizations depending on the alignment of the molecular chains. Polymers can have a crystal structure if the chains have high molecular regularity. The polymers are then called crystalline, and this structure is shown in Figure 2.2. The crystals have a lamellar structure of the polymer chains. Polymers with a low order of regularity in how the molecules are packed together are called amorphous. With such morphology, the chains are randomly distributed, as seen in Figure 2.2. In reality, polymers do not have fully crystalline or amorphous structures, but rather a mix of both. A common expression for crystalline polymers with amorphous regions is semi-crystalline polymers.

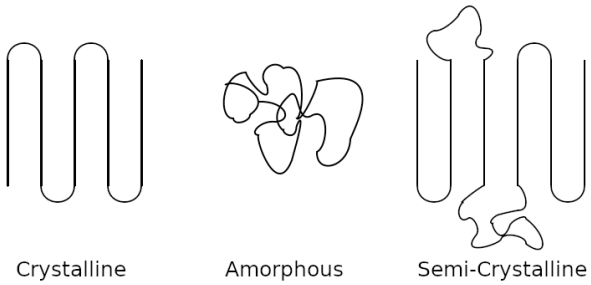

Figure 2.2: Schematic representation of different structural organizations depending on the alignment of the molecular chains (Robson 2018).

2.1.2 Mechanical Properties

Deformation of Thermoplastics

Some thermoplastics are characterized by being very ductile, which means exhibiting large elastic and plastic deformation (Polanco-Loria et al. 2010). The cause of the macroscopic deformation of thermoplastics is either because of the movement of polymer chains or movement of segment chains. The movement can be inter- or intramolecular, respectively meaning that the chains slide or change in the conformation of the chain (Ward 2004).

The deformation of thermoplastic polymers is dependent on the applied stress, strain rate, temperature, and pressure. When modeling the deformation, the deformation may be divided into one elastic and one plastic part. The elastic deformation is reversible, and the plastic deformation is irreversible.

The elastic properties are controlled by the intermolecular bonds between the chains, not the covalent bonds (Rösler et al. 2007). Elastic deformation of semi-crystalline polymers occurs at relatively low stress levels. Figure 2.3 shows the different stages in the elastic deformation of a semi-crystalline polymer (Callister Jr and Rethwisch 2012). The elastic deformation begins when the amorphous chains are elongated in the direction of the applied tensile stress. When the deformation continues, the lamellar crystalline thickness increases slightly due to bending and stretching of chains in crystalline regions. In the elastic phase, the van der Waals bonds between the chains are stretched, and the covalent chains in the amorphous region are elongated.

The transition from elastic to plastic deformation occurs when adjacent chains in the lamellae slide past one another. The plastic deformation results in tilting the lamellae, so the chains are more aligned with the tensile stress. Further deformation results in separation of crystalline block segments from the lamellae. The blocks will eventually be fully oriented with the tensile axis. The process of orientation is referred to as cold drawing and is known to improve the mechanical properties of the polymer. The plastic deformation process is visualized in Figure 2.4.

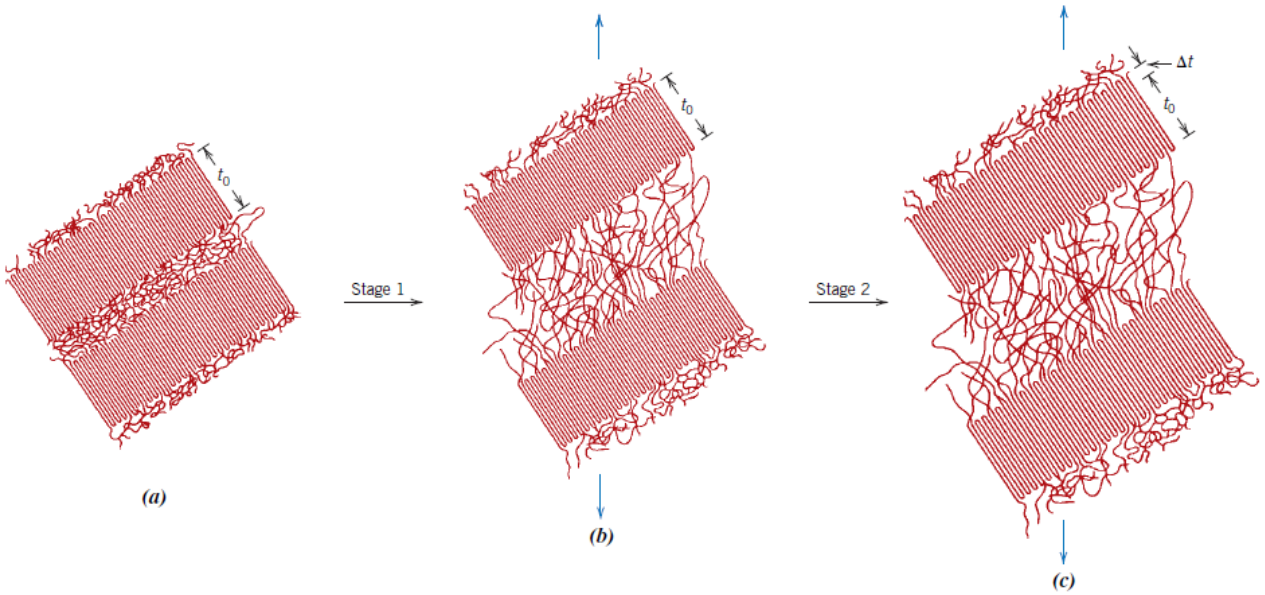

Figure 2.3: Elastic deformation of semi-crystalline polymers (Callister Jr and Rethwisch 2012).

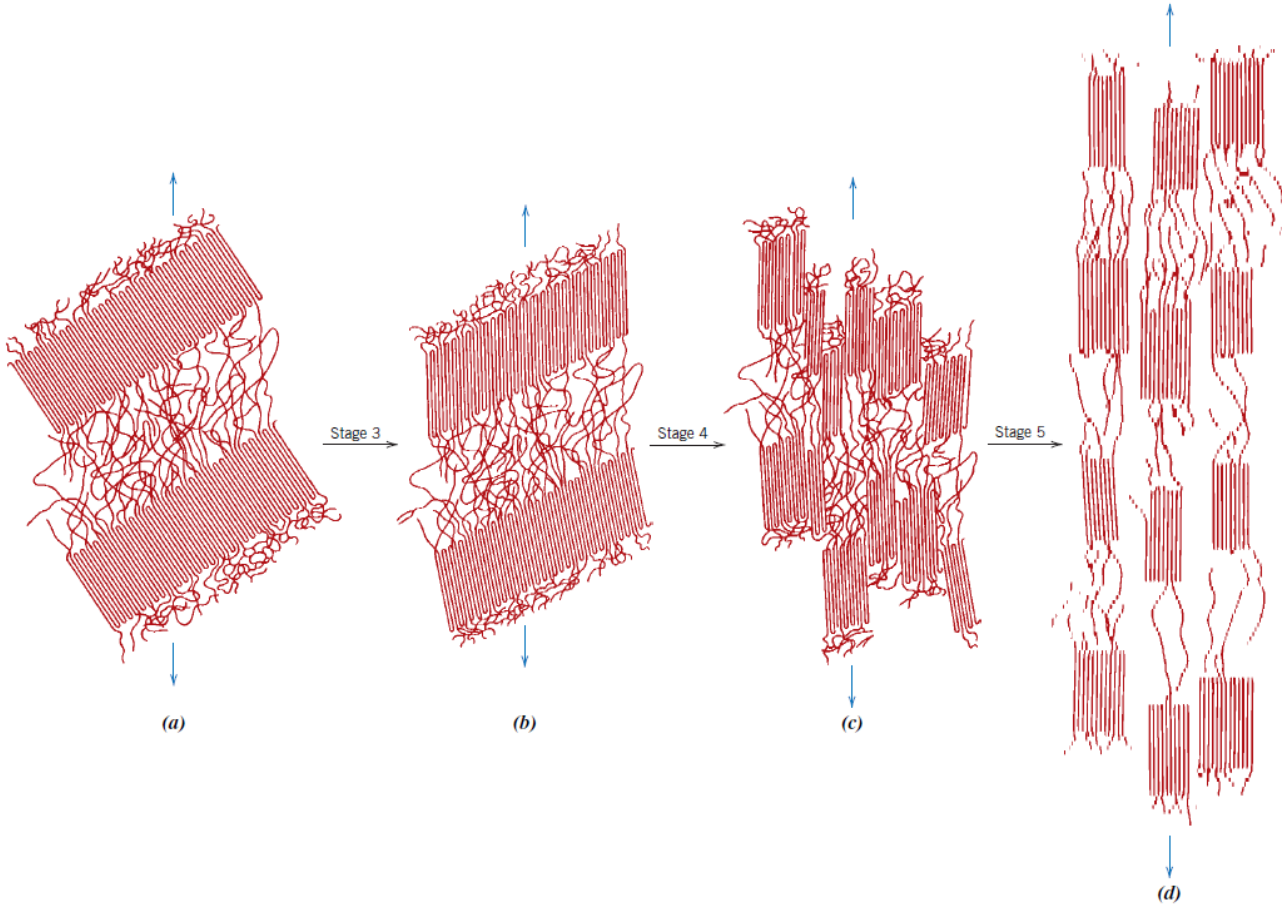

Figure 2.4: Plastic deformation of semi-crystalline polymers (Callister Jr and Rethwisch 2012).

Polymers are usually poor heat conductors, and most of the inelastic work is diffused as heat. The heat may cause a local increase in temperature, which leads to softening of the polymer. This softening effect is more apparent in cases where the strain-rate is high (Rösler et al. 2007).

Visco-Elasticity

Typical for polymers, is that they are rate- and time-dependent. The mechanical energy is dissipated through the diffusion of atoms and molecules in the amorphous parts of the polymers (Hopperstad and Børvik 2017; Gargallo and Radic 2009). This behavior is called visco-elasticity. Polymers are considered visco-elastic due to their ability to creep and are determined to be visco-elastic at all temperatures (Gargallo and Radic 2009).

Visco-Plasticity

Visco-plasticity is the rate dependent version of plasticity (Hopperstad and Børvik 2017). Semi-crystalline polymers experience visco-plastic flow in the amorphous parts first; then it continues in the crystallinities (Ghorbel 2008). When the strain-rate increases, polymers will often experience an increase in yield strength and initial stiffness, but may soften due to adiabatic heating.

Locking

Typical behavior of semicrystalline polymers after extensive stretching is locking. Locking is a phenomenon that is characterized by increased resistance to deformation at approximately $\varepsilon_L = 1 - 1.2$ (Galeski et al. 1992; Z. Bartczak and Lezak 2005). This is caused by severe deformation of the amorphous phase, which, after exhausting, locks and gives the polymer increased strength (Z. Bartczak 2017).

Degradation Process

Polymers that are exposed to hazardous environments will degrade over time. The degradation can vary from color change to the polymer simply dissolving (Lewis 2016). The degradation can be caused by contact with fluids, UV radiation, oxidation, or heat. As it is with many other materials, polymers can and will oxidize when in contact with the correct medium, and will oxidize faster at higher temperatures (Wright and Rapra Technology 2006).

The degradation process caused by contact with fluids, is caused by mass transfer either from the fluid into the polymer or vice versa (Wright and Rapra Technology 2006). This can severely alter

the polymer's properties, either because fillers and plasticizer are washed out, or a weakening fluid is absorbed into the polymer. Essential factors, in this case, is the permeability, the diffusion coefficient, and the solubility of the polymer.

Fillers

Fillers are used to adjust the properties of polymers. These fillers are small particles that are added to the material to, for example, increase toughness and ductility. Fillers can sometimes improve the initial stiffness of a polymer (Ognedal et al. 2014), due to the particles acting as reinforcement if they have enough adhesion to the matrix. When fillers initiate void growth, plastic resistance is decreased. This reduction of plastic resistance can be used to toughen the material by avoiding brittle behavior (Zbigniew Bartczak et al. 1999).

Void Growth

Void growth in polymers gives the polymer a white appearance, which is called stress whitening and is caused by differences in the refractive index (Schirrer et al. 1996). The voids can initiate from irregularities in how the molecules are packed, from cavitation, or due to fillers. When the fillers debond from the matrix, cavitation is initiated. Latent defects can also lead to void growth. It can be considered as a damage mechanism since the load bearing area is reduced. The appearance of voids can be related to plastic dilation (Ognedal et al. 2014), which means that the density of the material decreases. Void growth can also cause a locking behavior due to the material surrounding the void will be subject to considerably more strain.

Glass Transition Temperature

The glass transition temperature signifies the temperature where polymers experience a drastic change in mechanical properties, primarily a change in yield stress and Young's modulus (Rösler et al. 2007). These changes in properties are caused by the bonds widening with increased temperature. The glass temperature is observed as the point where the volume suddenly increases more with increasing temperature. Polymers are highly ductile above their glass transition temperature, but exhibit a more brittle behavior below the glass transition temperature. This change in behavior can introduce challenges for polymeric structures.

2.2 SIMLab Polymer Model

The material model used in the finite element analyses is the SIMLab Polymer Model (SPM). Most of the information in this section is reproduced from SIMLab (2015), with minor changes to fit the thesis.

2.2.1 General Formulation

The corotational stress approach is used to an invariant formulation. The strain rate that is applied in the formulation of the constitutive relations is, therefore, the corotational deformation rate tensor $\hat{\mathbf{D}}$, and for the stress is the corotational stress tensor $\hat{\boldsymbol{\sigma}}$. They are defined as

$$\hat{\mathbf{D}} = \mathbf{R}^{\mathbf{T}} \cdot \mathbf{D} \cdot \mathbf{R}, \quad \hat{\boldsymbol{\sigma}} = \mathbf{R}^{\mathbf{T}} \cdot \boldsymbol{\sigma} \cdot \mathbf{R}$$

where $\boldsymbol{\sigma}$ is the Cauchy stress tensor, $\mathbf{D}$ is the deformation rate tensor, and $\mathbf{R}$ is a rotation tensor that takes the rigid-body rotation of the element into account.

The corotational deformation rate tensor can be decomposed into a plastic and an elastic part, which subsequently are defined as

$$\hat{\mathbf{D}} = \hat{\mathbf{D}}^e + \hat{\mathbf{D}}^p, \quad \hat{\mathbf{D}}^e = \mathbf{R}^{\mathbf{T}} \cdot \mathbf{D}^e \cdot \mathbf{R}, \quad \hat{\mathbf{D}}^p = \mathbf{R}^{\mathbf{T}} \cdot \mathbf{D}^p \cdot \mathbf{R}$$

where $\mathbf{D}^e$ is the elastic deformation rate tensor, and $\mathbf{D}^p$ is the plastic deformation rate tensor.

2.2.2 Elasticity and Plasticity

Hypo-Elasticity

Since the general formulation is limited to small elastic strains, a hypo-elastic formulation must be applied. The hypo-elastic law is defined as

$$\dot{\hat{\boldsymbol{\sigma}}} = \hat{\mathbf{C}}^{\sigma} : \hat{\mathbf{D}}^e$$

where $\dot{\hat{\boldsymbol{\sigma}}}$ is the time derivative of the stress tensor and $\hat{\mathbf{C}}^{\sigma}$ is the elasticity tensor with constant coefficients. The flexibility relation is defined as

$$\hat{\mathbf{D}}^e = \hat{\mathbf{S}}^\sigma : \dot{\hat{\boldsymbol{\sigma}}}$$

where $\hat{\mathbf{S}}^\sigma$ is the inverse of the elasticity tensor, called the flexibility tensor.

Yield Function

The yield function f is given by

$$f(\hat{\boldsymbol{\eta}}, R) = \varphi(\hat{\boldsymbol{\eta}}) - (\sigma_T + R)$$

where $\hat{\boldsymbol{\eta}} = \hat{\boldsymbol{\sigma}} - \hat{\boldsymbol{\chi}}$ is the corotational overstress tensor, $\hat{\boldsymbol{\sigma}}$ is the Cauchy stress tensor, $\hat{\boldsymbol{\chi}}$ is the corotational backstress tensor, σ_T is the yield stress in uniaxial tension, and R is the isotropic hardening parameter. For ductile polymers, the Raghava yield function is applied. The Raghava yield function is both isotropic and pressure dependent and is defined as

$$\varphi(\hat{\boldsymbol{\eta}}) = \frac{(\alpha-1)tr\hat{\boldsymbol{\eta}} + \sqrt{(\alpha-1)^2(tr\hat{\boldsymbol{\eta}})^2 + 4\alpha\Phi^2(\hat{\boldsymbol{\eta}}')}}{2\alpha}, \quad \Phi(\hat{\boldsymbol{\eta}}') = \sqrt{\frac{3}{2}\hat{\boldsymbol{\eta}} : \hat{\boldsymbol{\eta}}'}, \quad \alpha = \frac{\sigma_T}{\sigma_C} \geq 1$$

where α is the parameter that describes the pressure sensitivity, and Φ is the von Mises norm of the deviatoric stress tensor. A particular case occurs if $\alpha = 1$, which gives the von Mises yield criterion.

The flow potential g is defined by

$$g(\hat{\boldsymbol{\eta}}) = \frac{(\beta-1)tr\hat{\boldsymbol{\eta}} + \sqrt{(\beta-1)^2(tr\hat{\boldsymbol{\eta}})^2 + 4\beta\Phi^2(\hat{\boldsymbol{\eta}}')}}{2\beta}, \quad \beta = \frac{2-\rho}{1+\rho} \geq 1, \quad \rho = \frac{\varepsilon_T^p}{\varepsilon_L^p}$$

where β, is the plastic dilation parameter, ρ is the plastic contraction, ε_L^p is the longitudinal plastic strain, and ε_T^p is the transverse plastic strain.

Plastic Dissipation and Flow Rule

The visco-plastic dissipation per unit volume is defined by

$$\mathfrak{D}_{vp} = (\hat{\boldsymbol{\sigma}} - \hat{\boldsymbol{\chi}}) : \hat{\mathbf{D}}^{\mathbf{P}} = \hat{\boldsymbol{\eta}} : \hat{\mathbf{D}}^{\mathbf{P}}$$

It is assumed that some of the plastic deformation power, i.e., what is related to the elasticity, is stored while the remainder is dissipated. The inelastic dissipation per volume, $\mathfrak{D}_i$, can be established as a sum of both the visco-plastic and -elastic dissipation.

It is required from the second law of thermodynamics that the inelastic dissipation is greater or equal than zero. This is fulfilled by selecting a fitting visco-elastic model and a plastic flow rule. The plastic flow rule is defined as

$$\hat{\mathbf{D}}^{P} = \dot{\lambda} \frac{\partial g}{\partial \hat{\boldsymbol{\eta}}}$$

where $\dot{\lambda}$ is the plastic parameter, which is zero in the elastic domain and positive in the plastic domain. The function $g = g(\hat{\boldsymbol{\eta}}) \geq 0$, is a convex and positive homogenous function of order one of the overstress tensor, which means that

$$\hat{\boldsymbol{\eta}} : \frac{\partial g}{\partial \hat{\boldsymbol{\eta}}} = g$$

From this, the visco-plastic dissipation can be defined as

$$\mathfrak{D}_{vp} = \hat{\boldsymbol{\eta}} : \hat{\mathbf{D}^{\mathbf{P}}} = \dot{\lambda} \hat{\boldsymbol{\eta}} : \frac{\partial g}{\partial \hat{\boldsymbol{\eta}}} = \dot{\lambda} g \geq 0$$

The visco-plastic dissipation is therefore zero in the elastic domain and postive in the visco-plastic domain, because of the plastic parameters characteristics.

Isotropic Hardening and Softening

The isotropic hardening parameter is defined by the set of evolution equations

$$\dot{R} = \sum_{i=1}^{3} \dot{R}_i, \quad \dot{R}_i = \Theta_{Ri}\left(1 - \frac{R_i}{Q_{Ri}}\right)\dot{p}, \quad R_i|_{t=0} = 0$$

where Θ_{Ri} is the initial hardening modulus, and Q_{Ri} is the saturation value of the term R_i. If R_i is assumed to be zero when there is no plastic strain, integration of the evolutionary equations establishes the extended Voce rule.

$$R = \sum_{i=1}^{3} R_i, \quad R_i = Q_{Ri}\left(1 - exp\left(-\frac{\Theta_{Ri}}{Q_{Ri}}p\right)\right)$$

The reason for having three terms is to describe the various stages of the hardening phase. If both $Q_{Ri} > 0$ and $\Theta_{Ri} > 0$, the hardening will exhibit a gradually decreasing hardening until it saturates at Q_{Ri}. If $Q_{Ri} < 0$ and $\Theta_{Ri} < 0$, then it will exhibit softening with a gradually decreasing slope until it saturates at Q_{Ri}. However, if $Q_{Ri} < 0$ and $\Theta_{Ri} > 0$, the hardening will be exponential. The three different terms can be seen in Figure 2.5

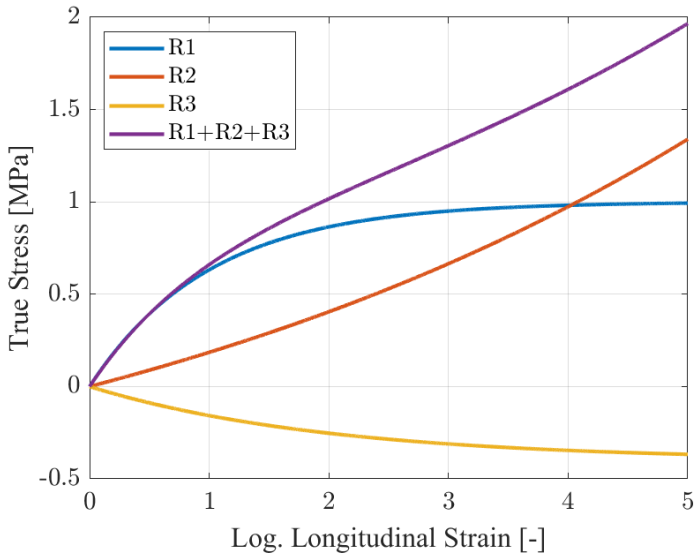

Figure 2.5: Three different Voce terms where R_1 has $Q_{R1} > 0$ and $\Theta_{R1} > 0$, R_2 has $Q_{R2} < 0$ and $\Theta_{R2} > 0$, R_3 has $Q_{R3} < 0$ and $\Theta_{R3} < 0$, and $R_1 + R_2 + R_3$ is the sum of the three terms.

Visco-Plastic Constitutive Relation

For polymers exhibiting rate-dependent behavior, the equivalent plastic strain rate can be defined by a constitutive relation

$$\dot{p} = \begin{cases} 0 & \text{if } f \leq 0 \\ \dot{p} & \text{if } f > 0 \end{cases} \quad \dot{p} = \dot{p}_0 \left\{ \exp\left[\frac{1}{C} \left(\frac{\phi(\hat{\boldsymbol{\eta}})}{\sigma_T + R} - 1 \right) \right] - 1 \right\}$$

where the coefficient $\dot{p}_0$ is the reference strain rate and C determines the immediate sensitivity of the flow stress. By using this relation, $\phi(\hat{\boldsymbol{\eta}})$ is defined as

$$\phi(\hat{\boldsymbol{\eta}}) = (\sigma_T + R) \left[1 + C \ln\left(1 + \frac{\dot{p}}{\dot{p}_0} \right) \right] \text{ for } f > 0$$

2.3 Extended Drucker-Prager Material Model

The extended Drucker-Prager material model is a built-in model in Abaqus. It is suitable for isotropic and pressure sensitive materials (Hopperstad and Børvik 2017), which is the case for many polymers.

Abaqus offers three different variations of the extended Drucker-Prager material model: a linear, a hyperbolic, and an exponential. All three can be used for materials which are pressure dependent, have higher compressive yield strength than tensile, and exhibit plastic dilation (*Abaqus Analysis User's Manual* 2010). Further, the model allows the user to describe the hardening and softening using tabular data.

The yield criteria for the different extended Drucker-Prager models are formulated as

$$\text{Linear: } F_{DP} = t - p_{DP} \tan \beta_{DP} = 0, \quad t = \frac{1}{2} \left[1 + \frac{1}{K} - \left(1 - \frac{1}{K} \right) \left(\frac{r}{q} \right)^3 \right]$$

where β_{DP} is the friction angle, p_{DP} is the equivalent pressure, q is the Mises equivalent stress, r is the third stress invariant, d is the cohesion, and K is the ratio between yield stress in triaxial tension and yield stress in triaxial compression(*Abaqus Analysis User's Manual* 2010).

$$\text{Hyperbolic: } F_{DP} = \sqrt{(d'|_0 - p_{DP,t}|_0 \tan \beta_{DP})^2 + q} - p_{DP} \tan \beta_{DP} = 0$$

where $p_{DP,t}|_0$ is the initial hydrostatic tension strength, d' is the hardening parameter, $d'|_0$ is the initial value of d', and β_{DP} is the friction angle at high confining pressure (*Abaqus Analysis User's Manual* 2010).

$$\text{Exponential: } F_{DP} = aq^b - p_{DP} - p_{DP,t} = 0$$

where a and b are independent material parameters and $p_{DP,t}$ is the hardening parameter, representing hydrostatic tension strength (*Abaqus Analysis User's Manual* 2010).

2.4 Digital Image Correlation

Strain and displacements are two essential factors in engineering applications. However, it is not always easy to receive information regarding the strains and displacements in a material. Digital Image Correlation (DIC) is a non-contact optical technique which may be used for studying deformations. The method is cheap, accurate, and straightforward compared to other techniques (McCormick and Lord 2010).

DIC compares digital photographs of a test specimen at different deformation stages. The photograph pixels are represented as data sets containing different values based on the grey level in each pixel. To perform a DIC analysis, the tested specimens are required to have a specific pattern, e.g., speckled, which can be recognized across an image series. DIC uses cross-correlation to find shifts between these data sets. DIC can measure surface displacement by tracking the shifts of the pixels and build up to full field 2D and 3D strain maps and deformation vector fields.

There are several software programs available for performing DIC analyses. NTNU has developed a DIC tool called *eCorr* (Fagerholt et al. 2013).

2.5 CT-Scanning

Computed Tomography (CT) uses X-ray radiation to capture images of an object from different angles to form a three dimensional model of both the internal and external structure of the object (Chiffre et al. 2014). This is a non-destructive method to map the flaws of materials, but is limited by both the time required to do such a scan and the thickness of the material. If

the material is too thick, the radiation is not able to penetrate the material. When analyzing materials, the object is rotated while the radiation source and detector stay put. Most materials are also not vulnerable to higher intensities of radiation than what can be applied in medicinal CT, which allows a higher intensity for material testing. With an axis of rotation in the object, it is possible to move the object closer to the source or closer to the detector. Both features strengths and weaknesses, as moving the object closer to the source gives higher resolution, but less distinct images, while moving it closer to the detector gives more distinct images and lower resolution (Chiffre et al. 2014).

3 Material and Degradation

This chapter introduces the material used and describes the degradation procedures that have been employed to obtain the degraded material.

3.1 The Material Used in This Study: Polyamide 11

PA11 is a semi-crystalline thermoplastic used in many engineering applications, especially in the oil and gas industry, and is the material studied in this report. It is commonly used as liners in flexible risers, because of its low capacity to absorb moisture (Arkema 2011). A carved out part of a PA11 liner was used in this thesis to acquire specimens. The PA11 piece is seen in Figure 3.1.

Figure 3.1: Part of a virgin PA11 liner used for the experimental work conducted in this thesis.

PA11 is resistant to chemical aging induced by hydrocarbons and many solvents (Arkema 2011), and is resistant to both diluted acids and bases. Although PA11 has a low capability for moisture absorption, PA11 has a high permeation rate for methanol. This is because of the small size of the methanol molecules. This makes methanol an excellent solver for extracting plasticizer from PA11 (Arkema 2011). A common reaction with methanol is methanolysis, which reduces the molecular weight, although this happens at approximately 140°C.

Arkema produces the PA11 used in this report, and it is called Rilsan BESNO P40TL. The TL suffix notifies that anti-oxidant packages are added to the material to resist oxidation (Arkema 2011). According to Arkema, it can operate continuously at 125°C due to its thermal stability, and its glass transition temperature is around 0°C due to its plasticizer content (Arkema 2011).

Typical forms of degradation of this material, when used in flexible risers, are believed to be shortening of the molecular chain, i.e., reducing the molecular weight, due to hydrolysis, and reduction of plasticizer content (Arkema 2011).

3.2 Degradation Procedures and Goals

Degraded PA11 from a used riser was not available at the time when the tests were performed. Hence, they were artificially degraded in Equinor's laboratory to simulate the damage inflicted during use. The most usual problems surround a reduction of plasticizer content and reduction of molecular weight. Therefore, three degradation procedures were performed to simulate three different scenarios. The goals of these procedures were: (P) one where only the plasticizer content was reduced, (W) one where only the molecular weight was reduced, and (PW) one where both the plasticizer content and molecular weight were reduced.

The molecular weight was measured through corrected inherent viscosity (CIV). Energy dispersive X-ray fluorescence spectrometry (XRF) was used for measuring the amount of plasticizer.

3.2.1 Procedure 1 - Reduction of Plasticizer Content (P)

To reduce the amount of plasticizer in the specimens, the samples were washed in methanol at 40 °C for 120 hours. Afterward, the specimens were dried in a vacuum oven. Results showed a reduction of the plasticizer from 13.61 wt% to 6.97 wt% while the molecular weight remained approximately unchanged. The reduction to 6.97 wt% was lower than the goal of 3.0 wt%.

3.2.2 Procedure 2 - Reduction of Plasticizer Content and Molecular Weight (PW)

The goal during the second procedure was a CIV of 0.8 dl/g and ESV of 3.0 wt%. The samples were first treated as in the first procedure to extract the plasticizer. After this step, they were exposed to a HCl solution, $pH = 3$, at 120°C for two weeks. CIV results showed a reduction from 1.8 dl/g to 1.2 dl/g. However, the plasticizer content was further reduced from 7.0 wt% to 4.5 wt%. This was a concern because all the plasticizer had probably not been extracted in the previous procedure. This step had now changed two variables, plasticizer content and molecular weight.

3.2.3 Procedure 3 - Reduction of Molecular Weight

The goal of procedure 3 was a CIV of 0.8 dl/g and an ESV of 12 wt%. A hydrochloric acid solution (HCl), $pH = 3$, with 10ml of plasticizer added was used to only reduce the molecular weight of the specimens. The samples were aged in the HCl solution for two weeks at 120°C. Extra plasticizer was added to the HCl solution to prevent leaching of plasticizer from the material. The result was ESV of 24.9% and CIV of 1.2 dl/g. This, unfortunately, meant that the samples became over saturated with plasticizer due to having absorbed more from the solution. The measured plasticizer amount of 24.9 wt% is most likely too high since Arkema, the producers of the material, believes the material to be fully saturated of plasticizer around 15 wt%. The absorption of the plasticizer also caused significant swelling of the specimens. The dimensions increased by approximately 10%. Hence, they could no longer fit in the tension machine, and the threads of the specimens had to be turned one more time.

The degradation results are summarized in Table 3.1.

Table 3.1: Goals and results of the degradation processes.

Material		**V**		**P**		**PW**		**W**	
		Goal	Result	Goal	Result	Goal	Result	Goal	Result
ESV	[wt%]	12.0	13.61	3.0	6.97	3.0	4.47	12.0	24.89
CIV	[dl/g]	1.8	1.82	1.8	1.77	0.8	1.20	0.8	1.21

The degraded specimens are illustrated in Figure 3.2, where the swelling is visible in the bottom specimen.

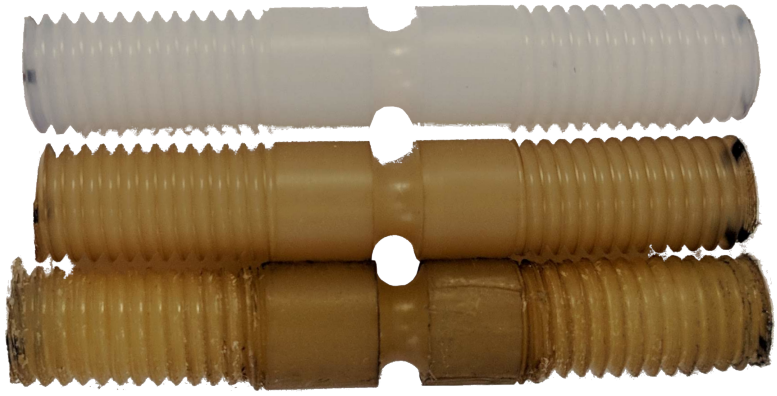

Figure 3.2: The degraded specimens. From top to bottom: PA11 with reduced amount of plasticizer (P), PA11 with reduced amount of plasticizer and molecular weight (PW), and PA11 with reduced molecular weight (W).

Part II

Experimental Work and Calibration

4 Material Testing

Several tension and two compression tests have been conducted at NTNU, Gløshaugen in the laboratories at the Department of Structural Engineering to get a better understanding of the material properties of PA11. In this chapter, these tests are described, and the results are presented and discussed.

4.1 General Experimental Setup for Tension and Compression Tests

The material was provided by Equinor as a small part of a pipe. All specimens were cut from the pipe's axial direction. After being cut from the pipe, the specimens were turned to five different axisymmetric shapes seen in Figure 4.1. These geometries, a smooth (S), three notched (R20, R5, R2), and a cylinder (Cy) have been used to obtain the information regarding the material and to validate the material model.

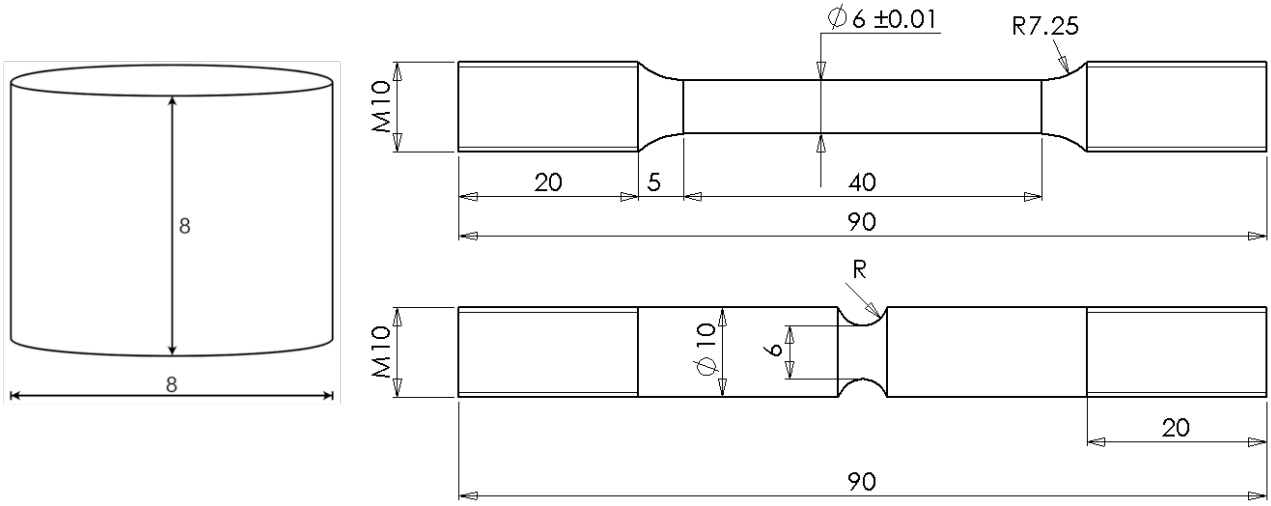

Figure 4.1: The geometry of the specimens: a cylinder (Cy), a smooth (S), and three notched with radiuses of 20mm, 5mm and 2mm (R20, R5, and R2). Dimensions are given in mm.

Two Instron machines were used to conduct the tension and compression tests. One machine with a 5kN load cell was employed for six virgin tension tests at room temperature, and one machine with a 2kN load cell was used for the remaining tension and compression tests. Both machines fastened the specimen with threads on both ends as seen in Figure 4.2. Further, the standard nominal strain rate was $\dot{\varepsilon} = 10^{-3}s^{-1}$. Some tests were conducted at $\dot{\varepsilon} = 10^{-2}s^{-1}$ and $\dot{\varepsilon} = 10^{-1}s^{-1}$ to check the visco-plastic behavior. To achieve the target nominal strain rate, the nominal displacement rates seen in Table 4.1 were employed. The displacement rates for notched specimens were reduced based on experience from previous PVC tests conducted at SIMLab.

Table 4.1: Displacement rates for experiments with a target value of nominal strain rates of $10^{-3}s^{-1}$.

Geometry	Cy	S	R20	R5	R2
Nominal displacement rate $[mm/min]$	0.48	2.40	2.20	1.92	1.68

Figure 4.2: Illustration of how the specimens are fastened with threads (the picture is rotated 90 degrees).

Two cameras were set up with a 90°angle to each other, as seen in Figure 4.3. They were used to monitor the tests, and the images produced were later used to perform 2D DIC analyses from each angle. The acquisition rate of the cameras varied between 0.01 Hz to 2 Hz depending on notch radius and nominal strain rate. The captured images were loaded into eCorr for DIC analyses to obtain strain fields and displacement fields of the specimens.

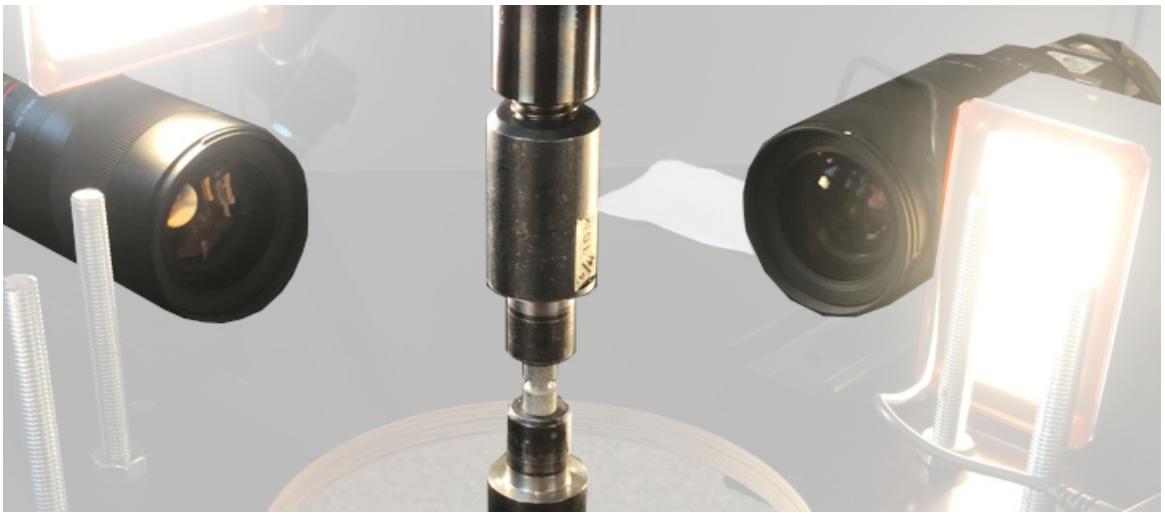

Figure 4.3: Configuration of the experimental setup.

For eCorr to be able to distinguish different points on the test specimen, the surface on the test specimens had a random speckled pattern. For test specimens at room temperature, this was obtained by spraying on a white paint to reduce glare from the lights and then speckled with black paint, as seen in Figure 4.4a. A different speckle procedure was used at -20°C since the paint cracked easier at low temperatures. Grease was applied to the specimen before a black powder was sprinkled on the surface as seen in Figure 4.4b. The painting was applied the same day as the tests were performed to ensure that the paint did not crack during the experiment.

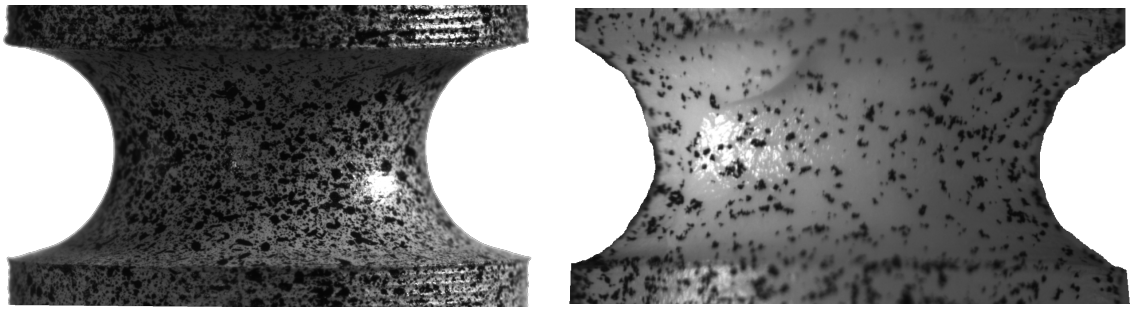

(a) Room temperature (b) -20 °C

Figure 4.4: Two speckled test specimens at different temperatures.

The material variations were also tested below their glass transition temperature. Since the glass temperature was around 0°C, the testing was decided to be conducted at -20°C. This was to ensure that the entire specimen was cold enough. To obtain a cold environment during the tension tests, a closed transparent chamber was placed around the test machine as seen in Figure 4.5. The temperature was reduced by flushing liquid nitrogen into the chamber. A sensor registered the temperature and a feed back loop ensured the environment was sufficiently

cool by flushing in more nitrogen if needed. To make sure the test specimens were at the right temperature, they were stored in a freezer at -20°C, and then placed in the transparent chamber. After the specimens had been in the chamber for a minimum of 15 minutes, the tests were started.

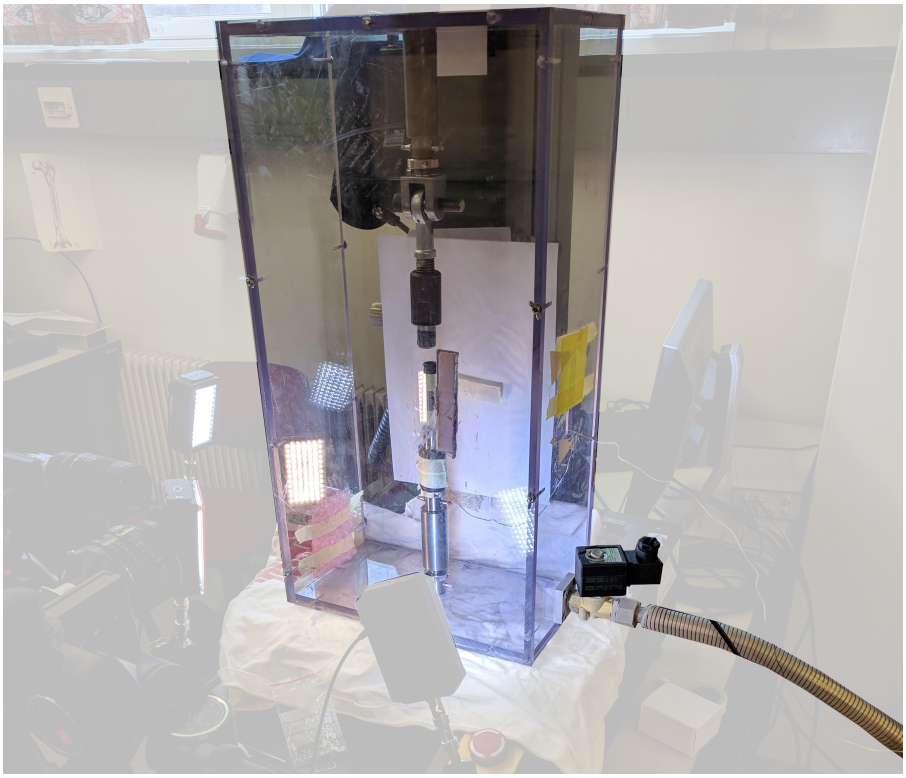

Figure 4.5: Configuration of the tests at -20°C.

When performing the compression tests, grease was applied to the top and the bottom of the specimens to reduce the friction on the load surfaces.

Some tests were run two times to ensure repeatability of the results. The scatter between the replicates was small.

The material testing has been performed with virgin PA11 (V), PA11 with reduced plasticizer content (P), PA11 with reduced molecular weight (W), and PA11 with both reduced plasticizer content and molecular weight (PW). To make it easier to differentiate between the different tests, each test variation has been labeled, as can be seen in Table 4.2.

The radius of the tension specimens and the width and thickness of the compression specimens were measured with a sliding caliper prior to the testing. All test specimens were approximately the right size, except the specimens with reduced molecular weight (W), which had expanded due to the increase in plasticizer content. This has been explained in-depth in Section 3.2.

The threads of the swelled test specimens (W) were turned one more time to fit them to the fixtures of the test machine, but the capacity of the threads was lost, and the test specimens were below the necessary quality to perform tension tests.

Table 4.2: Structure of the different test configurations along with their descriptions, abbreviations, and plot identifications.

Property	**Description**	**Abbreviation**	**Plot identification**
Material	Virgin	V	No identification
	Reduced content of plasticizer	P	Circle ∘
	Reduced molecular weight	W	Diamond ◊
	Reduced molecular weight and reduced content of plasticizer	PW	Cross ×
Geometry	Smooth	S	Orange
	Notch radius 20mm	R20	Blue
	Notch radius 5mm	R5	Green
	Notch radius 2mm	R2	Red
	Cylinder	Cy	Purple
Temperature	Room temperature	H	Continuous line ——
	-20°C	C	Dashed line - - -
Strain rate	$\dot{\varepsilon} = 10^{-3}$ 1/s	No abbrev.	No identification
	$\dot{\varepsilon} = 10^{-2}$ 1/s	Ra2	Triangle △
	$\dot{\varepsilon} = 10^{-1}$ 1/s	Ra3	Square □
Load	Tension	No abbrev.	No identification
	Compression	No abbrev.	No identification

4.2 Post-Processing

The post-processing was initiated with DIC anlyses. Using eCorr, a grid was defined with a certain number of elements, where each element represented a given area on the surface of the test specimens. Afterwards, eCorr computed the displacement and strain fields. An example of a grid and the DIC results from one camera angle is shown in Figure 4.6. The size of the elements on the grid varied depending on the applied camera equipment and the distance from the camera to the test specimen. Under cold conditions, the distance was increased due to the chamber covering the specimens. Hence, the number of pixels on the test specimen were decreased. Depending on the test situation, the element size varied between 25×25 and 50×50 pixels.

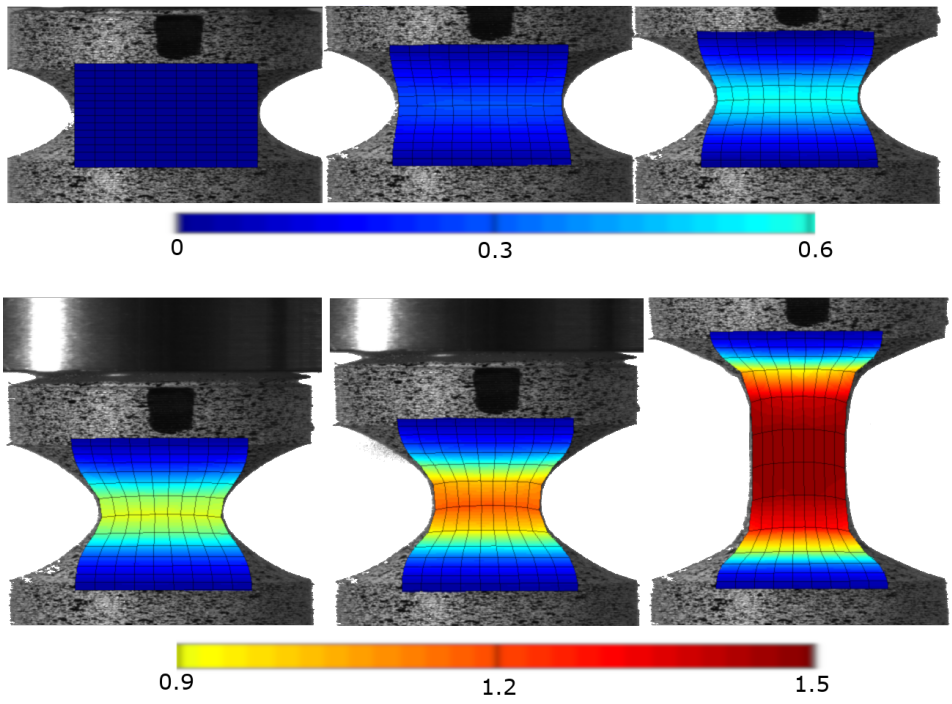

Figure 4.6: Logarithmic longitudinal strain results from eCorr at six different times for a R5 test specimen.

Two DIC analyses were conducted for each test specimen, one for each camera. The logarithmic principle strains were exported from the element in the center of the grid, which in all cases represented the worst case scenario regarding strain values. Furthermore, the selected element was orthogonally directed towards the camera, which reduced possible errors from the camera projection. The log. longitudinal strain, ε_L, was set to the first principal strain, and the log. transverse strain, ε_T, was set to the second principle strain. An example of the eCorr results from both camera angles is shown in Figure 4.7, which addresses one of the R2 specimens. In

general, the longitudinal strain from the two angles was very similar. Given the two camera angles, the scatter between the transverse strains were often larger than the scatter between the longitudinal strains. Since the transverse strain results indicated that the material was highly isotropic, the transverse strain in all directions was set to the average of the transverse strain from both camera angles. The results from Engebretsen (2017) validate the isotropy.

$$\varepsilon_T = \frac{1}{2}(\varepsilon_T^{Camera_1} + \varepsilon_T^{Camera_2})$$

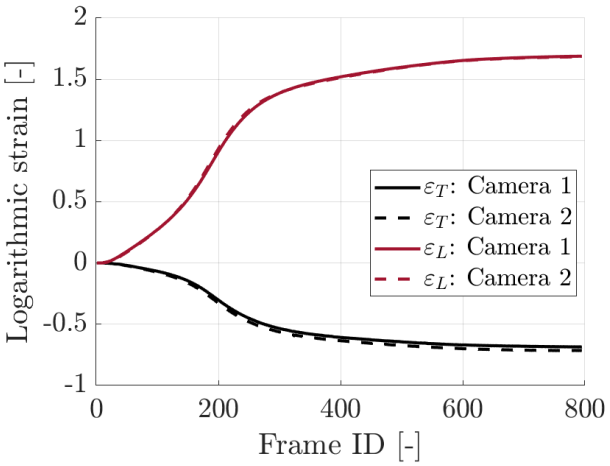

Figure 4.7: Logarithmic longitudinal and transverse strain results from eCorr at captured frames from two cameras for a R2 test specimen.

The volumetric strain, ε_V, was calculated as the sum of the transverse strain from both camera angles and the longitudinal strain from camera 1.

$$\varepsilon_V = \varepsilon_T^{Camera_1} + \varepsilon_T^{Camera_2} + \varepsilon_L^{Camera_1}$$

Based on measurements with a sliding caliper, the scatter between the design diameter and the measured diameter was too low to be accounted for. Hence, the initial diameter, D_0, in the post-processing was chosen as 6mm for the tension tests and 8mm for the compression tests.

The current diameter, D_C, was computed based on the average transverse strain.

$$D_C = D_0 \cdot exp(\varepsilon_T)$$

The current area, A_C, was determined based on the current diameter.

$$A_C = \pi \cdot D_C^2/4$$

The true stress, σ, and the nominal stress, σ_0, were calculated based on the current area, A_C, and the initial area, $A_0 = \pi \cdot D_0^2/4$, respectively, and the recorded force, F.

$$\sigma = F/A_C$$

$$\sigma_0 = F/A_0$$

The true strain rate, $\dot{\varepsilon}_L$, was found by numerical differentiation of the longitudinal strains

$$\dot{\varepsilon}_L = (\varepsilon_L^{i+1} - \varepsilon_L^i) \cdot f$$

where f is the number of pictures per second and ε_L^i is the longitudinal strain at time i.

4.3 Uniaxial Tension and Compression Results

This section presents the results from the tension and compression tests. The results have been post-processed as described in the previous section using Matlab and eCorr (DIC). Tension test results of the virgin material will be presented before the results of the degraded material are introduced. For the virgin specimens, the effect of notch radius, temperature, and nominal strain rate will be studied. For the degraded specimens, the effect of different degrading processes will be studied. Lastly, the compression tests will be presented.

The conducted tests are listed with their test variables and plot identifications in Table 4.3.

Table 4.3: The conducted tests with their tests variables and plot identification.

Test number	Material	Geometry	Load	Temp.	$\dot{\varepsilon}$ $[s^{-1}]$	Plot ID
1 V-S-H	V	Smooth	Tension	20 °C	10^{-3}	
2 V-S-H	V	Smooth	Tension	20 °C	10^{-3}	
3 V-R20-H	V	R20	Tension	20 °C	10^{-3}	
4 V-R5-H	V	R5	Tension	20 °C	10^{-3}	
5 V-R2-H	V	R2	Tension	20 °C	10^{-3}	
6 V-R2-H	V	R2	Tension	20 °C	10^{-3}	
7 V-R20-C	V	R20	Tension	-20 °C	10^{-3}	
8 V-R20-C	V	R20	Tension	-20 °C	10^{-3}	
9 V-R2-C	V	R2	Tension	-20 °C	10^{-3}	
10 V-S-H-Ra2	V	Smooth	Tension	20 °C	10^{-2}	
11 V-S-H-Ra3	V	Smooth	Tension	20 °C	10^{-1}	
12 V-R5-H-Ra2	V	R5	Tension	20 °C	10^{-2}	
13 V-R5-H-Ra3	V	R5	Tension	20 °C	10^{-1}	
14 P-R20-H	P	R20	Tension	20 °C	10^{-3}	
15 PW-R20-H	PW	R20	Tension	20 °C	10^{-3}	
16 W-R20-H	W	R20	Tension	20 °C	10^{-3}	
17 P-R20-C	P	R20	Tension	-20 °C	10^{-3}	
18 PW-R20-C	PW	R20	Tension	-20 °C	10^{-3}	
19 P-R2-H	P	R2	Tension	20 °C	10^{-3}	
20 PW-R2-H	PW	R2	Tension	20 °C	10^{-3}	
21 W-R2-H	W	R2	Tension	20 °C	10^{-3}	
22 P-R2-C	P	R2	Tension	-20 °C	10^{-3}	
23 PW-R2-C	PW	R2	Tension	-20 °C	10^{-3}	
24 V-Cy-H	V	Cylinder	Compression	20 °C	10^{-3}	
25 V-Cy-H	V	Cylinder	Compression	20 °C	10^{-3}	

The results will be presented by four different plots:

- Nominal stress and force vs. displacement
- True stress vs. log. longitudinal strain
- True transverse strain and diameter vs. log. longitudinal strain
- True volumetric strain vs. log. longitudinal strain

Furthermore, different time points, t_i, are plotted to make it easier to compare global and local behavior. These points represent a given time during the test. A star is also plotted on the specimens which fractured. However, not all fractured test results have a star due to two DIC problems. Firstly, some experiments were not properly speckled. Secondly, the first six test specimens were deformed beyond what the cameras captured. Hence, at large strains some tests only have a star on the force vs. displacement plot because of problems with the DIC analyses.

4.3.1 Effect of Notch Radius

In Figure 4.8, results from six virgin test specimens at room temperature under standard strain rate, $\dot{\varepsilon} = 10^{-3}s^{-1}$, are presented. There are two replicates of the smooth and the R2 specimens. The scatter between the replicates is low. One of the R2 specimens fractured, while the other R2 specimen was stopped at an earlier stage. It was stopped at the point where it was believed to have it's highest volume strain. This specimen would be used in an ex-situ CT-scan.

Figure 4.8a shows the relationship between force (which corresponds to nominal stress) and displacement. As the notch radius declined, the material behaved more brittle as a component. One of the smooth specimens was displaced 150mm, but Figure 4.8a is cropped. Please see Figure A.2 for more details regarding test V-S-H.

The relationship between true stress and logarithmic longitudinal strain is observed in Figure 4.8b. The stresses at small strains are similar among different notch radiuses. As the strains increased, the hardening effect initiated earlier in the specimens with low triaxiality.

A softening effect was seen on the global response, force vs. displacement plot. However, this effect was not seen on the local response, true stress vs. strain. See the t_i's for comparison.

The effect of notch radius on transverse strain and diameter is observed in Figure 4.8c, where it was seen that a lower notch radius implied lower transverse strain. Further, note that the transverse strain axis has a linear scale while the diameter axis has a log. scale.

The volumetric strain is shown in Figure 4.8d. Volumetric strains were high for low notch radiuses, especially for a notch radius of 2mm.

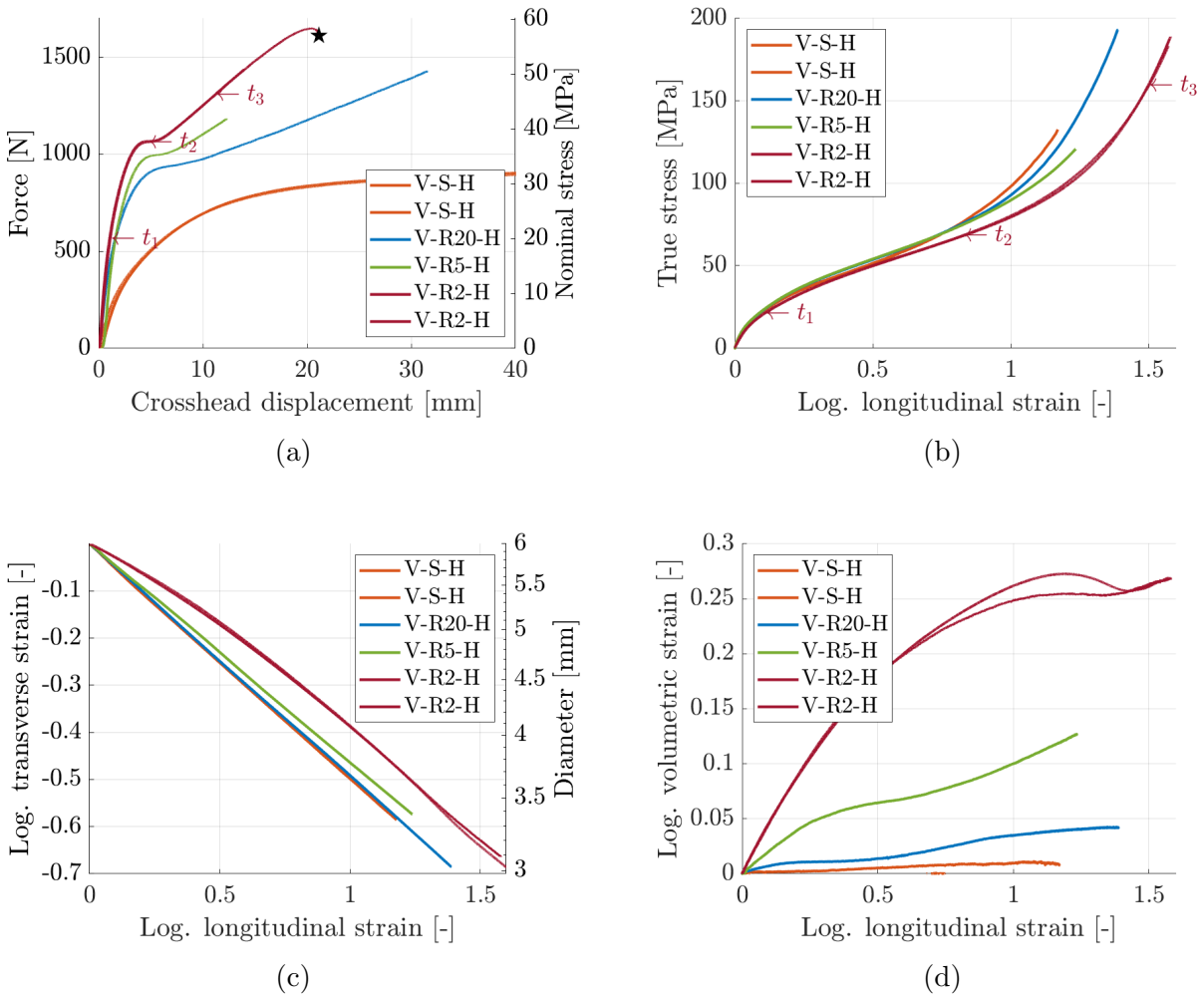

Figure 4.8: Results of six virgin test specimens at room temperature with different notch radiuses.

4.3.2 Effect of Temperature

The effect of temperature on the material properties is shown in Figure 4.9. It is recalled from Table 4.3 that tests at -20°C were only carried out with R20 and R2 specimens at a low strain rate, $\dot{\varepsilon} = 10^{-3}s^{-1}$. For the R20 specimens, two tests were conducted, but there were problems with the cameras for one of the tests. Hence, a proper DIC analysis was only done on one of the tests. The scatter between the force vs. displacement is low, which indicates good replicability. Furthermore, the speckling quality of the R2 specimen at -20°C (V-R2-C) was poor. The results from the DIC analyses of the specimen was usable for strains up to approximately 0.6.

A softening effect can be observed after the first local force maximum in Figure 4.9a. However, at the same time, this effect was not seen in the plot of true stress vs. log. longitudinal strain. Furthermore, at low temperatures, the Young's modulus and the yield strength increased, as seen in Figure 4.9b. This was expected due to the specimens being below the glass transition temperature.

Both the cold test specimens experience a small decline in the transverse strain compared to the warm test specimens. Further, the cold R20 test specimens experienced an increase in volumetric strains at large longitudinal strains. This observation was not seen for R2, but beware that the R2 specimen fractured at the time the R20 specimen started to experience an increase in volumetric strain.

Due to the discrepancy between the local and global response, control of the calculations has been done. As seen in Table 4.4, the computations from the local and global response match well.

Table 4.4: Control of calculations of forces and stresses for V-R20-H and V-R20-C.

Test Specimen	Time	Tension Machine	DIC			Controll
		Force	Stress	Transverse strain	Area	Stress×Area
V-R20-H	t_2	788.4	33.8	-0.1006	23.3	787.9
	t_3	935.6	57.3	-0.2789	16.4	940.8
V-R20-C	t_2	1773.5	79.4	-0.1150	22.3	1771.2
	t_3	1556.2	129.6	-0.4321	12.0	1554.2

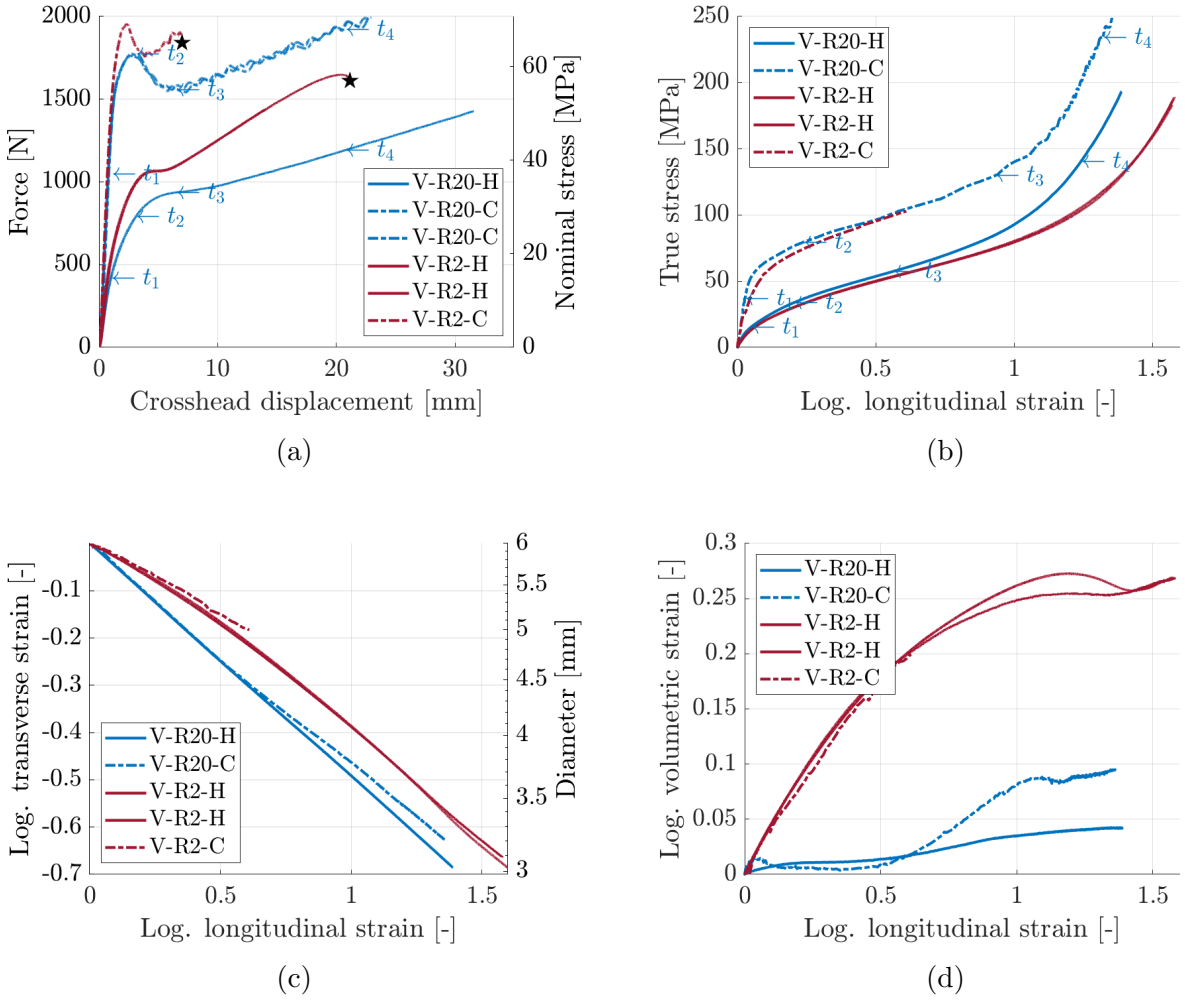

Figure 4.9: Results of two (three) virgin test specimens at -20°C and three virgin test specimens at room temperature.

4.3.3 Effect of Nominal Strain Rates

Figure 4.10 presents the results of tests carried out at different nominal strain rates. It is noted that the true plastic strain rates may be found in Appendix A. Furthermore, the nominal strain rates were: $\dot{\varepsilon} = 10^{-3}\text{s}^{-1}$, $\dot{\varepsilon}^{Ra2} = 10^{-2}\text{s}^{-1}$ and $\dot{\varepsilon}^{Ra3} = 10^{-1}\text{s}^{-1}$.

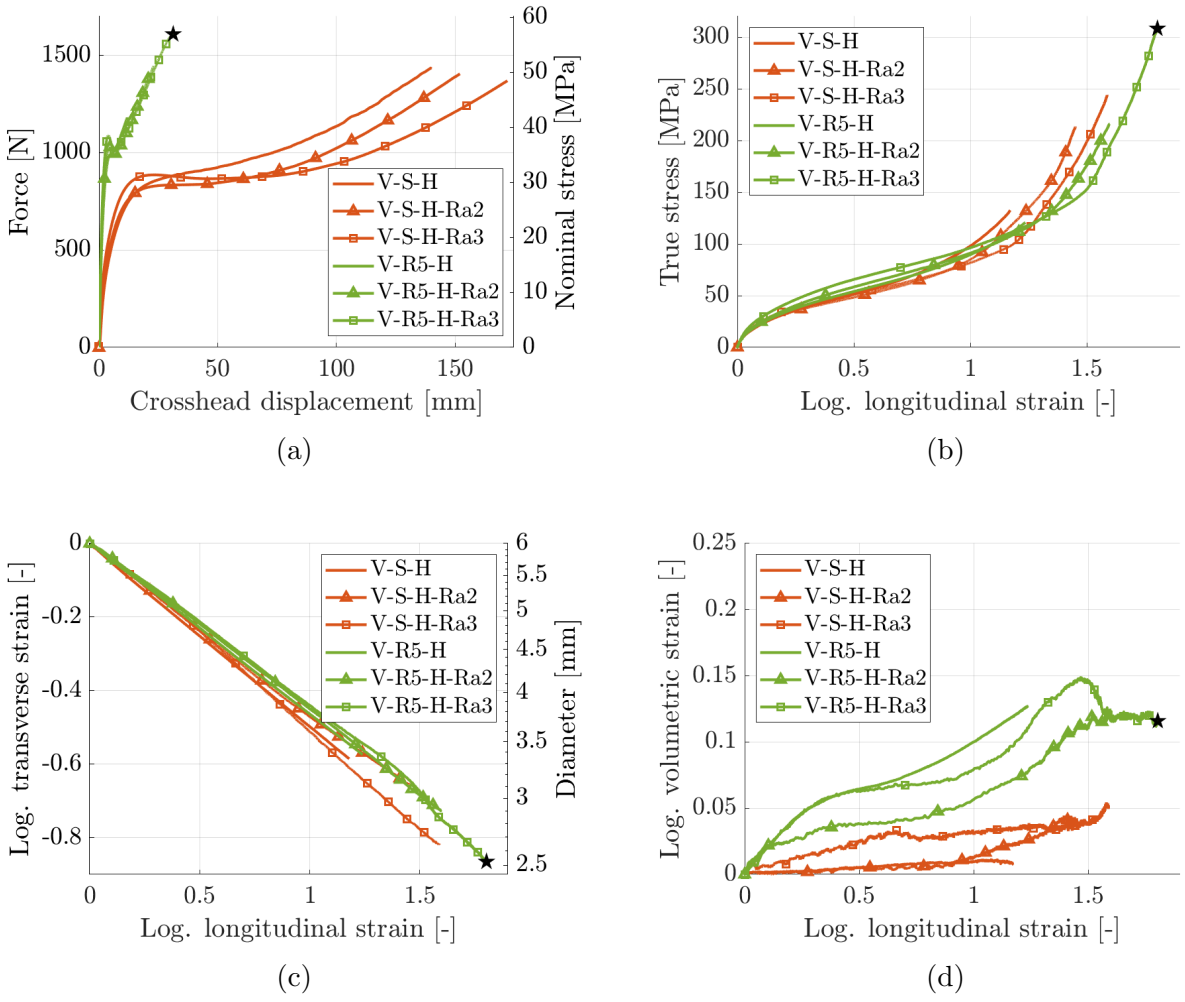

Figure 4.10: Results of six virgin test specimens at room temperature with different notch radiuses and nominal strain rates.

The results did not show a strong effect from different nominal strain rates. For low strains, the material strength increased as the nominal strain rate increased. For larger strains, the material hardening reduced with the strain rate until a locking effect was observed. A clear pattern was not identified regarding the impact of strain rates on transverse and volumetric strains.

4.3.4 Effect of Degrading

Figures 4.11, 4.12, 4.13 and 4.14 show the effect of the different degrading processes on R20 and R2 specimens under warm and cold conditions. Three different degradation procedures are investigated, see Section 3.2, and compared to the virgin material at room temperature and -20°C. The specimens with reduced molecular weight was not tested at -20°C. This was due to the expansion of the specimens under the degrading process, as recalled from Section 3.2. Many of the observed effects for each degrading process were similar for both R20 and R2 under warm and cold condition. Hence, even though each test is unique, the effects of the degrading methods showed good replicability.

The degradation effects will be presented by comparing the impact of each degradation procedure with the virgin material. Hence, three paragraphs will describe the results.

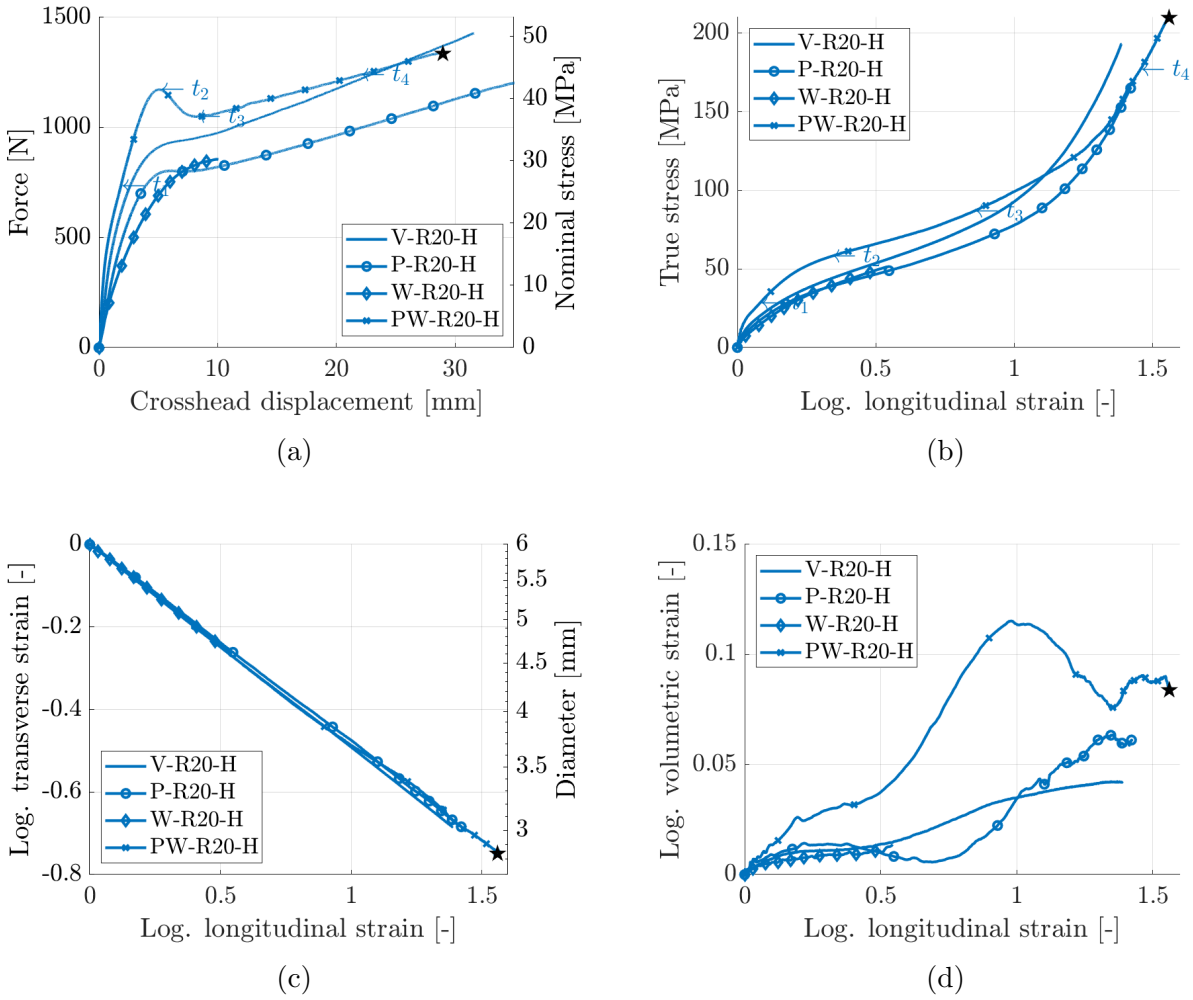

Figure 4.11: Results of three degraded specimens (P, W, and PW) and one virgin (V) specimen at room temperature with notch radiuses of 20mm.

Removing the plasticizer without reducing the molecular weight (P) resulted in a softer material. This effect was seen for all test specimens in both the force vs. displacement plot and the true stress vs. log. longitudinal strain plot. It is noted that a plasticizer is supposed to soften the material, not harden it. Thus, the response of the specimens with reduced plasticizer content is unexpected and will be discussed in Section 4.6. The transverse strain was slightly reduced for R2 with reduced plasticizer content compared to the virgin material. However, this effect was not seen on R20. The volumetric strain was slightly increased for R2, but this was also not seen for R20.

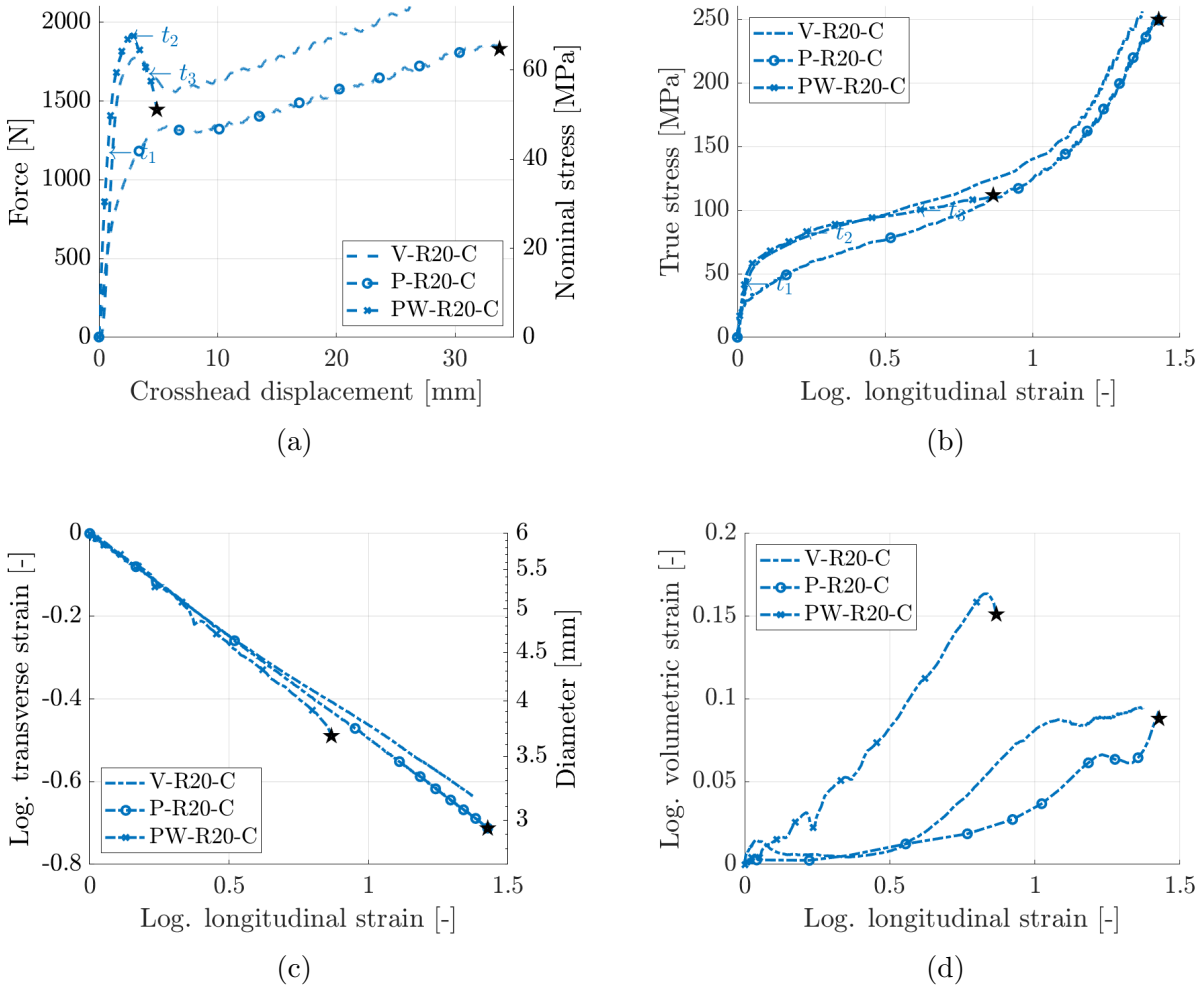

Figure 4.12: Results of two degraded specimens (P and PW) and one virgin specimen (V) at -20 °C with notch radiuses of 20mm.

By reducing both the content of plasticizer and the molecular weight (PW), the material got stiffer and the strength increased. This effect was seen for all test specimens in both the force vs. displacement plot and the true stress vs. log. longitudinal strain plot. The transverse strain remained approximately the same for all test specimens. However, the volumetric strain

experienced a significant increase among all the test specimens, except for R2 under the cold condition which fractured early.

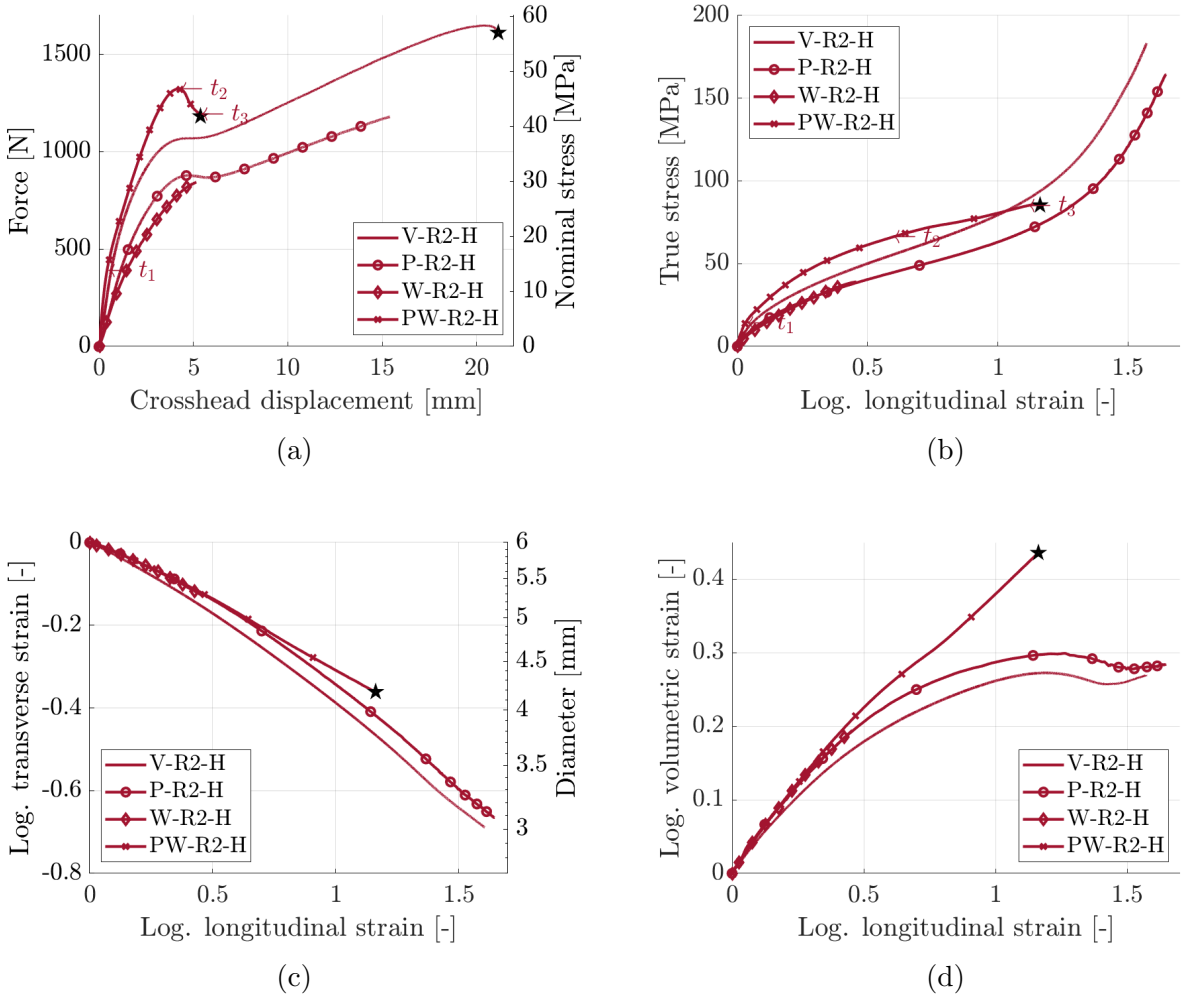

Figure 4.13: Results of three degraded specimens (P, W, and PW) and one virgin specimen (V) at room temperature with notch radiuses of 2mm.

Before describing the results from only reducing the molecular weight (W), it is recalled that during the degrading process, the material absorbed a large amount of plasticizer from the solution. Hence, when looking at the results, this must be taken into account. The measured diameter was approximately 10% higher, thus the area was approximately 20% higher. The stress in this specimen was therefore substantially lower than in the figure. Furthermore, the test specimens behaved softer than the virgin specimens. Both the transverse and volumetric strain stayed unchanged after the degradation process. The test specimens detached quickly from the fixtures due to the poor quality of the threads, as previously described.

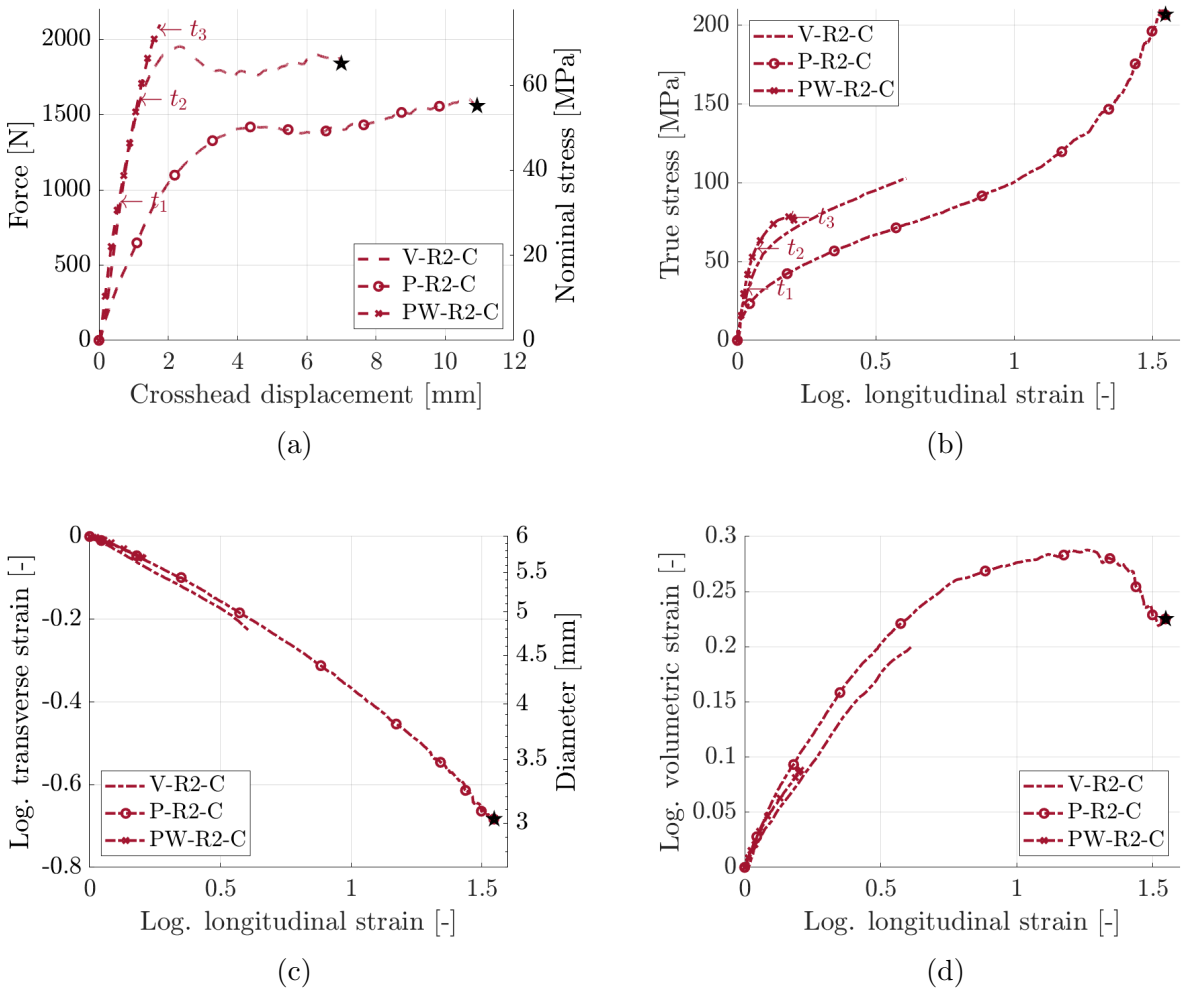

Figure 4.14: Results of two degraded specimens (P and PW) and one virgin specimen (V) at -20 °C with notch radiuses of 2mm. Please note that the test PW-R2-C was stopped since the applied load reached the maximum force of the machine.

4.3.5 Compression Tests

In Figure 4.15, two compression tests of cylinders are shown. The scatter between the plots was small. For comparison, a tension test of a smooth virgin specimen is also plotted.

Figure 4.15a shows the relationship between force and crosshead displacement. This relationship varied greatly between the tension and compression tests due to different geometries of the test specimens. Figure 4.15b shows that the material was stronger in tension than compression. This is surprising and will be discussed in Section 5.5. The log. transverse strain vs. log. longitudinal strain plot was similar to the virgin tension specimen. Furthermore, the volumetric strain was approximately equal to zero during the test. The cylinder specimens exhibited no barreling behavior during the tests.

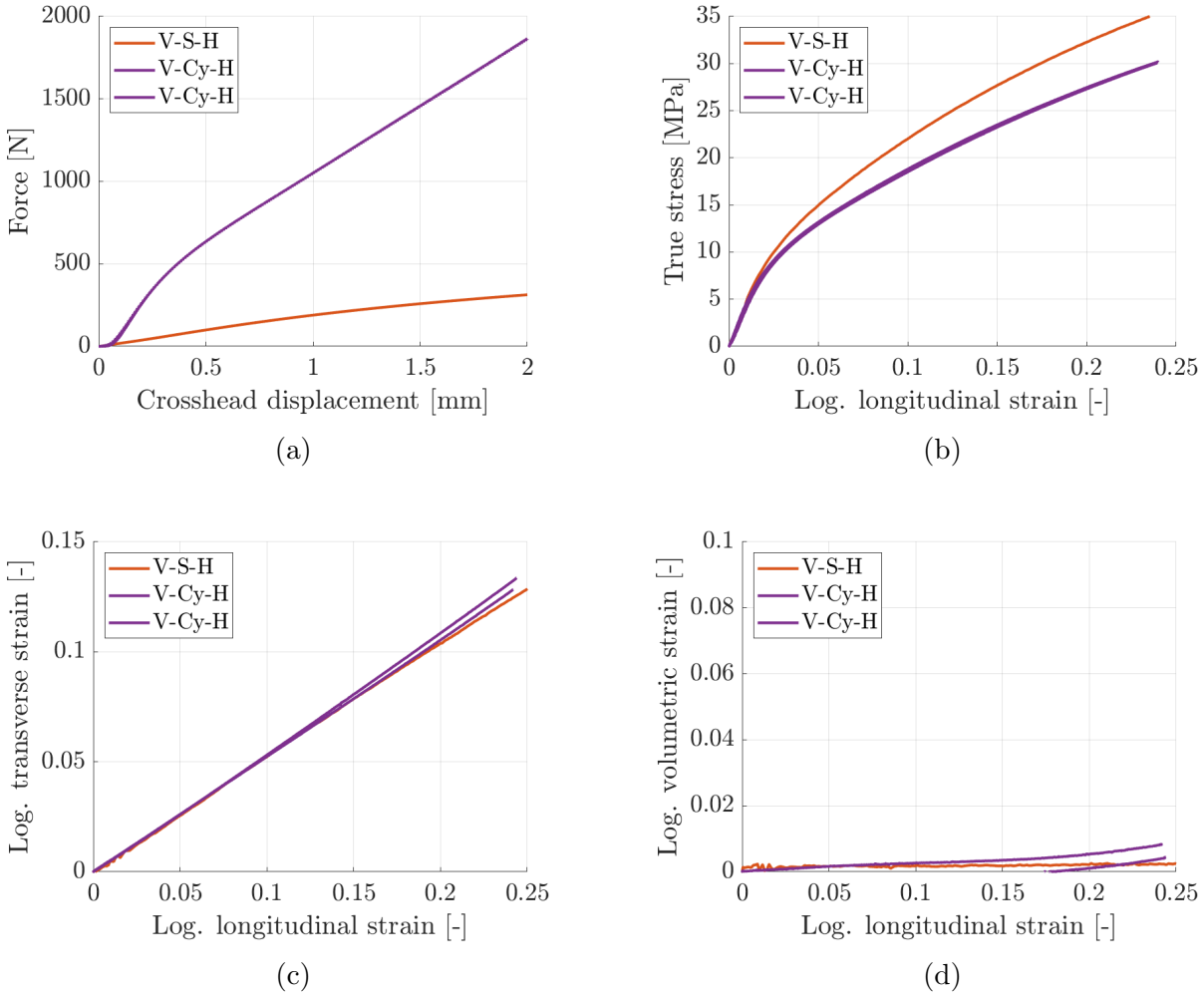

Figure 4.15: Results of two virgin specimens at room temperature under compression and one smooth specimen under tension.

4.4 CT-Scanning

To obtain more information regarding void growth in PA11, several in-situ CT scans were planned. Due to two problems, all the in-situ scans were unfortunately unsuccessful. Firstly, two small bolts that were the fixtures for the specimen were not suitable because the threads of the specimens were not strong enough. Therefore, many of the test specimens lost the grip at an early stage of the experiment. Secondly, the machine was only able to displace the test specimens 7mm, which was not enough to reach the elongation where the largest volumetric strains appeared. Hence, no results of interest were obtained. In this section, the experimental in-situ setup will be described and the results from one ex-situ CT-scan will be presented.

The setup for performing in-situ CT-scans is shown in Figure 4.16. The test specimen was fastened in a small tension test rig that was adapted to the CT apparatus. Further, the specimen was speckled as previously described and seen in Figure 4.4. One camera captured the experiment with the help of two lights. Lastly, the CT-scanner sent radiation beams (X-rays) through the specimen.

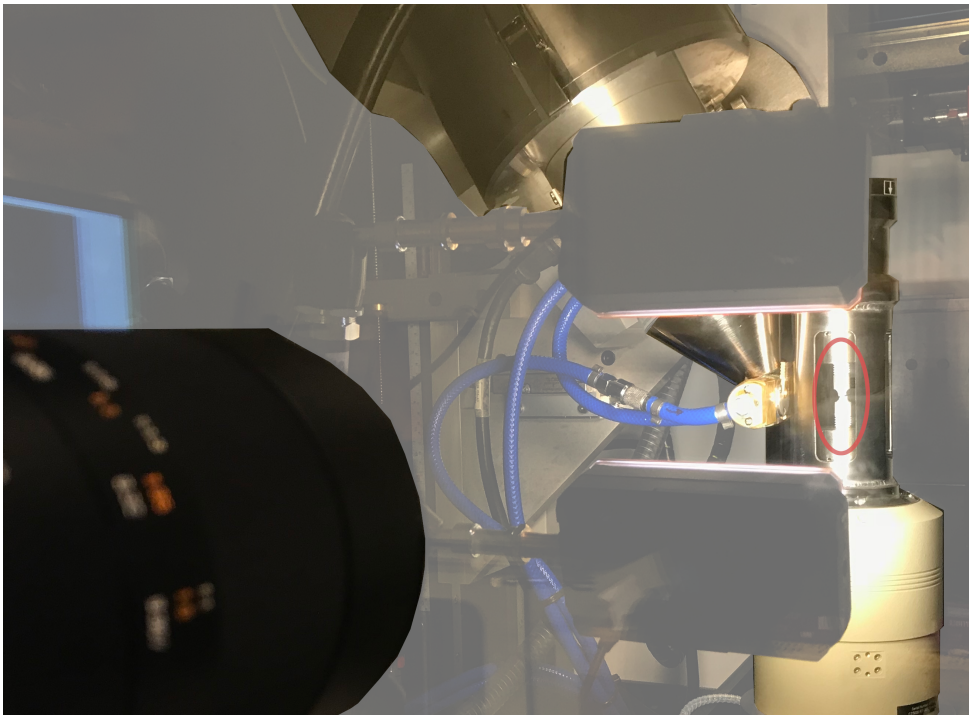

Figure 4.16: Configuration of in-situ CT-scanning.

By using the described setup, three independent results were obtained. Firstly, the load cell records displacement and force. Secondly, the images from the camera may be used for DIC analyses, i.e., strain and displacement fields may be obtained. Lastly, the CT-scan resulted in

images consisting of different grey level values, which represented the density of the material. Each image represents a cross-section in the specimen.

As a preparation for the in-situ CT-scan of PA11, an ex-situ CT-scan was performed of a virgin R2 specimen to check if the material was homogenous. When performing an in-situ CT-scan, the specimen is not rotated, and the images acquired is from just one angle. Therefore, a prerequisite was that the material was homogenous. A tension test of V-R2-H resulted in failure at 21 mm and a peak in the volumetric strain at 14mm. Based on this result, a second tension test was performed of V-R2-H where the specimen was elongated to 14mm. A CT-scan of the 14 mm elongated test specimen was carried out. The results are presented in Figure 4.17 which showed a relatively homogeneous density for the virgin material. Hence, no apparent tendency of cavitation. The mechanical tests presented in Section 4.3.4 indicated that the change of volume, in general, was larger for the degraded materials. It was therefore likely that in-situ CT-scans of these materials would have disclosed changes of density.

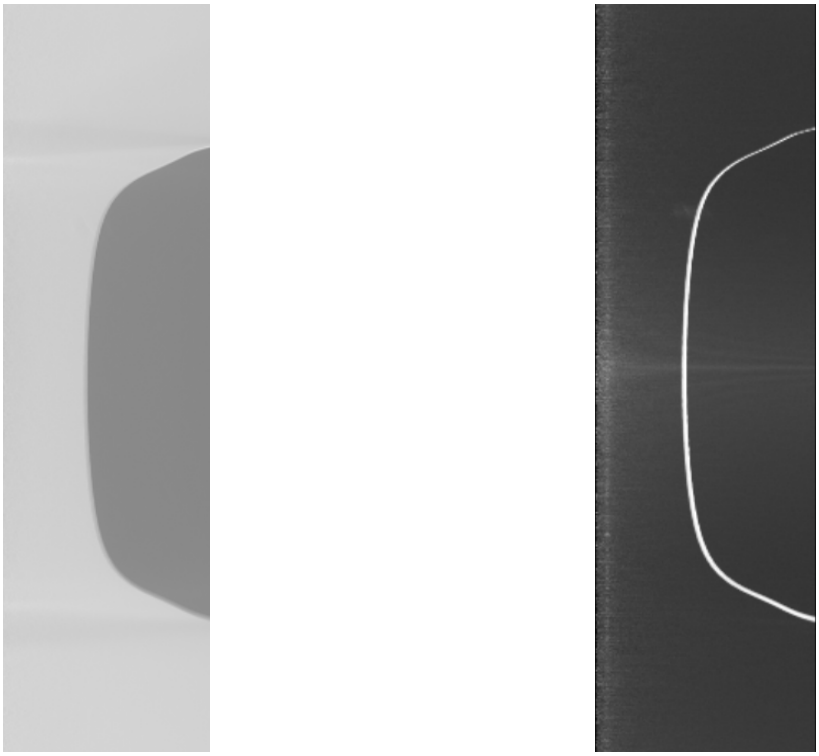

(a) Mean of all cross-section densities.

(b) Standard deviation of all cross-section densities.

Figure 4.17: Results from ex-situ CT-scanning of a R2 specimen.

4.5 Sources of Error

There were possible sources of errors from the experiments and in the post-processing of the results. First, the speckling of some of the specimens, especially the cold specimens, was not optimal, which reduced the quality of the DIC results. Glare from lights on the specimens also reduced the quality of the DIC results. The reduced quality of DIC analyses resulted in a reduction of information at high strains for some specimens.

The diameter results presented in this chapter were calculated from the transverse strain as previously described. It is recalled that the transverse strain was based on DIC results from the most critical element on the specimen surface. Hence, the strains were taken from a projection of the specimen surface, which lead to minor errors in the results. However, the diameter may also be represented by a vector with two points which are placed on the edge of the specimen's DIC mesh. DIC analyses may calculate the change of the length of the vector. The two procedures are compared in Figure 4.18. It was observed that the scatter between the methods was small. The small discrepancy in Figure 4.18b at a crosshead displacement of 10mm was probably due to poor speckling, which required a coarser mesh.

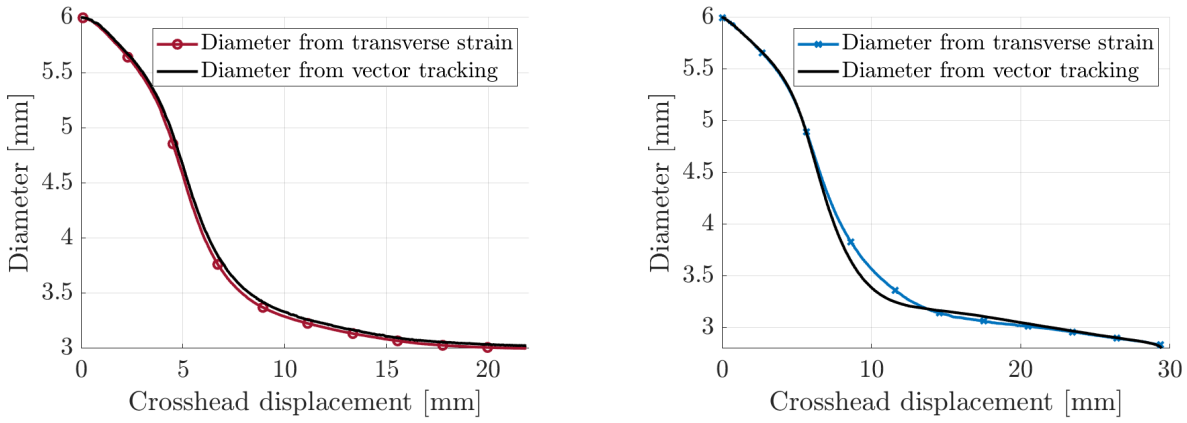

(a) P-R2-H (b) PW-R20-H

Figure 4.18: Control of the calculated diameter.

The cameras and the force tracker were not in perfect synchronization. Since the tests lasted for a long time, this effect was assumed negligible. Furthermore, some of the captured pictures were lost during the experiment. The reason why some images were lost was most likely due to an unidentified bug in the software used. These images, along with their corresponding data points, were removed under the post-processing, but the problem may have lead to poorer results.

The threads on the test specimens were a problem during several of the experiments. At high longitudinal strains, they either slowly loosened or in some cases got completely detached from the machine. It was possible to identify this problem on the captured images. Hence, when the problem occurred, the post-processing was stopped. This resulted in loss of information at high strains.

4.6 Discussion and Conclusion

Under all test conditions, the notch radius had a significant impact on the behavior of PA11. A smaller notch radius increased the damage in the specimen. The volumetric strain also increased with a decreasing notch radius. Further, for small notch radiuses, the test specimen behaved more brittle as a component, but locally it still behaved highly ductile.

When the temperature was decreased the material got stiffer, the yield strength increased, and the ductility decreased. This was due to the temperature being below the glass transition temperature (Rösler et al. 2007). A softening effect in the force was also observed. This effect was probably due to the temperature being below the glass transition temperature as well.

At small strains the strength of the material increased as the nominal strain rate increased. At larger deformations, the material softened. Adiabatic heating was most likely the reason for the observed softening effect since the test specimens with high nominal strain rates experienced a considerable increase in temperature. The observed increase of strength of PA11 with increasing strain rate corresponds with literature (Boisot, Fond, et al. 2008; Nishida et al. 2014; Boisot, Laiarinandrasana, et al. 2011). If the temperature is below the glass transition temperature, the effect of different strain rates is expected to be greater. Further, it is expected that the material is more sensitive towards different strain rates when the amount of plasticizer reduces.

A reduction of the plasticizer content made the material softer. This was unexpected since the plasticizer is supposed to soften the material. The softening of the material might be due to the methanol used to wash out the plasticizer. If the methanol permeated into the material, it may have worked as a plasticizer. Furthermore, the reduction of plasticizer should have increased the glass transition temperature, which should increase the stiffness of the material (Arkema 2011).

It was difficult to determine the effect of reducing the molecular weight since the specimens

with a reduction of molecular weight also had an increase in plasticizer. The specimens with reduced molecular weight became softer, but this was most likely due to the increased amount of plasticizer.

The reduction of both the softener and the molecular weight made the specimen stiffer, increased the tensile strength, and decreased the ductility. This was expected, but there were several interesting observations. Firstly, a global softening effect was seen on all test specimens regardless of the temperature. Secondly, an increase in volumetric strain was observed. Lastly, a loss in the locking effect was seen on all test specimens, except on R20 under room temperature. Since the diameter stayed unchanged, an increase in voids was a possible explanation of the observations. An increase in voids may also be the reason for the increased tendency of fracture. By visual inspection of the test specimens, a whitening effect was seen on the fracture surface, which also indicated void growth. Examples of different fracture surfaces from a selection of the test specimens are presented in Figure 4.19. It was observed that reduced plasticizer and molecular weight results in the most significant whitening effect.

Figure 4.19: Fracture surfaces of a selection of test specimens. From left to right: V-R2-H, V-R2-C, P-R2-C, PW-R2-H, PW-R20-C.

5 Calibration

This chapter presents how the material parameters were calibrated for the SPM. Furthermore, the simulation process and its results are presented and discussed. Lastly, a Drucker-Prager model is briefly presented.

Each material variation at room temperature and -20°C has been calibrated to a unique material model. The material parameters were optimized by visually comparing the lab tests and the simulations.

5.1 Abaqus Model

The numerical simulations were performed in the explicit module of Abaqus, which is a finite element analysis program. The specimens were modeled with three dimensional solid elements. The elements used were C3D8, 8-node linear brick elements, with a coarse mesh at the ends of the specimen, and a finer mesh in the middle to properly supervise what happened in the most critical zone. The decided mesh size was based on results from Engebretsen (2017). The coarsest mesh had elements with a target size of 2mm×2mm×2mm, while the finer mesh had elements as small as 0.2mm×0.2mm×0.2mm.

The reason for using the dynamic, explicit model and not the static, general model, was that after large strains, the elements exhibited considerable amounts of non-linearities that the static model could not deal with properly. Moreover, the dynamic, explicit model had a lower computational time, which made optimizing the different parameters faster.

To reduce the computational time, the specimens were modelled as quarters, exploiting the symmetry of them, as can be seen in Figure 5.1, which is a simplified version of the R2 specimen. The specimens were not modelled as axisymmetrical since these models produced unrealistic results.

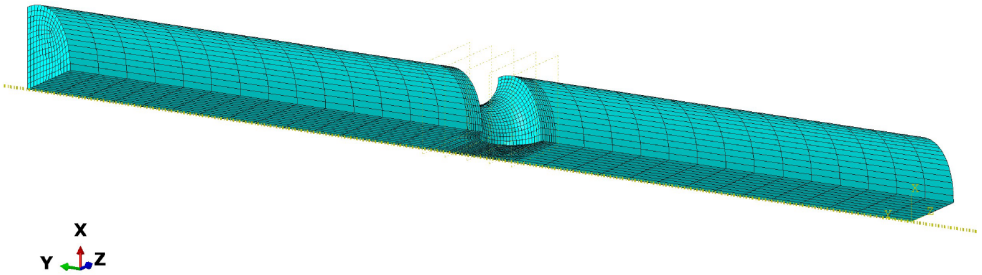

Figure 5.1: The simplified R2 specimen.

When the results were appropriate, the whole specimen was modelled, as seen in Figure 5.2, to control that the simplifications had not deteriorated the validity of the results.

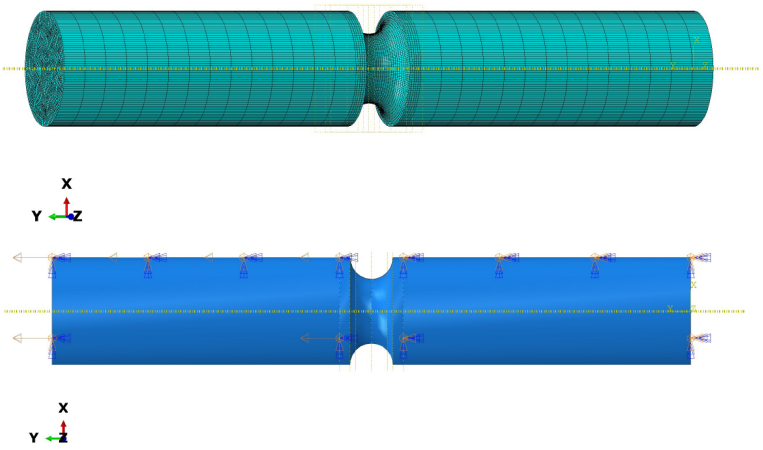

Figure 5.2: The applied modell of the entire R2 specimen used to validate the quarter specimen.

When obtaining the necessary values from the models, such as diameter reduction, force, displacement, true stress and log. longitudinal strain, different approaches were used. True stress and log. longitudinal strain were obtained by selecting an element at the edge of the centre of the specimen, see Figure 5.3a. Further, as seen in Figure 5.3b and 5.3c, two separate nodes were used to obtain the diameter reduction, i.e., the transverse displacement, and total longitudinal displacement of the specimen. Lastly, in Figure 5.3d, the section selected for obtaining the force is showed. The reaction force in the longitudinal direction from each node in the section was summed, thus calculating the total force.

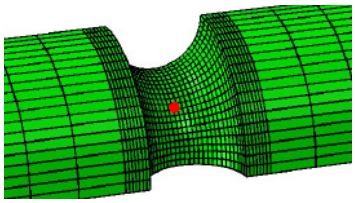

(a) Element used to obtain the true stress and the log. longitudinal strain.

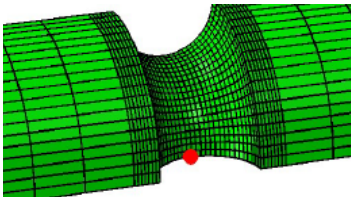

(b) Node used to obtain diameter reduction.

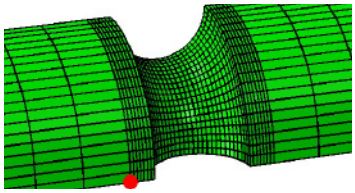

(c) Node used to obtain total displacement.

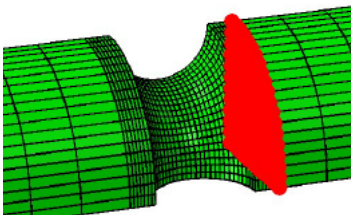

(d) Section used to obtain the total force.

Figure 5.3: Elements, nodes and sections used for exporting forces, displacements, strains and stresses.

The boundary conditions used are shown in Figure 5.4. Both *symmetry planes* were fixed against rotations and displacement in all directions, except displacement in the longitudinal direction. Furthermore, the *fixed* boundary condition was fixed against rotations and displacement in all directions. Lastly, the boundary condition *displacement* was fixed against rotations and displacement in all directions, except displacement in the longitudinal direction. The load was applied with a velocity in the longitudinal direction, which was ramped up by an amplitude to avoid unphysical oscillations in the simulations.

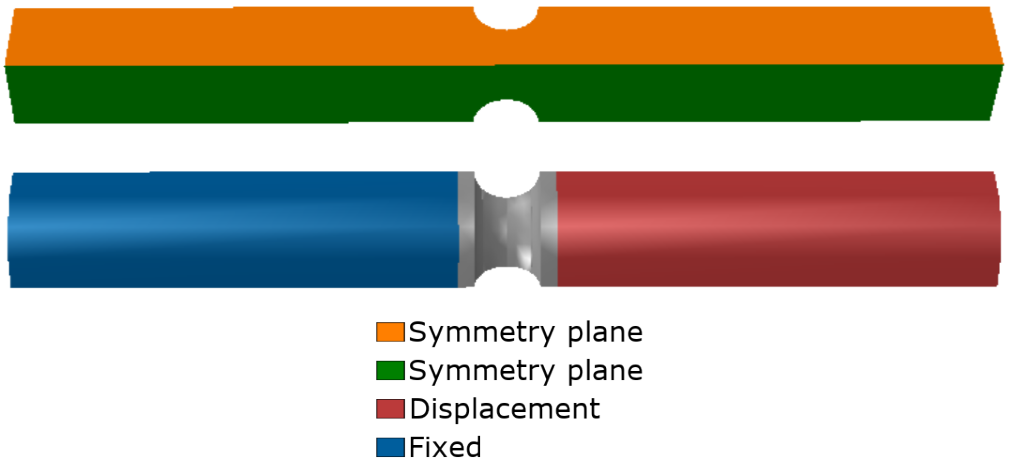

Figure 5.4: The boundary conditions used for simulating the tension tests.

Due to a dynamic, explicit model being only conditionally stable, the time increment had to

be sufficiently small to ensure stability. To make the analysis run faster, mass scaling was applied, but applying mass scaling may deteriorate the results. To check if a model had a small enough time increment, the kinetic energy was compared to the total external work. Since the experiment was quasi-static, only a small amount of the work should become kinetic energy, something the model had to replicate. As seen in Figure 5.5, which has a logarithmic vertical axis, the kinetic energy is less than 0.1% of the total external work, when the mass scaling had a target time increment of $\Delta t = 5 \cdot 10^{-5}$s. Thus, the strain energy was dominating.

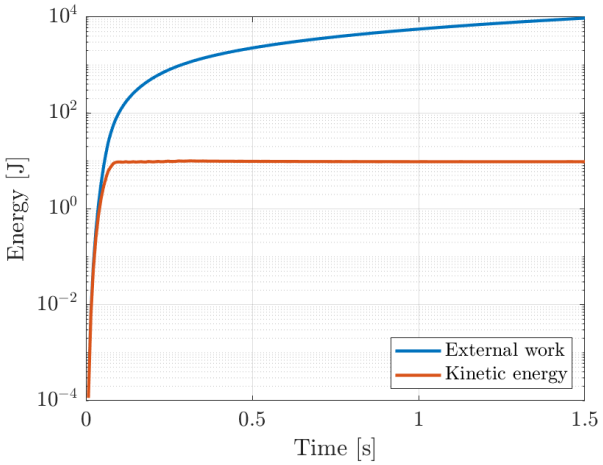

Figure 5.5: Comparison between external work and kinetic energy of the R20 simulation.

It should be noted that the illustrations in this section was of the R2 specimen. A similar approach has been done for all specimens.

5.2 Calibration of the SIMLab Polymer Model

The SPM, see Section 2.2, was used as the numerical model to simulate the different variations' of PA11 behavior. To calibrate the parameters of the model, MATLab has been applied. Due to the amount of different material models needed to be established, a general procedure is first presented before an in depth calibration of the virgin PA11 is described. The remaining six material models will be touched upon after this, but in a condensed form, where only the optimization of the initial parameters is in focus.

5.2.1 General Calibration Procedure

The general calibration procedure consisted mainly of an initial calibration of each parameter needed for the SPM. After this was done, the Abaqus model of the R20 specimen was analyzed with the initial calibrated parameters. The results from the initial analyses were compared to the results from the lab. For a better correspondence, the material parameters were optimized by visual inspection of the results.

Plastic Dilation Parameter

The plastic dilation parameter, β, describes the change in volume in a material during plastic deformation. This parameter was calculated by

$$\beta = \frac{2-\rho}{1+\rho} \geq 1, \qquad \rho = \left| \frac{\varepsilon_T^p}{\varepsilon_L^p} \right|$$

where ρ is the plastic contraction parameter and ε_T^p and ε_L^p are the logarithmic plastic strains in the transverse and longitudinal direction. The β used in the initial calibration was calculated using the lab results from the R2 specimens, since these were the specimens that had the largest volumetric strain. The plastic dilation varies during a tensile test, while the parameter β is constant in SPM. Therefore, the plastic dilation parameter was determined from the mean value of the plastic contraction of the entire plastic region.

Elastic Parameters

Young's modulus is the relation between stress and strain in the linear elastic region of the material curve, and was calibrated by taking the mean of a curve fitted linear function and a secant in the elastic region of the true stress-log. longitudinal strain curve.

$$E = \frac{E_{Fit} + E_{Sec}}{2}$$

The elastic region is the linear region in the beginning of the true stress vs. true strain curve, but for many polymers, this region has a continuous change of stiffness. Therefore the elastic region was determined after careful inspection.

Poisson's ratio is the relation between the transverse and longitudinal elastic strains.

$$\nu = \left| \frac{\varepsilon_T^e}{\varepsilon_L^e} \right|$$

Since both Young's modulus and Poisson's ratio differed between the different geometries, maximum and minimum values for each parameter were calculated, as can be seen visually in Figure 5.6. The figures show the elastic response as measured in the experimental tests on the four different specimens made of the virgin material. The dashed black line and the continuous black line represent the maximum and minimum values of Young's modulus and Poisson's ratio, respectively.

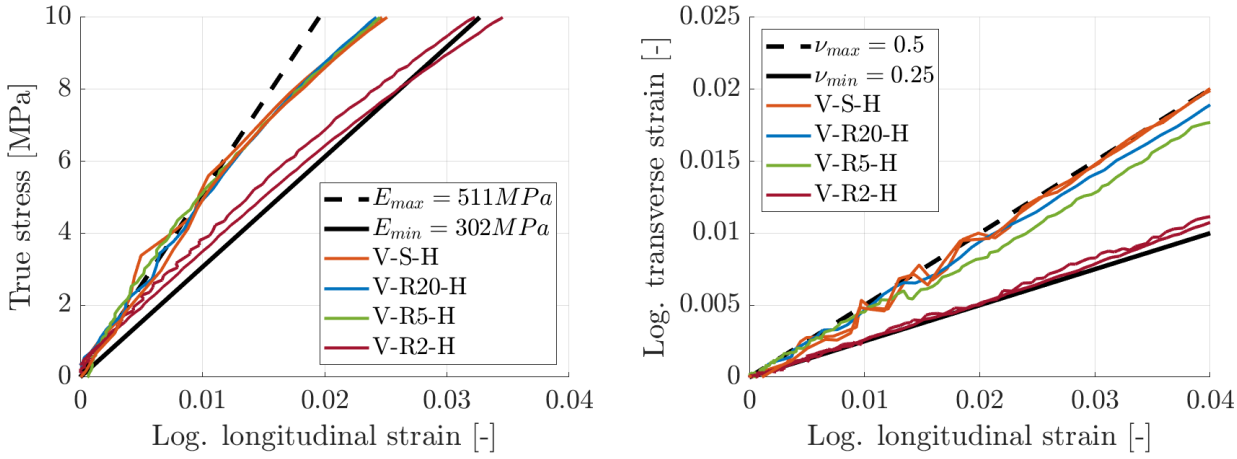

Figure 5.6: Visual representation of the Young's modulus and the Poisson ratio for different geometries.

Pressure Sensitivity

The pressure sensitivity parameter indicates the amount of pressure sensitivity in a material. It is defined as the ratio between the yield stress in compression and in tension. The yield stresses are found from the uniaxial tension and compression tests.

$$\alpha = \frac{\sigma_C}{\sigma_T}$$

Since compression tests were only performed with the virgin material at room temperature, the pressure sensitivity parameter had to be optimized by visual inspection for the specimens at -20°C and the degraded versions of the material.

Yield Stress

The yield stress was determined using a strain displacement that was equivalent to a 0.3% offset (Raghava 1972), as can be seen in Figure 5.7. The point where the offset of Young's modulus and the stress curve intersected was decided to be the yield stress. When deciding on a initial yield stress parameter, a reasonable value was chosen between the maximum and minimum of the tested specimens, smooth and with notches, for that material.

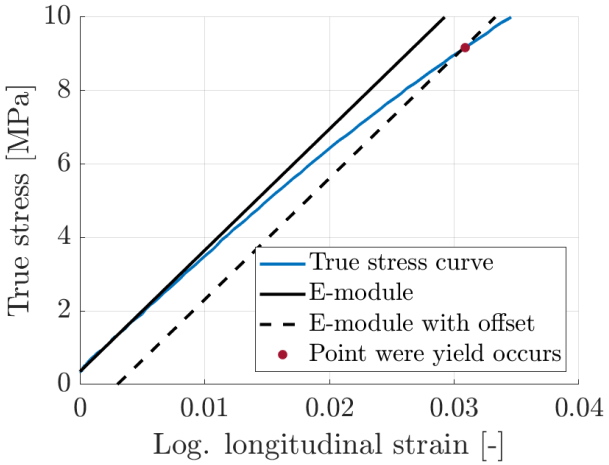

Figure 5.7: Determining the yield stress parameter.

Isotropic Hardening Parameters

As outlined in Section 2.2, the isotropic hardening was represented with Voce's hardening law where three terms were applied.

$$\sigma = \sigma_y + \sum_{i=1}^{3} Q_{Ri} \left(1 - \exp\left(-\frac{\theta_{Ri}}{Q_{Ri}} p\right)\right)$$

The hardening and softening parameters were calibrated by curve fitting Voce's law to the plastic stress vs. plastic strain curve. The smooth specimen was used to calibrate the initial hardening parameters for the virgin material, since it was assumed that the stress state was most uniaxial in this case. This meant that the equivalent plastic stress was the true stress in the longitudinal direction and the equivalent plastic strain was the true plastic strain. The curve fit application in MATLab was used.

A smooth specimen was only used when testing the virgin material. Therefore, to calibrate the hardening of the other material variations, the results from the R20 specimens were used.

This was due to the assumption that this specimen had a stress state that resembled uniaxial tension.

Optimizing the Parameters

After this initial calibration, the material model was applied in a finite element analysis (FEA) in Abaqus. Using the initial calibration as a baseline, the parameters were optimized by trial and error. All optimization was done using a quarter R20 specimen, similar to the one in Figure 5.1, and the main focus of the optimization procedure was on the isotropic hardening parameters, the plastic dilation parameter, and the pressure sensitivity parameter.

5.2.2 Virgin PA11 (V-H)

Plastic Dilation Parameter

As seen in Figure 5.8, the plastic dilation parameter for the virgin PA11 was calibrated to be $\beta = 1.15$ from the R2 specimen. This plot also shows that the plastic dilation varied for the entire duration of the test, and the parameter should therefore be considered not exact.

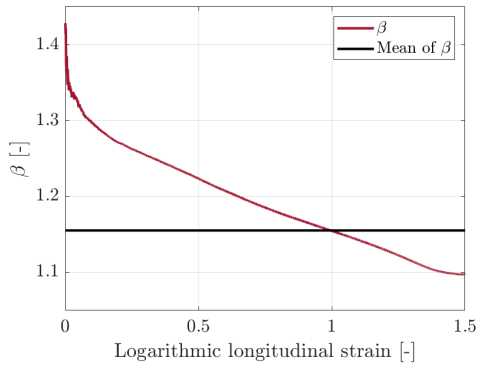

Figure 5.8: Plastic dilation for the virgin R2 specimen at room temperature.

Elastic Parameters

The maximum Young's modulus calibrated for the PA11 tested, $E = 511$ MPa, was for the R5 specimen, as seen in Table A.8. The calibrated minimum value, $E = 302$ MPa, was for the R2 specimen, as seen in Table A.12.

Poisson's ratio varied between $\nu = 0.5$ for the smooth specimen and $\nu = 0.25$ for the R2 specimen, as can be seen in Table A.4 and A.12.

Initial elastic parameters were chosen as $E = 400$ MPa and $\nu = 0.4$.

Pressure Sensitivity

As seen in the following equation, the pressure sensitivity was less than one for the virgin material, but since this parameter was required to greater or equal to one in the material model, it was set to one. This meant that the virgin material may not be pressure sensitive.

$$\alpha = \frac{\sigma_C}{\sigma_T} = \frac{7.8MPa}{9.6MPa} = 0.81 \tag{5.1}$$

Yield Stress

The scatter between the calculated yield stress parameters was low for the different geometries. The lowest yield stress was $\sigma_y \approx 8.5$MPa for the R5 specimen, and the highest yield stress was $\sigma_y \approx 10.5$MPa for the R20 specimen, as can be seen in Table A.8 and A.6. The initial yield stress parameter was decided to be $\sigma_y = 9$MPa.

Isotropic Hardening Parameters

The Voce parameters acquired from the curve fit can be seen in Table 5.1, and the fitted curve can be seen with the curve from the lab test in Figure 5.9.

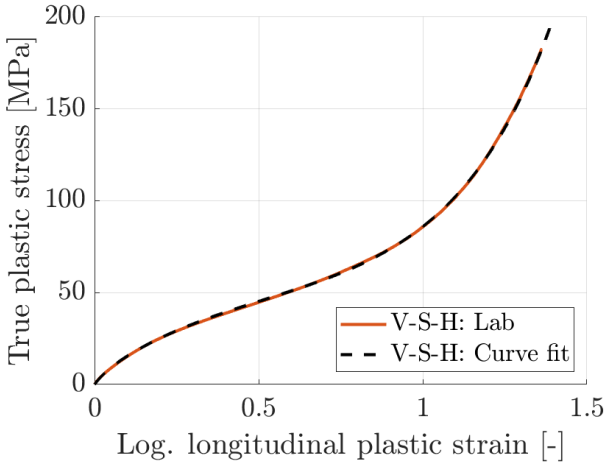

Figure 5.9: Comparison of the curve fit and test data from a smooth specimen.

Table 5.1: Voce parameters acquired from a curve fit of the smooth specimen.

Q_{R1} [MPa]	Θ_{R1} [-]	Q_{R2} [MPa]	Θ_{R2} [-]	Q_{R3} [MPa]	Θ_{R3} [-]
3.43	101.26	47.22	134.58	-1.34	4.53

Optimizing the Parameters

The initial values of the material parameters were, as explained earlier in this section, determined more or less from one or more material tests on the virgin material. The next step was to optimize the values of some parameters through numerical simulations of the R20 specimen.

Both the initial and optimized result can be seen in Figure 5.10, and the changed parameters are presented in Table 5.2, and are identified with red. Neither, E, ν or σ_y were changed in the optimization process.

The initial calibration lacked the locking behaviour that was apparent in this material, thus the isotropic hardening parameters had to be altered to increase the hardening late in the strain history. As can be seen, the optimized version corresponded less with regards to the diameter contraction. Since the stress matched well, it meant that the calibrated model was stiffer than in reality.

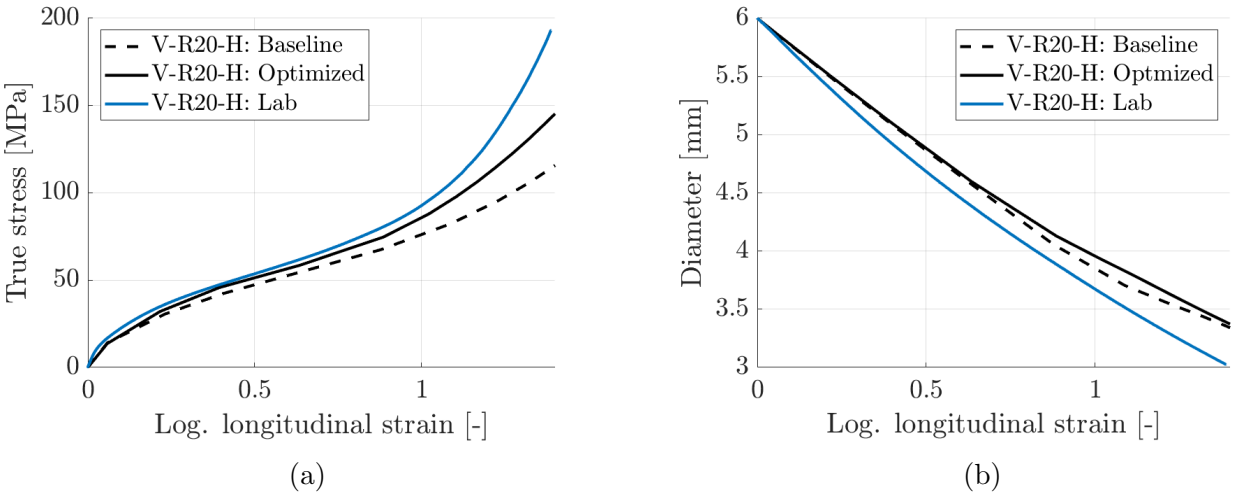

Figure 5.10: Comparison of the FEA results using the baseline and optimized calibration and the lab result (V-H).

Table 5.2: Material parameters (V-H) used for the initial and optimized simulation.

Parameter Unit	Q_{R1} [MPa]	Θ_{R1} [-]	Q_{R2} [MPa]	Θ_{R2} [-]	Q_{R3} [MPa]	Θ_{R3} [-]	β [-]	α [-]
Initial	3.43	101.3	47.2	134.6	-1.34	4.53	1.15	1.01
Optimized	15.4	101.3	32.2	134.6	-0.85	4.0	1.1	1.01

Check of Global Response

Due to focus being on the local behaviour when optimizing the material parameters, a quick check of the global response and of the volumetric strain was conducted, which gave the results as seen in Figure 5.11a and 5.11b.

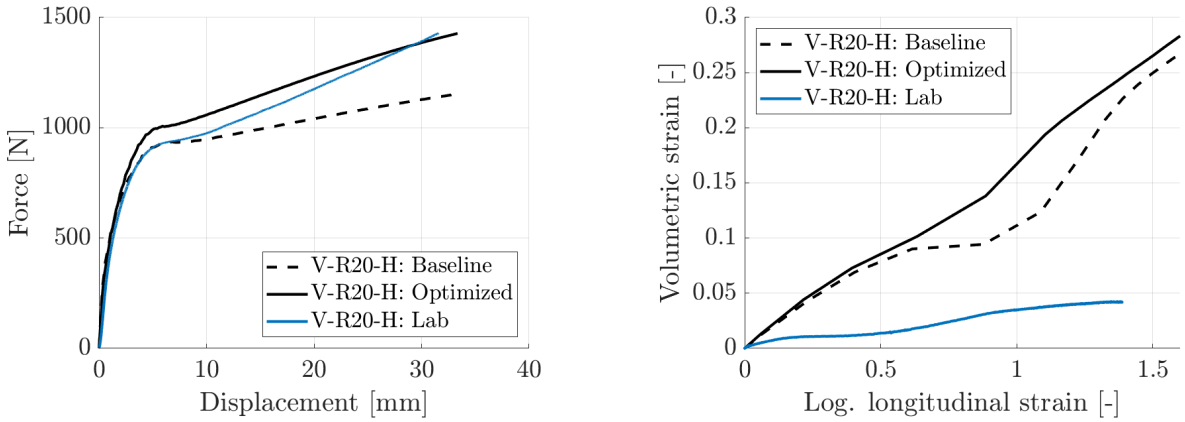

(a) (b)

Figure 5.11: Check of the global response and volumetric strain of the material model for virgin PA11 under room temperature.

The results from this control confirmed the assumption that the local and global response were well connected. Hence, it was chosen to only focus on the local response when calibrating a model. Further, the volumetric strain confirmed that the plastic dilation was too high for R20. This was expected because the plastic dilation parameter was determined from the R2 test. The R2 specimen exhibited much larger change of volume than what the R20 specimen did.

5.2.3 PA11 with Reduced Plasticizer Content (P-H)

The material parameters of the degraded material were determined using the same procedure as the virgin material. The major difference was that the isotropic hardening parameters, i.e., Q_{Ri} and Θ_{Ri}, were established using the results from the R20 specimen. As well as for the virgin material, the parameters were optimized through FEA on the R20 specimen.

Both the initial and the optimized result can be seen in Figure 5.12. The material parameters are found in Table 5.3. Initially, the model was too soft, and after $\varepsilon_L \approx 1$, the specimen hardened more than the simulation. The diameter reduction was fairly well represented. After optimizing the isotropic hardening parameters, the stress matched better. To increase the diameter reduction, the initial plastic dilation parameter was reduced.

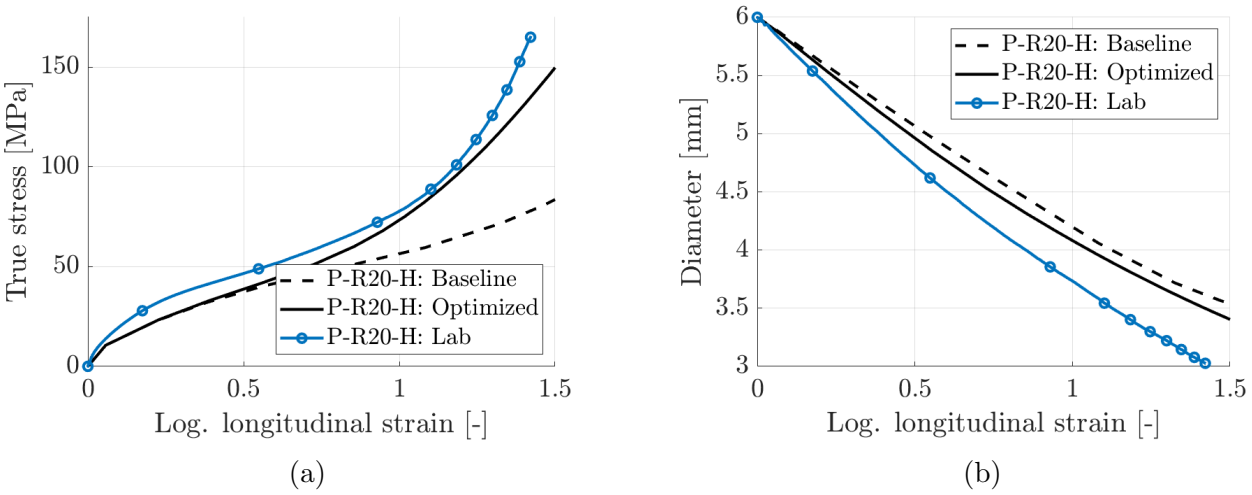

Figure 5.12: Comparison of the FEA results using the baseline and optimized calibration and the lab result (P-H).

Table 5.3: Material parameters (P-H) used for the initial and optimized simulation.

Parameter Unit	Q_{R1} [MPa]	Θ_{R1} [-]	Q_{R2} [MPa]	Θ_{R2} [-]	Q_{R3} [MPa]	Θ_{R3} [-]	β [-]	α [-]
Initial	46.7	106.5	2.1	66.7	-0.55	1.81	1.195	1.01
Optimized	46.7	106.5	2.1	66.7	-0.40	2.20	1.1	1.01

5.2.4 PA11 with Reduced Plasticizer Content and Reduced Molecular Weight (PW-H)

The calibration procedure outlined for the virgin material was employed here as well. Both the initial and the optimized results can be seen in Figure 5.13, where the material parameters can be seen in Table 5.4. For the initial calibration the diameter reduction did not correspond properly and the stress did not harden properly after yielding. To compensate for this, the exponential term of the Voce parameters was altered to simulate a locking behaviour. To decrease the plastic dilation, the plastic dilation parameter was decreased from the initial analytical value.

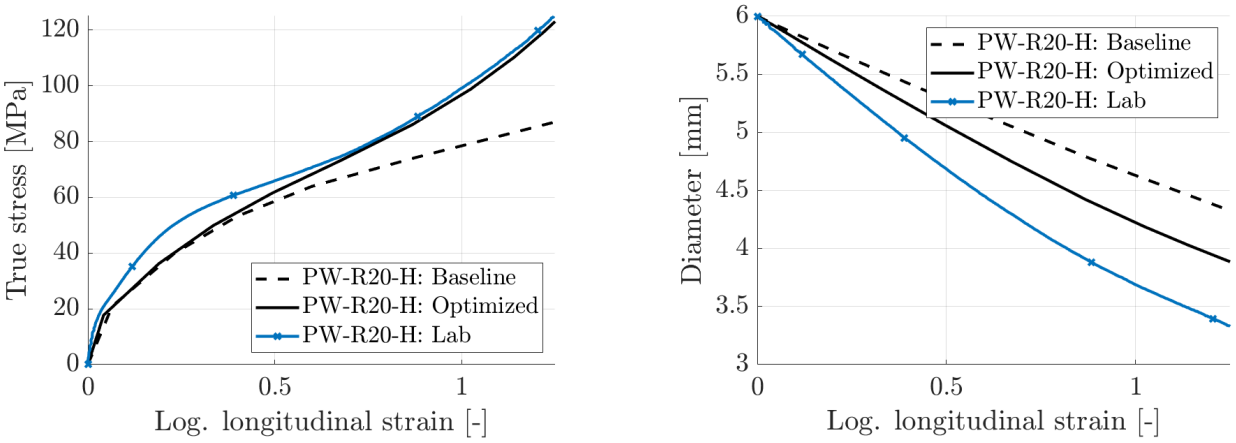

(a) (b)

Figure 5.13: Comparison of the FEA results using the baseline and optimized calibration and the lab result (PW-H).

Table 5.4: Material parameters (PW-H) used for the initial and optimized simulation.

Parameter Unit	Q_{R1} [MPa]	Θ_{R1} [-]	Q_{R2} [MPa]	Θ_{R2} [-]	Q_{R3} [MPa]	Θ_{R3} [-]	β [-]	α [-]
Initial	54.0	175.6	0.98	154.9	-5.6	7.4	1.38	1.01
Optimized	54.0	175.6	0.98	154.9	-4.0	10	1.20	1.01

5.2.5 PA11 with Reduced Molecular Weight (W-H)

To calibrate the baseline model, the same procedure for calibrating the parameters was used as for the virgin material. Both the initial and the optimized result can be seen in Figure 5.14, and the optimized parameters can be found in Table 5.5. The initial model was too soft and had too little diameter reduction. After optimizing the values, the stress matched better, being softer by approximately 5MPa, as well as the diameter which differed by less than 0.5mm due to a reduction of the plastic dilation parameter. Since the specimens for this degradation procedure failed in the fixtures, all the hardening parameters were positive, due to a lack of information regarding later hardening. All the other material variations had an exponential hardening term, so it is reasonable to assume that this model should have had one as well.

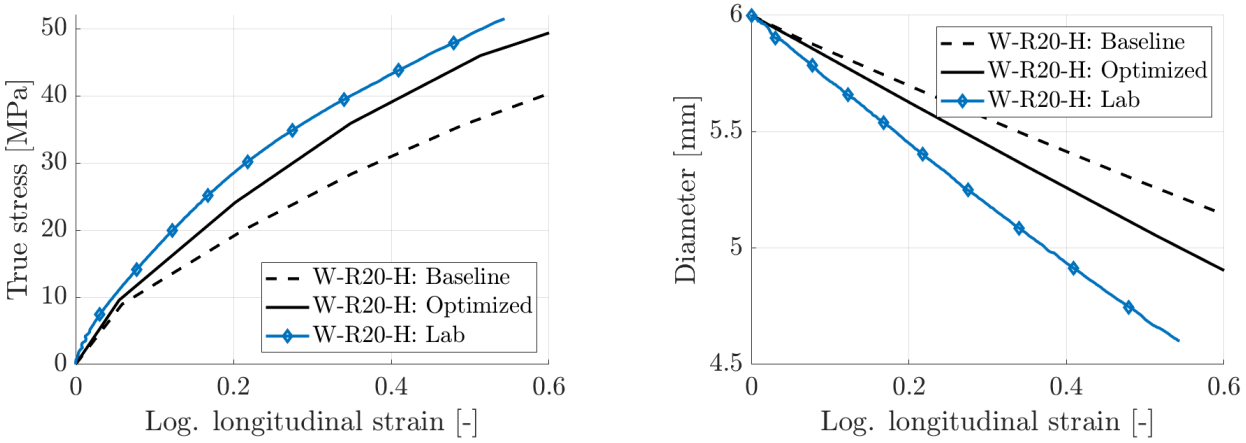

(a) (b)

Figure 5.14: Comparison of the FEA results using the baseline and optimized calibration and the lab result (W-H).

Table 5.5: Material parameters (W-H) used for the initial and optimized simulation.

Parameter Unit	Q_{R1} [MPa]	Θ_{R1} [-]	Q_{R2} [MPa]	Θ_{R2} [-]	Q_{R3} [MPa]	Θ_{R3} [-]	β [-]	α [-]
Initial	5.2	10.2	45.1	88.8	8.3	17.4	1.41	1.01
Optimized	5.2	20.2	45.1	150.8	8.3	30.4	1.20	1.01

5.2.6 Virgin PA11 at -20°C (V-C)

Since there was not implemented an option to include the effect of temperature in SPM, a new material model had to be calibrated for the materials at -20°C. These were calibrated employing the same procedure as with the virgin material. Both the initial and the optimized result can be seen in Figure 5.15, and the optimized parameters can be found in Table 5.6. The stress in the baseline was considered as a sufficient match. Hence, only the diameter reduction was prioritized when optimizing the parameters. By reducing the plastic dilation parameter, a more appropriate diameter reduction was achieved.

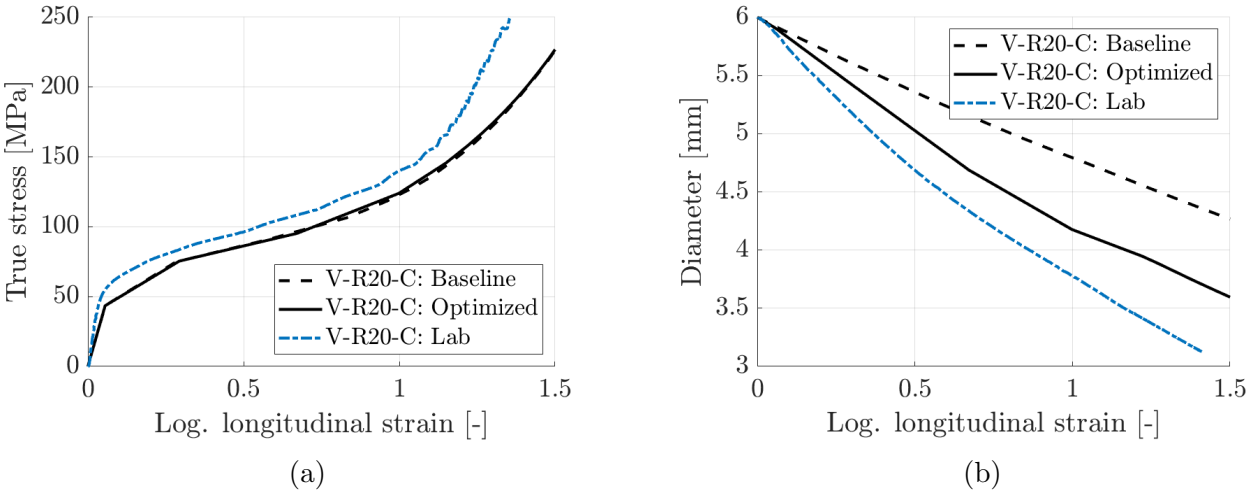

Figure 5.15: Comparison of the FEA results using the baseline and optimized calibration and the lab result (V-C).

Table 5.6: Material parameters (V-C) used for the initial and optimized simulation.

Parameter Unit	Q_{R1} [MPa]	Θ_{R1} [-]	Q_{R2} [MPa]	Θ_{R2} [-]	Q_{R3} [MPa]	Θ_{R3} [-]	β [-]	α [-]
Initial	40.5	257.9	11.3	958.9	-2.8	8.6	1.44	1.01
Optimized	40.48	257.9	11.32	958.9	-2.8	8.6	1.20	1.01

5.2.7 PA11 with Reduced Plasticizer Content at -20°C (P-C)

The calibration procedure remained the same as for the virgin material. Both the initial and the optimized result can be seen in Figure 5.16, and the material parameters are found in Table 5.7. The stress matched well, but the diameter reduction was too small, probably because of a too high plastic dilation parameter. As seen in the optimized curve, the diameter reduction corresponded better after reducing the plastic dilation parameter. By increasing the pressure sensitivity, a slightly more accurate material model was achieved with regards to stress.

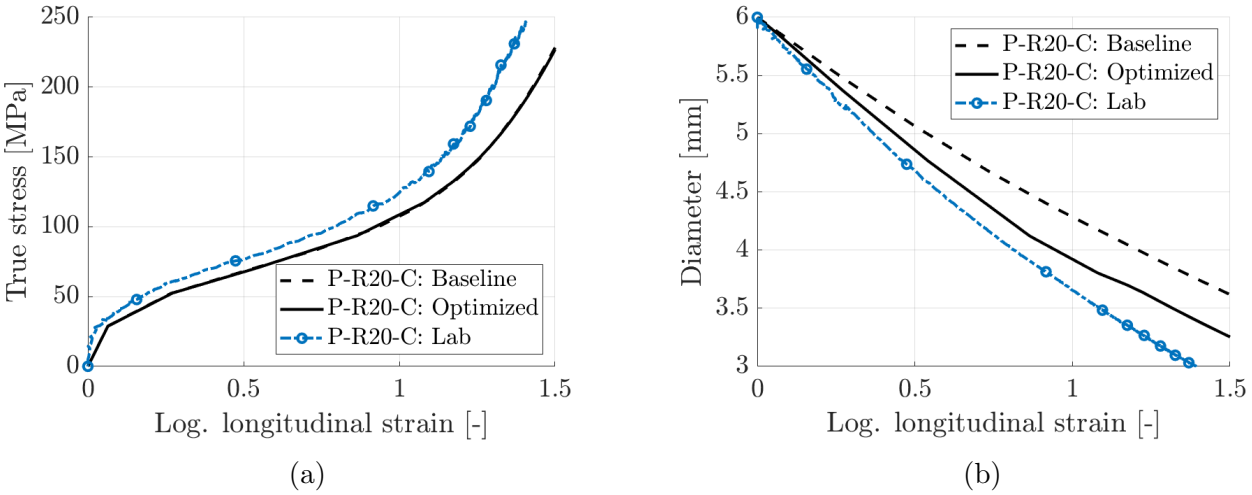

Figure 5.16: Comparison of the FEA results using the baseline and optimized calibration and the lab result (P-C).

Table 5.7: Material parameters (P-C) used for the initial and optimized simulation.

Parameter Unit	Q_{R1} [MPa]	Θ_{R1} [-]	Q_{R2} [MPa]	Θ_{R2} [-]	Q_{R3} [MPa]	Θ_{R3} [-]	β [-]	α [-]
Initial	251.3	70.42	20.02	252	-0.055	0.27	1.195	1.01
Optimized	251.3	70.42	20.02	252	-0.05	0.31	1.1	1.20

5.2.8 PA11 with Reduced Plasticizer Content and Molecular Weight at -20°C (PW-C)

The calibration for the last model was the same as earlier. Both the initial and the optimized result can be seen in Figure 5.17, and the material parameters can be found in Table 5.8. The initial calibration matched well with the stress from the lab results. However, the initial results differed at the diameter reduction, which suggested a reduction of the plastic dilation parameter. A reduction of the plastic dilation parameter gave an almost identical diameter reduction as in the lab.

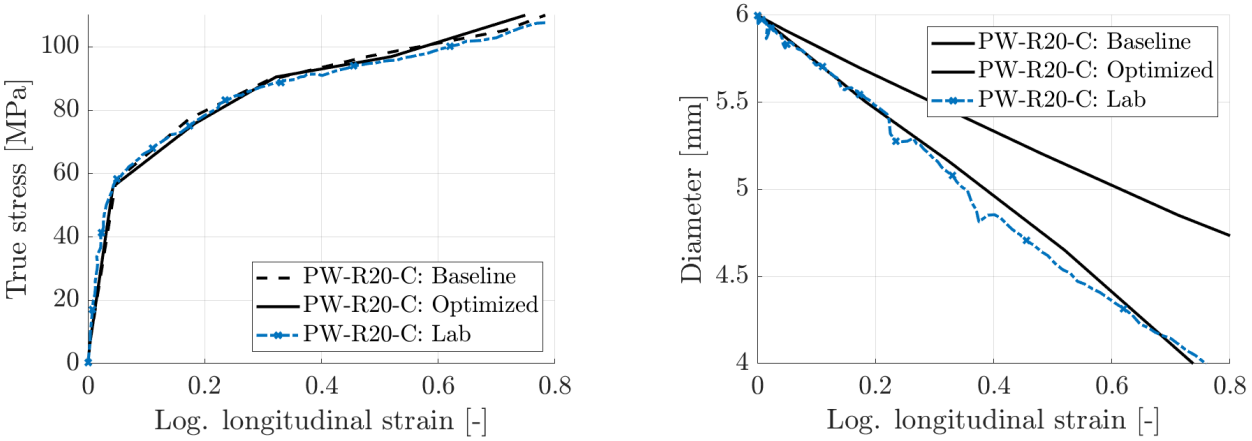

(a) Comparison between the stress curves of the simulations and the lab tests.

(b) Comparison between the diameter reduction of the simulations and the lab tests.

Figure 5.17: Comparison of the FEA results using the baseline and optimized calibration and the lab result (PW-C).

Table 5.8: Material parameters (PW-C) used for the initial and optimized simulation.

Parameter Unit	Q_{R1} [MPa]	Θ_{R1} [-]	Q_{R2} [MPa]	Θ_{R2} [-]	Q_{R3} [MPa]	Θ_{R3} [-]	β [-]	α [-]
Initial	11.5	1189	46.4	211.1	-0.13	0.74	1.33	1.01
Optimized	11.5	1189	46.44	211.1	-0.13	0.74	1.10	1.20

5.3 Calibration of the Drucker-Prager Model for Virgin PA11 (V-H)

The extended Drucker-Prager was mainly checked as a substitute for to the SPM. Hence, all the necessary tests needed to calibrate the material parameters were not conducted. Therefore, the parameters of the material model were found through trial and error.

Due to lacking lab results, a material model using the hyperbolic Drucker-Prager yield criterion was only established for virgin PA11 at room temperature. The best results achieved with this model can be seen in Figure 5.18a and 5.18b, using the parameters as listed in Table 5.9. The problems regarding this material model was that when reducing the dilation angle, the diameter would correspond with the lab tests, but the model would fail too early. The true stress was also too low, although this could probably have been solved by multiplying the tabular values for the hardening with a factor between 1 and 2.

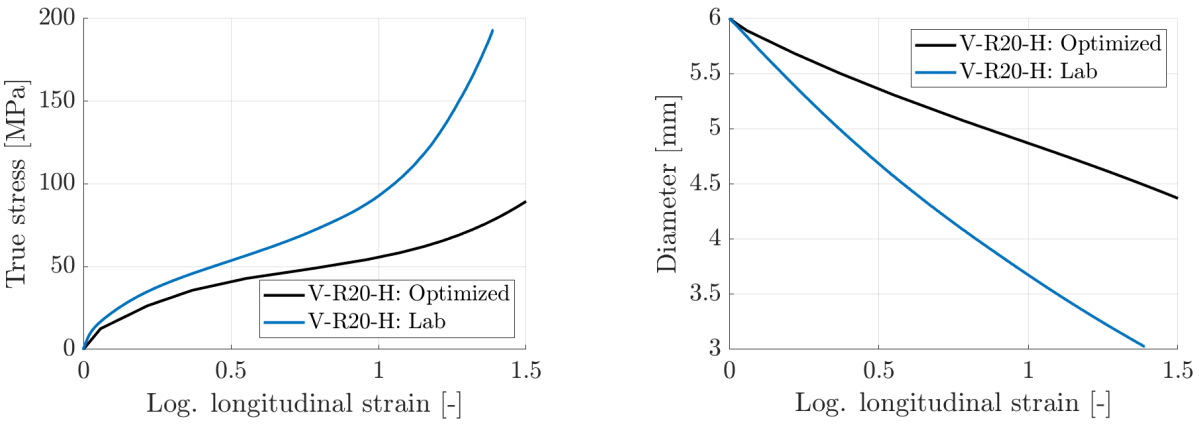

(a) (b)

Figure 5.18: Comparison of the calibration results from the Drucker-Prager model with the lab test.

Table 5.9: Parameters used to calibrate the virgin PA11 at room temperature using the hyperbolic extended Drucker-Prager material model.

Young's modulus	Poisson's ratio	Angle of friction	Init tension	Dilation angle
300	0.45	65	6	35

5.4 Sources of Error

Much of the calibration has been based on careful inspection, thus the yield stress parameters, Young's modulus and Poisson's ratios may be affected by human error.

The plastic dilation seemed to be too high for most cases. This is probably due to the plastic dilation not being constant in reality, and it was therefore not correct to assume it to be constant in the simulations. When the specimen failed early, little information was available regarding the plastic dilation parameter, making it difficult to detemine.

The pressure sensitivity was uncertain for most of the specimens due to a lack of compression tests. Therefore, some error is connected to this parameter.

As can be seen for the degraded specimens in Figure A.14 through A.23, the plastic strain rate is usually not equal to the nominal strain rate. Since no tests were conducted to analyze the rate sensitivity for the degraded materials, error may come from a lack of a reference strain rate and rate sensitivity parameter.

5.5 Discussion and Conclusion

Figure 5.19 shows the values of Young's modulus and yield stress as found from the calibration of parameters from the experimental tests. As can be seen in Figure 5.19, identical tests (i.e., number 1 and 2, 5 and 6, 7 and 8 and 24 and 25) gave almost identical yield stress and Young's modulus. Thus the scatter between replicates was limited. This was also observed in Chapter 4.

The calibrated yield stress from virgin PA11 had a difference of 2 MPa between minimum and maximum yield stress. When the virgin material was tested at -20°C, the difference increased to 20 MPa. This behavior was observed in the PA11 with reduced plasticizer content as well. A reason for this, was suspected to be an increase in pressure sensitivity.

The two compression results showed a lower yield stress compared to the tension tests (V-S-H). The SPM and the Drucker-Prager model require the material to have a higher, or equal, yield stress in compression than tension. However, the compression tests were only conducted for virgin material, which experienced less stress triaxility than the degraded specimens. The initial estimated pressure sensitivity deviates from the underlying assumptions of both material

models. This deviation was also seen by Engebretsen (2017).

Table 5.10 shows the optimized parameters for all the material models. Some tendencies were present. The yield stress, as well as Young's modulus, increased approximately three times when the materials temperature was reduced to -20°C. Almost all the variations had two hardening terms and one exponential hardening terms, except for the PA11 with reduced molecular weight, which failed in the fixtures at an early stage. It was reasonable to believe that also this one could have an exponential hardening term. All four material variations, both at warm and cold conditions, experienced plastic dilation.

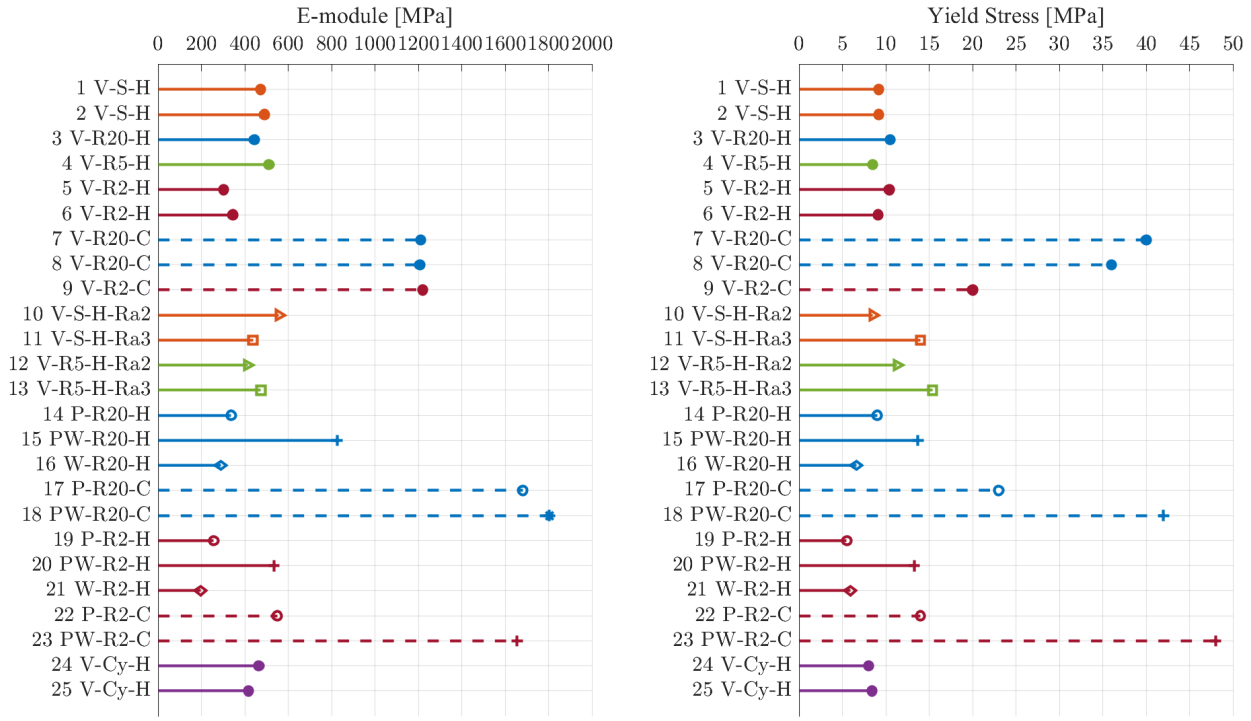

Figure 5.19: Results of the Young's modulus and the yield stress for the material tests conducted.

Table 5.10: Optimized material parameters for all the tested variations of PA11.

Material Model		**V**	**P**	**PW**	**W**	**V-C**	**P-C**	**PW-C**
σ	[MPa]	9	7	13.5	6.3	30	18.5	45
E	[MPa]	350	300	700	240	1100	1000	1700
ν	[-]	0.4	0.3	0.3	0.325	0.27	0.35	0.35
Q_{R1}	[MPa]	15.4	46.7	0.98	5.2	40.5	251.3	11.5
Θ_{R1}	[-]	101.3	106.5	154.9	20.2	257.9	70.4	1189.0
Q_{R2}	[MPa]	32.22	2.1	54.0	45.1	11.3	20.0	46.4
Θ_{R2}	[-]	134.6	66.7	175.6	150.8	958.9	252.0	211.1
Q_{R3}	[MPa]	-0.85	-0.40	-4.0	8.33	-2.83	-0.05	-0.13
Θ_{R3}	[-]	4.0	2.2	10.0	30.4	8.6	0.3	0.7
β	[-]	1.1	1.1	1.2	1.2	1.2	1.1	1.1
α	[-]	1.01	1.01	1.01	1.01	1.01	1.20	1.20

The R20 specimen experienced little volumetric strain, i.e., volume growth, thus it's plastic dilation was too small. The model was therefore expected to not be affected by having a high plastic dilation parameter. This was proven to be false, and the R20 numerical simulations were greatly affected by the plastic dilation parameter. Because of this behavior, the calibrated plastic dilation would always be too high for the R20 specimen.

The optimization was performed through careful inspection and manually changing reasonable parameters based on experience. This could have been done more comprehensively by calibrating for more specimens than just the R20 and by taking the global response into account.

Part III

Validation and Conclusion

6 Validation: Numerical Simulation

This chapter presents the validation of the calibrated material models. Since the four different specimens, smooth, R20, R5, and R2, were assumed to have entirely different stress states during tensile loading, it was reasonable to use them as validation. If the numerical model could represent the results from the lab for all four geometries, the model was assumed as validated.

As described in Chapter 5, the notched specimen with a radius of 20mm was used to optimize all the initial calibrated models. It can be recalled that the plastic dilation parameter was calibrated from the R2 specimens' results, and was therefore not optimized further for the R20 specimen. Hence, in this chapter the notched specimen with a radius of 2 mm is used to validate the models. The material model for virgin specimens at room temperature has also been validated by comparing a notched specimen of 5 mm and a smooth specimen.

As validation, the simulations have been compared with the lab experiments. Due to the amount of different material models that have been established, an in depth validation of the virgin PA11 under room temperature is first described. The remaining six material models are touched upon after this, but in a condensed form with the same layout seen in Chapter 5. The results used for comparing results are true stress vs log. longitudinal strain and diameter vs log. longitudinal strain. In addition, volumetric strain vs log. longitudinal strain and force vs displacement will be presented for the in depth validation of the virgin material at room temperature.

6.1 Validation of the SIMLab Polymer Model

6.1.1 Virgin PA11 (V-H)

The model for virgin PA11 at room temperature was tested with four different geometries in tension, one smooth and three notched. The geometries had approximately identical true stress vs. log. longitudinal strain curves until $\varepsilon_L = 0.5$, where smoother specimens started hardening earlier. The simulations were not able to capture this, as seen in Figure 6.1. It was to stiff for the R2 specimen, almost exact for the R5 specimen, and too soft for the smooth specimen. It is recalled from the calibration in Section 5.2.2 that the R20 specimen was too soft.

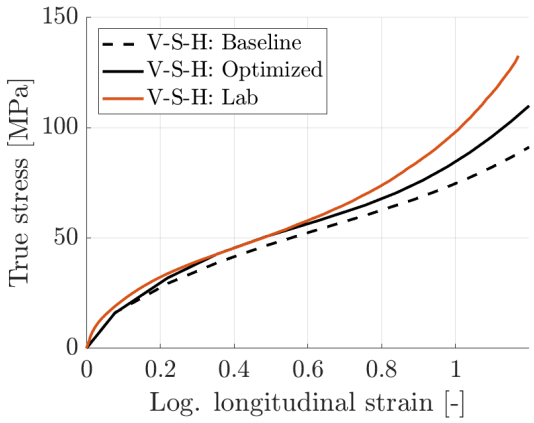

(a) Smooth specimen.

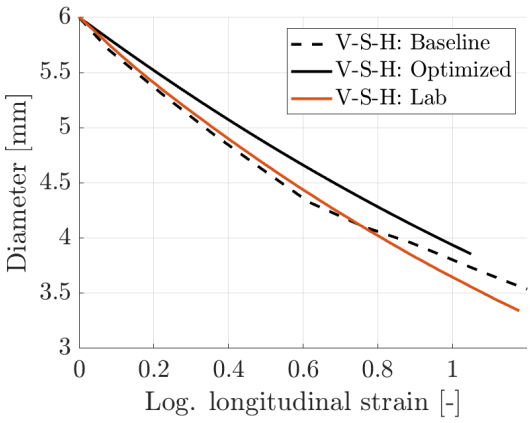

(b) Smooth specimen.

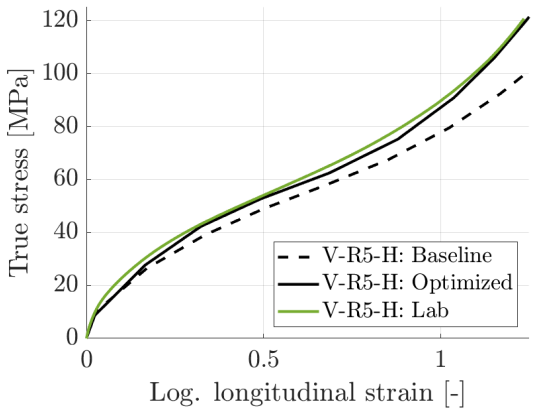

(c) Notched R5 specimen.

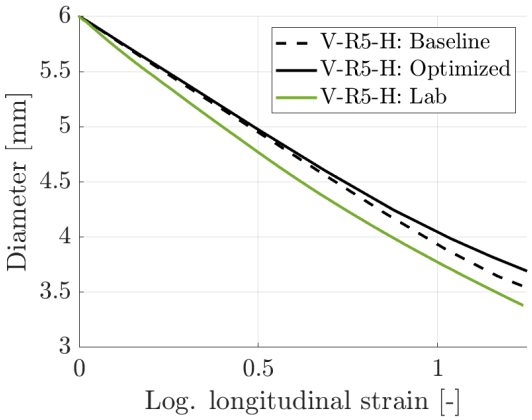

(d) Notched R5 specimen.

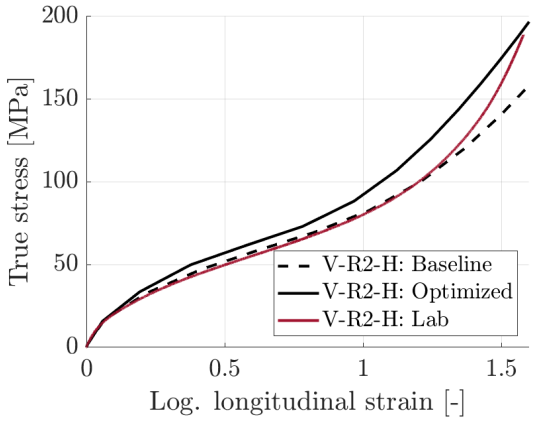

(e) Notched R2 specimen.

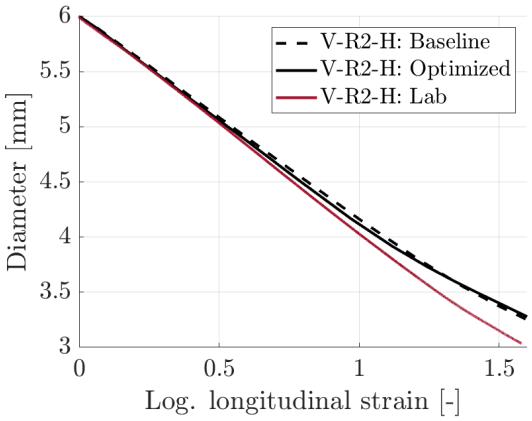

(f) Notched R2 specimen.

Figure 6.1: Validation results of the material model for virgin PA11 at room temperature.

The diameter reduction corresponded reasonably well in all cases in Figure 6.1. However, the baseline was seemingly better in some cases, as seen in Figure 6.1b and Figure 6.1d.

The simulated models were in general too stiff as components in the baseline analysis. This was due to the fixtures in the model being closer to the notch than in reality. This was fixed for the optimized simulations. The global response of the validated virgin R2 specimen at room temperature can be seen in Figure 6.2a. It was observed that the response was slightly stiffer than the lab results. This corresponded well with what was observed in Figure 6.1f and 6.1e. The force had to be higher for the stress to match, since the area of the simulated specimen was higher.

The volumetric strains from the simulated virgin R2 specimen at room temperature is presented in Figure 6.2b. The result matched well with reality, but the model predicted a monotonic increase in volumetric strain. For most specimens, the volumetric strain fluctuated at a constant level at high strains. This was a behavior the material model could not simulate due to the constant plastic dilation parameter. Furthermore, it is recalled that for smoother specimens the volumetric strain decreased. Hence, since the plastic dilation parameter was constant in the simulations, the volumetric strains would always match better for specimens with smaller notch radiuses than for smoother specimens.

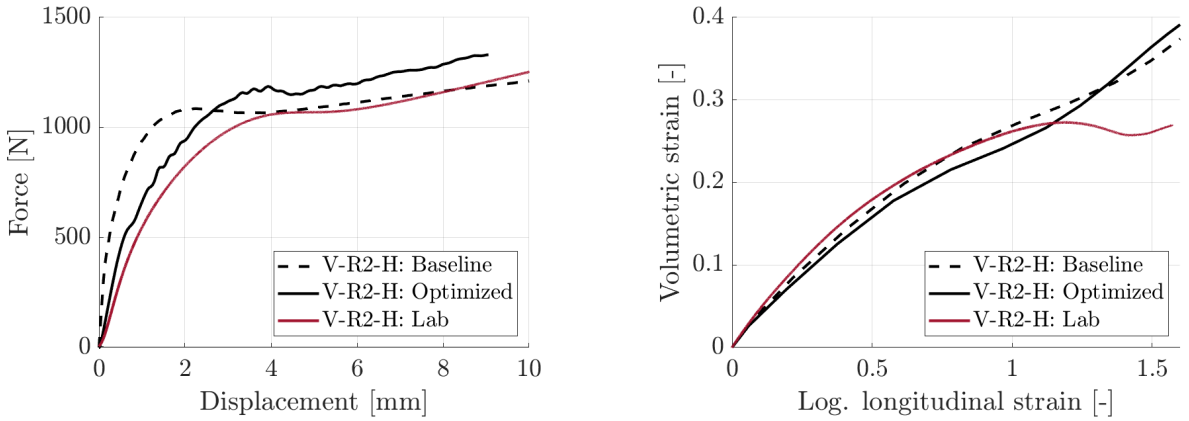

Figure 6.2: Validation of the global response and volumetric strain of the material model for virgin PA11 under room temperature.

6.1.2 PA11 with Reduced Plasticizer Content (P-H)

For the R2 specimen, the stresses matched until $\varepsilon_L = 0.6$. The simulation hardened too early which gave a too stiff response. The diameter reduction matched well until $\varepsilon_L = 1.0$, where the simulation seemed to suddenly get a lower gradient, as seen in Figure 6.3b.

The calibrated material model yielded too early for the R20 specimen, as recalled from Section 5.2.3 and seen in Figure 6.3c. After yielding, the real specimen hardened more than the simulation. The diameter reduction was too small.

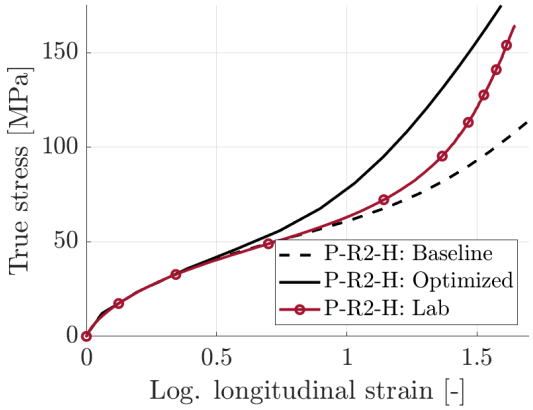

(a) Validated R2 specimen.

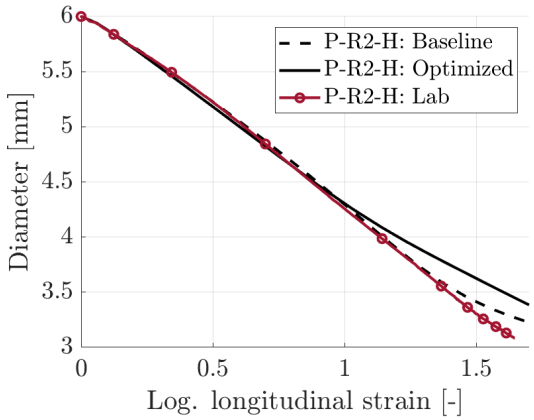

(b) Validated R2 specimen.

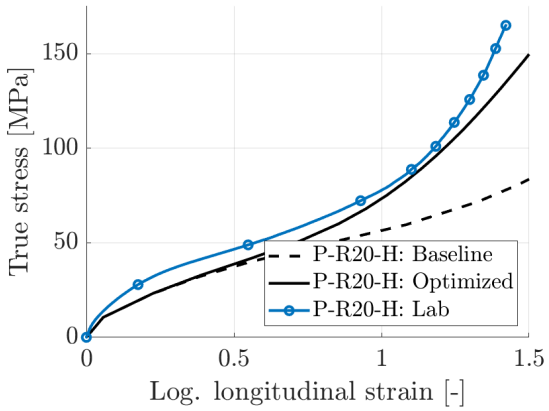

(c) Calibrated R20 specimen.

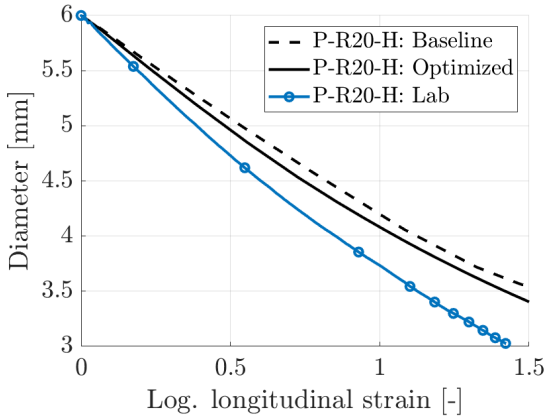

(d) Calibrated R20 specimen.

Figure 6.3: Validation results of the material model for PA11 with reduced reduced plasticizer (P-H). The calibration results from Chapter 5 are replicated for comparison.

6.1.3 PA11 with Reduced Plasticizer Content and Molecular Weight (PW-H)

From Figure 6.4a, it can be seen that the true stress from the optimized R2 specimen corresponded well for low strains, but deviates for larger strains . The match between the diameter from the lab and simulation was almost a perfect match for the R2 model, as seen in Figure 6.4b.

The hardening matched well for the calibrated R20 specimen, as recalled from Section 5.2.4. Although, in the beginning, it seems as if it yields to early. Furthermore, the diameter reduction was too low.

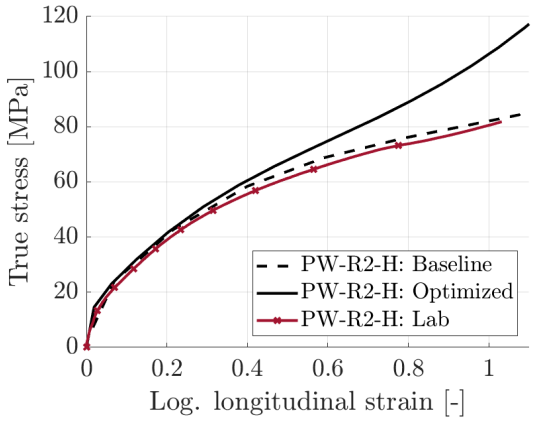

(a) Validated R2 specimen.

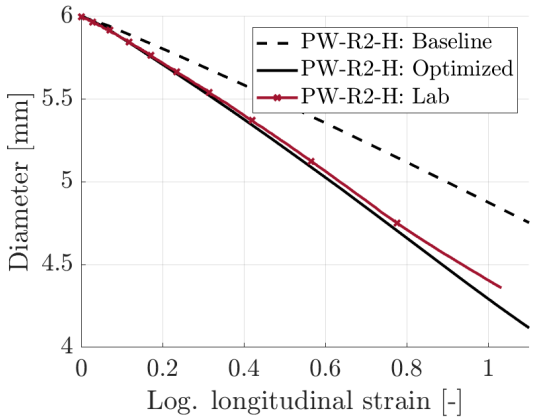

(b) Validated R2 specimen.

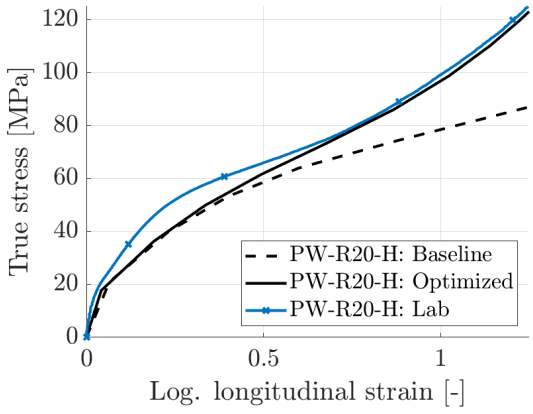

(c) Calibrated R20 specimen.

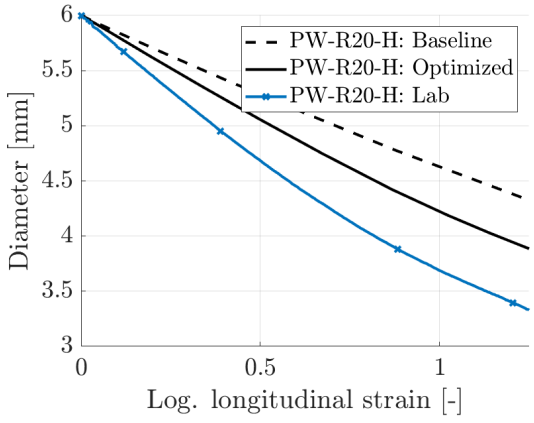

(d) Calibrated R20 specimen.

Figure 6.4: Validation results of the material model for PA11 with reduced reduced plasticizer and molecular weight (PW-H). The calibration results from Chapter 5 are replicated for comparison.

6.1.4 PA11 with Reduced Molecular Weight (W-H)

The calibrated R2 specimen had a good match between the physical experiment and the simulation as seen in Figure 6.5a and 6.5b. The simulation was too stiff, but the diameter reduction was almost identical with a slight difference of 0.05mm at the end.

As seen previously in Section 5.2.5, the curvature of the stress in the R20 simulation matched well with the lab, but had a slightly softer response. The diameter reduction did not match, as the diameter was rapidly decreasing in the test, but not in the simulation.

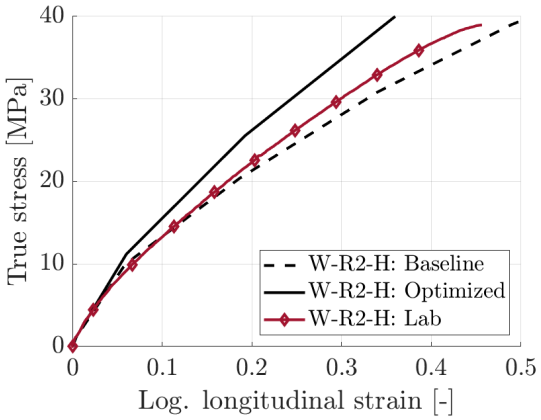

(a) Validated R2 specimen.

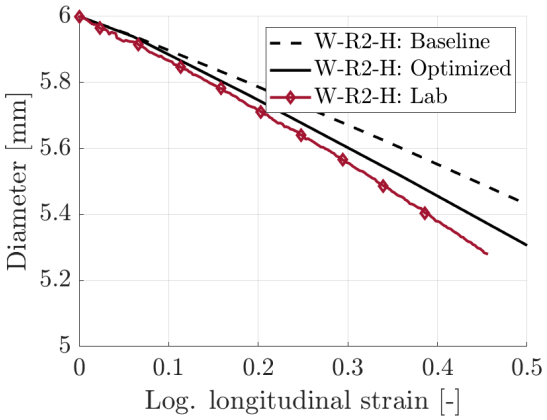

(b) Validated R2 specimen.

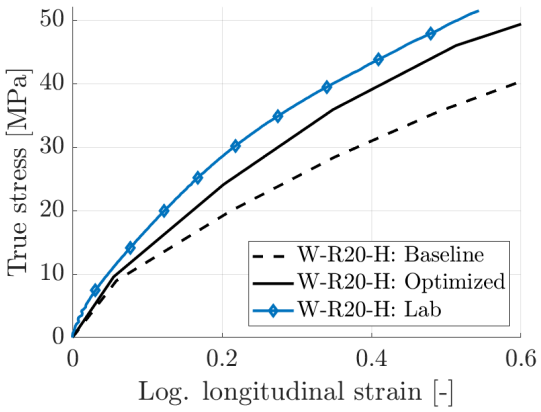

(c) Calibrated R20 specimen.

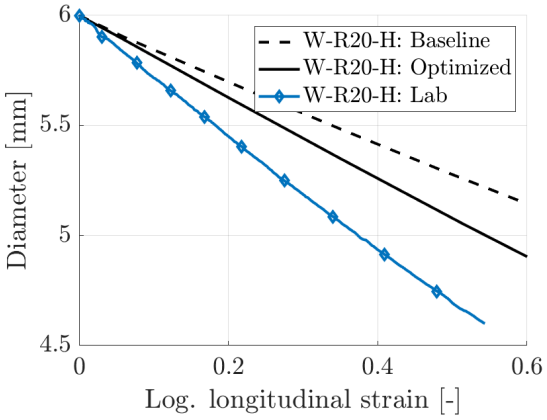

(d) Calibrated R20 specimen.

Figure 6.5: Validation results of the material model for PA11 with reduced molecular weight (W-H). The calibration results from Chapter 5 are replicated for comparison.

6.1.5 Virgin PA11 at -20°C (V-C)

The numerical model matched well for the R2 specimen, as seen in Figure 6.6a and 6.6b. The difference was less than 0.05mm in diameter and 5MPa in stress. More sampling points should have been applied to the model, since the curve was rough and could not properly show the curvature of the stress curve.

Recalled from Section 5.2.6, the initial calibrated model of R20 was slightly soft, as seen in Figure 6.6c. Furthermore, the initial calibrated diameter should have contracted even more for the R20 specimen.

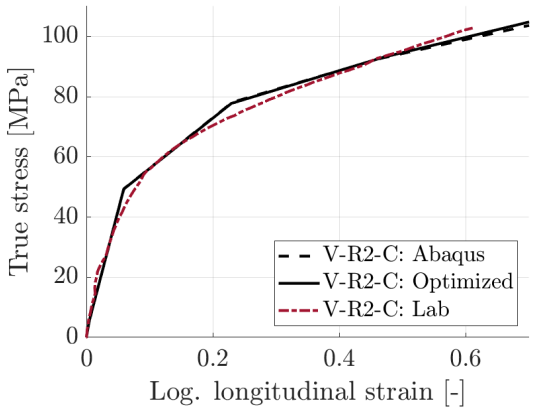

(a) Validated R2 specimen.

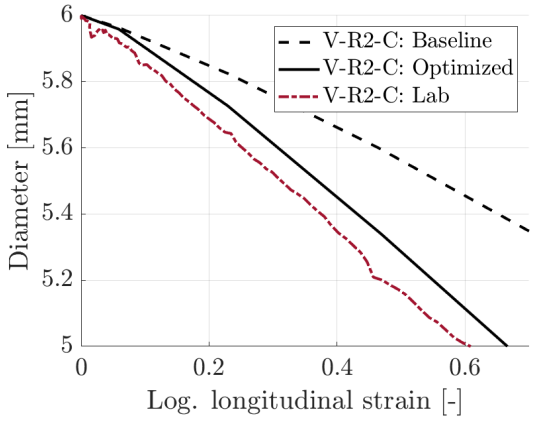

(b) Validated R2 specimen.

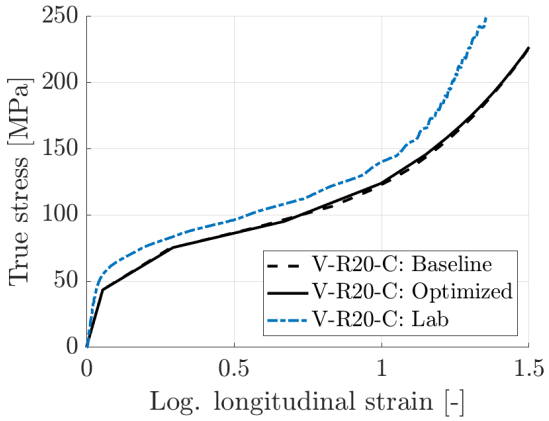

(c) Calibrated R20 specimen.

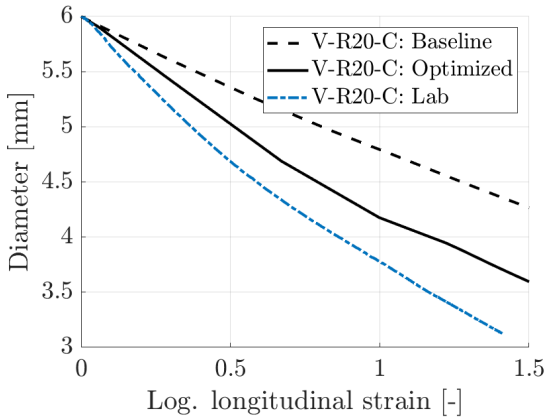

(d) Calibrated R20 specimen.

Figure 6.6: Validation results of the material model for virgin PA11 at -20°C (V-C). The calibration results from Chapter 5 are replicated for comparison.

6.1.6 PA11 with Reduced Plasticizer Content at -20°C (P-C)

The response from the simulation matched well for the R2 specimen, as seen in Figure 6.7a. The diameter reduction, as seen in Figure 6.7b, matched quite well, although they started diverging after $\varepsilon_L = 1$. This may be connected to the difference in the stress that happened at the same time.

The stress response from the simulation was too low for the calibrated R20 specimen, as previously observed in Section 5.2.7. The diameter reduction was also too low.

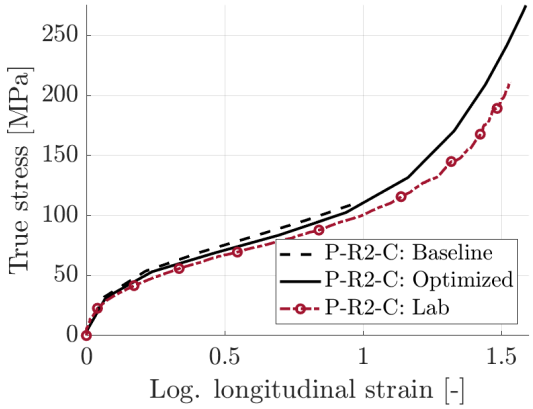

(a) Validated R2 specimen.

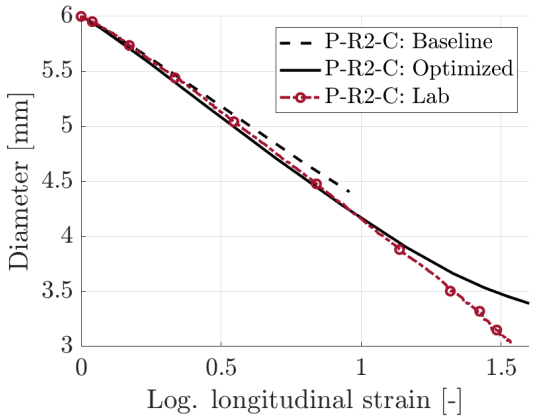

(b) Validated R2 specimen.

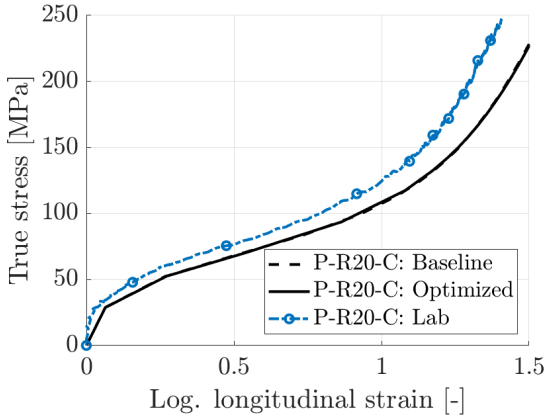

(c) Calibrated R20 specimen.

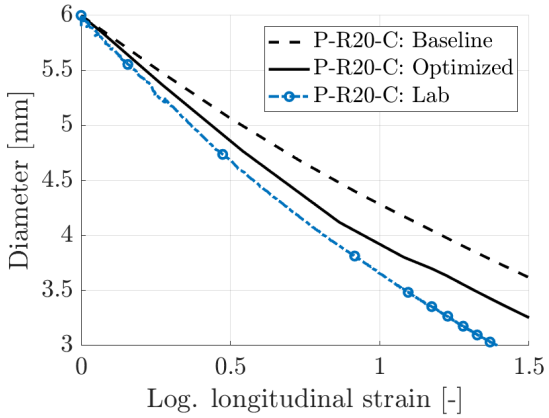

(d) Calibrated R20 specimen.

Figure 6.7: Validation results of the material model for PA11 with reduced reduced plasticizer at -20°C (P-C). The calibration results from Chapter 5 are replicated for comparison.

6.1.7 PA11 with Reduced Plasticizer Content and Molecular Weight at -20°C (PW-C)

As for the R2 specimen, neither the diameter reduction nor the stress was a decent fit, as seen in Figure 6.8a and 6.8b. The stresses were too stiff and the simulations had too much diameter reduction. The low similarity could be due to the specimen failing quite early, giving an unusual behaviour.

The stresses were almost identical for the R20 specimen, as well as for the diameter reduction, as recalled from Section 5.2.8.

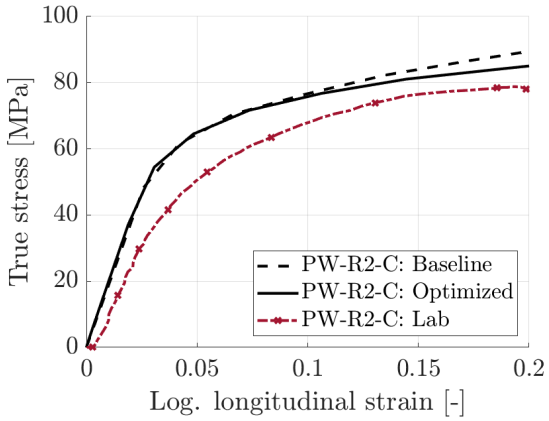

(a) Validated R2 specimen.

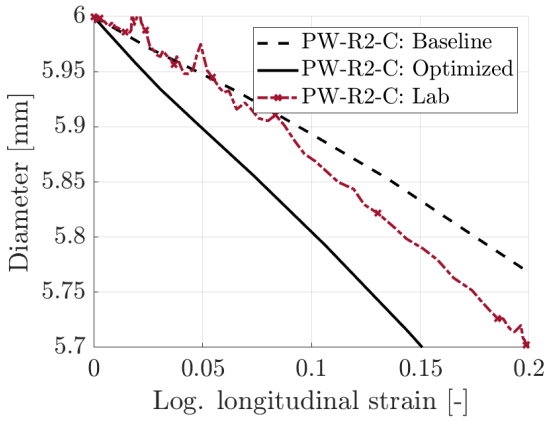

(b) Validated R2 specimen.

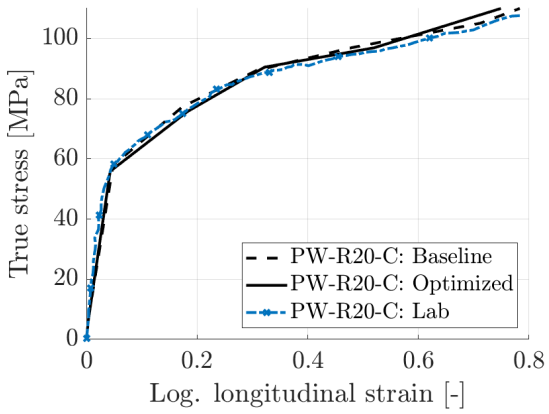

(c) Calibrated R20 specimen.

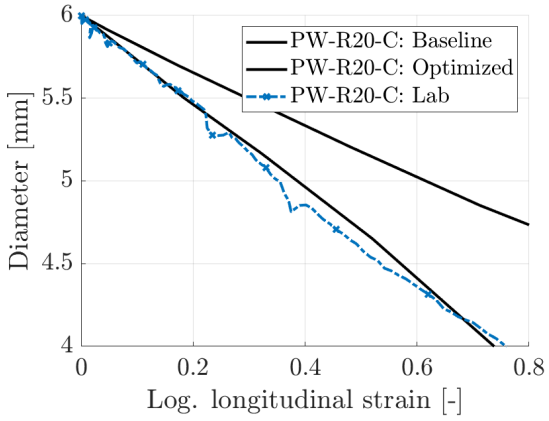

(d) Calibrated R20 specimen.

Figure 6.8: Validation results of the material model for PA11 with reduced reduced plasticizer and molecular weight at -20°C (PW-C). The calibration results from Chapter 5 are replicated for comparison.

6.2 Validation of the Drucker-Prager Model for Virgin PA11 (V-H)

As recalled from Section 5.3, the Drucker-Prager model was not a suitable choice for PA11 due to low hardening and low diameter reduction. The hyperbolic extended Drucker-Prager material model was not able to capture the behavior of the virgin PA11 for the other specimens either. This can be seen in the stress curves, 6.9a, 6.9c and 6.10a. The models were not hardening enough later in the strain history and the diameter reduction was almost half of what it was in reality, as seen in Figure 6.9b, 6.9d and 6.10b.

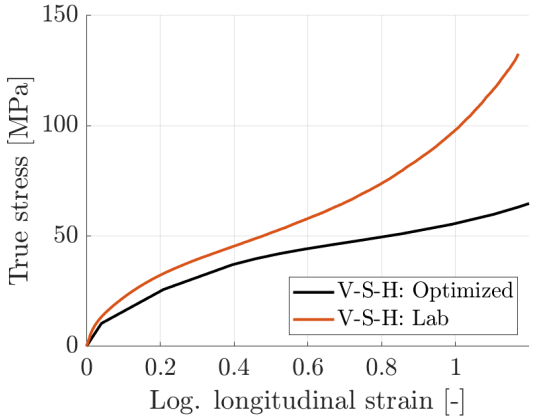

(a) Smooth specimen.

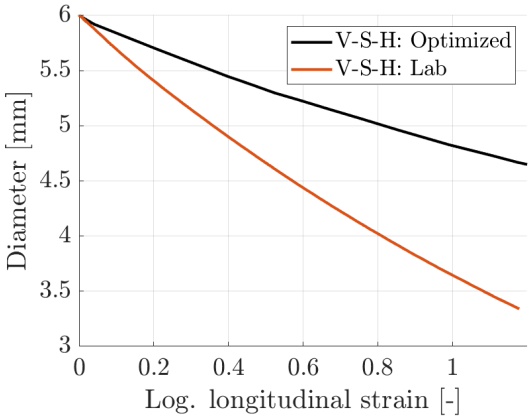

(b) Smooth specimen.

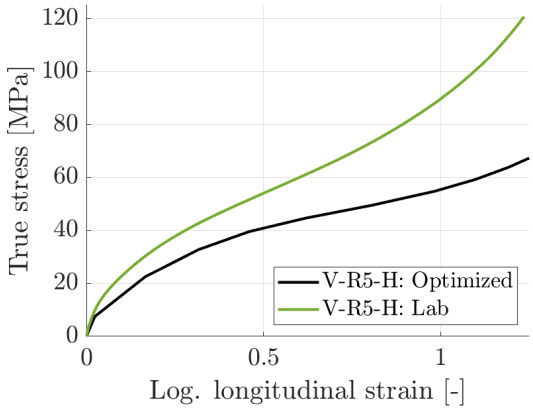

(c) Notched R5 specimen.

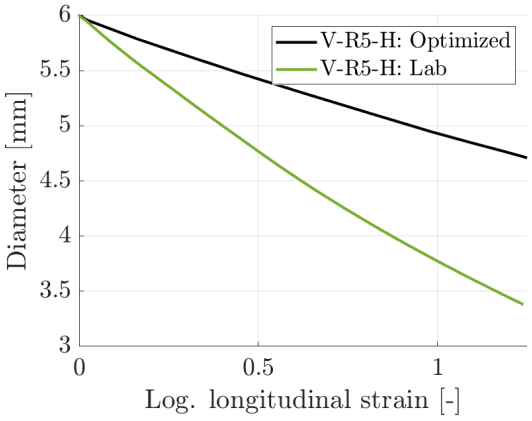

(d) Notched R5 specimen.

Figure 6.9: Validation results of the extended Ducker-Prager material model for virgin PA11.

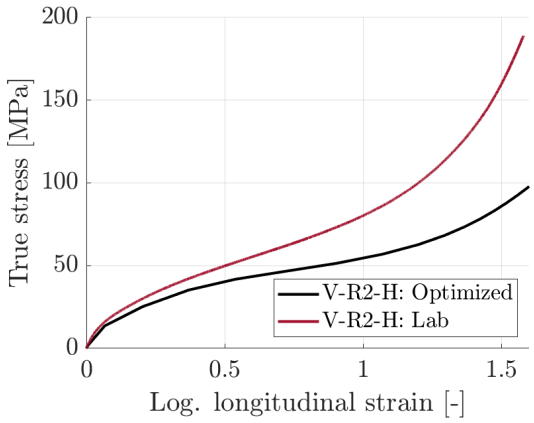

(a) Notched R2 specimen.

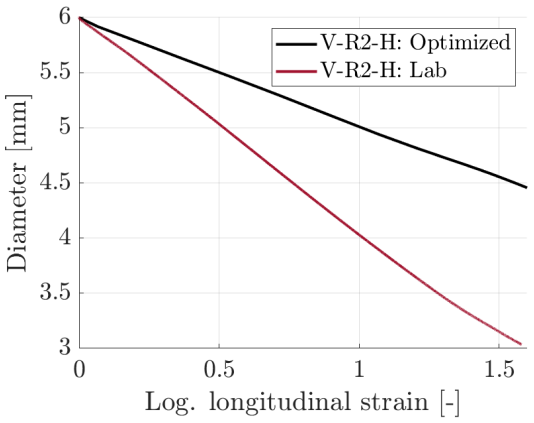

(b) Notched R2 specimen.

Figure 6.10: Validation results of the extended Ducker-Prager material model for virgin PA11.

6.3 Validation of the Abaqus Model

To validate the Abaqus model, the quarter model was expanded to a three dimensional model of the entire specimen, as previously seen in Figure 5.2. The results from the simplified V-R2-H analysis were used as comparison to what was thought to be the most correct simulation of reality. The mesh configuration remained the same as for the simplified specimen, see Section 5.1. Both ends of the modelled specimen had a coarse mesh with target element size of 2mm×2mm×2mm and a finer mesh in the middle with a target element size of 0.2mm×0.2mm×0.2mm. The number of elements in each model can be seen in Table 6.1. The comparison was between the diameter reduction and true stress, the two most important aspects of this thesis. As can be seen in Figure 6.11, the left graph shows no discrepancies between the simplified and full model with regards to the stress. Although the diameter reduction was slightly less for the full model, approximately 3% at the end, the simplified model was considered adequate.

Table 6.1: Number of elements in each model.

Model	Simplified R2	Simplified R5	Simplified R20	Simplified Smooth	Full R2
Number of elements	10 398	53 154	16 775	55 797	169 400

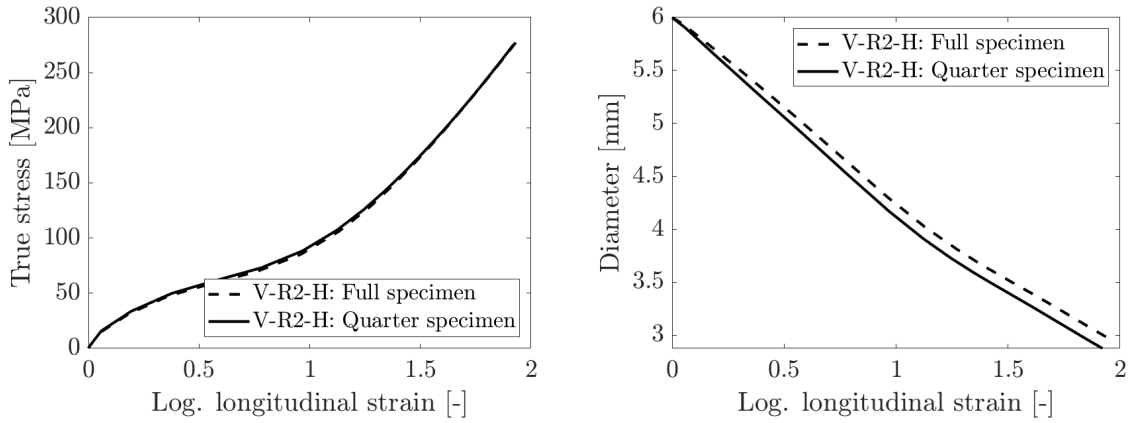

Figure 6.11: Comparison between the results from the simplified and the full model.

When obtaining data from the completed analysis, the strain and stress were obtained from an element at the edge of the center of the specimen. A check was done to ensure that this stress corresponded with the true stress calculated from the force and the true area, which can be seen in Figure 6.12. Due to the minor difference in stress, the procedure was believed to be accurate within reason.

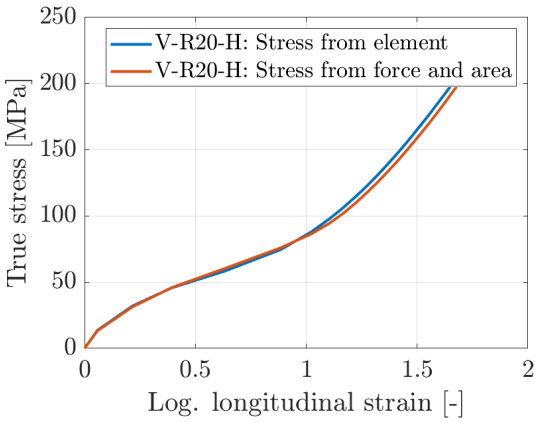

Figure 6.12: Comparison between the stress obtained from an element and the stress calculated from the total force and the true area.

A check of the longitudinal stress and hydrostatic pressure was done by visual inspection of the full and the simplified specimen, as seen in Figure 6.13 and 6.14. In these figures, red indicates the highest value, blue indicates the lowest, and green is approximately in the middle. It can be noticed that the distribution were similar. This method was also used to confirm that the largest stress was at the surface of the specimen.

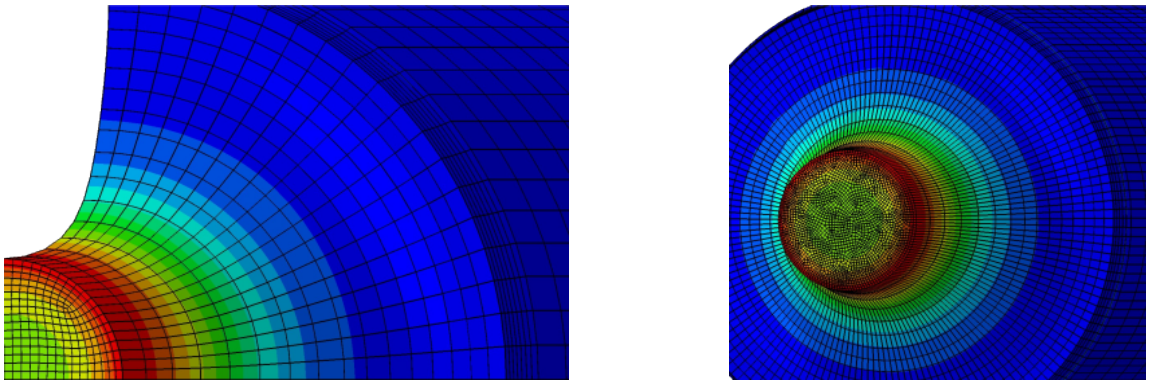

Figure 6.13: Visual comparison of the stress distribution from an arbitrary cross section of the simplified and full model.

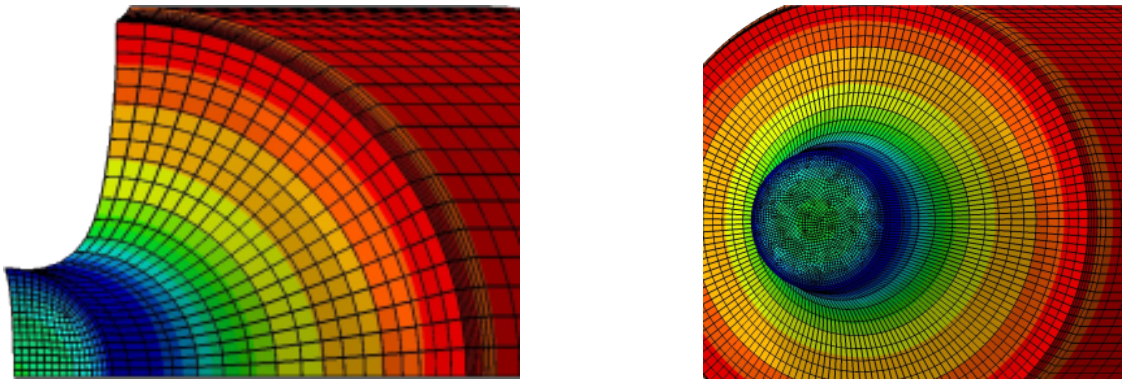

Figure 6.14: Visual comparison of the hydrostatic pressure distribution from an arbitrary cross section of the simplified and full model.

6.4 Sources of Error

When calibrating and validating the models, the focus was on the local behaviour of the simulated specimens, although the global response was important as well. The interaction that was established between the global and local response in Section 5.2.2 and 6.1.1, defined a precedent for the further calibrations and validations. Therefore, only the local behaviour was in focus, since a matching local response gave a matching global response. This was done due to the sheer amount of data, but could be a source of error.

The extracted stress may also be a source for error, due to the possibility of the element not being the element experiencing the highest stress. Moreover, it would probably only lower the stress equally by an arbitrary factor which was assumed negligible.

6.5 Discussion and Conclusion

A common feature of the numerical models was that the response was stiffer for the R2 specimen than for the R20 specimen. The calibrated plastic dilation was too high for several of the material variations that was tested. Although a reasonable reduction of this parameter was performed, the modelled R20 specimens experienced less diameter reduction than the lab results. This was because of the plastic dilation parameter being calibrated with data from the R2 specimens. A perfect match for the R20 specimens could be established with the plastic dilation parameter set close to 1, but since plastic dilation had occurred for all the materials, this assumption was not realistic.

As observed in Section 6.1.1, the boundary conditions had a major impact on the global response of the specimen. After altering the fixtures in the model, the global response matched better, but it should be noted that it had no effect on the local response.

Many of the models corresponded well until the log. longitudinal strain approached a value between 0.7 and 1, when locking behavior was exhibited. This meant that the models worked until the specimen had stretched to between two and three times it's own length. It would be unusual for a material to be elongated to such an extent in reality, and it would surely have been replaced before this occurred. Therefore, SPM could be sufficient in certain industry aspects.

Common tendencies across the material models were when the contraction of the R20 specimens diameter was to small, it corresponded well with the R2 specimen. When the specimen hardened too late for the R20 specimens, the stress hardened correctly for the R2 specimens, or too early. In some cases an increase of the pressure sensitivity parameter softened the response of the R2 specimen and hardened the response of the R20 specimen.

For some of the calibrated models, the baseline often did not harden properly later in the strain history for several of the material models. Moreover, the plastic dilation was seemingly too high for all the baseline models, which also indicated that the mean value of β was too high to be an appropriate choice for the initial calibration.

The simplified model gave results that corresponded adequately with the complete model, and was therefore considered to be suitable to analyze the different variations of the PA11.

7 Conclusion and Further Work

7.1 Conclusion

In this thesis, experimental and numerical studies of PA11 have been carried out to address the thermomechanical behavior at triaxial stress states and the effects of material degradation. PA11 is a semi-crystalline thermoplastic, which is commonly used as liners in flexible risers for transporting oil and gas.

The degradation processes of PA11 have been artificially conducted by three different procedures which aimed for; reducing the amount of plasticizer content (P), reducing the molecular weight (W), and reducing both the amount of plasticizer and the molecular weight (PW) at the same time.

The virgin and degraded material has been examined through tensile tests with and without notches at room temperatures and at -20°C. The replicability was good between similar tests. Additionally, tension tests with higher strain rates and compression tests were conducted. Elastic and plastic material parameters have been analytically identified and optimized through numerical analyses and visual inspection. Furthermore, assumptions regarding strain rate and pressure sensitivity have been studied.

The virgin and degraded specimens showed different mechanical behavior. A reduction of both the plasticizer and the molecular weight (PW) made the specimen stiffer, increased the tensile strength, and decreased the ductility. Moreover, a global softening effect and a loss of the locking behavior were seen from the degraded test results. Furthermore, an increase in volumetric strain and a whitening effect of the fracture surface indicated void growth. Void growth may be the reason for an increased fracture tendency of the degraded specimens.

Under all test conditions, the stress triaxiality had a significant impact on the behavior of PA11. A smaller notch radius increased the damage in the specimen. The amount of volumetric strain increased with a decreasing notch radius and should be considered a damage mechanism due to the indications of void growth. Further, for small notch radiuses, the test specimen behaved more brittle as a component, but locally it still behaved highly ductile.

Almost all the variations experienced some degree of cold drawing. When it did not cold draw, the global ductility dropped greatly. Furthermore, when the temperature was decreased, an

increase in stiffness and strength was observed for all the experiments. Hence, the presence of multiaxial stress states and chemical agents in flexible risers challenge the structural integrity.

Non-linear finite element simulations were done using Abaqus together with the SIMLab Polymer Model. A unique material model has been established for each material variation under both cold and warm conditions, except for the material with reduced molecular weight (W) at -20°C. Common tendencies across the material models were that the response often was either too soft for the specimens with low triaxiality or too stiff for the specimens with high triaxiality. The diameter reduction was too low for the specimens with low triaxiality. The discrepancy in diameter reduction was due to the plastic dilation being independent of the stress state in the material model.

Two significant weaknesses of the SIMLab Polymer Model were observed in this thesis, as has also been seen earlier by Engebretsen (2017). Firstly, the plastic dilation was based on a constant contraction ratio, which was not the case in reality. Secondly, the plastic dilation parameter changes the ratio between the transverse and longitudinal strain unrelated to the stress state of the specimen. These weaknesses make the SPM currently unsuitable for polymers that experience multiaxial stress states or large volume growth.

7.2 Recommended Further work

Material Testing

Further work should be done to complete the in-situ CT-scans, due to the insight it can give with regards to void growth and the materials internal behavior during loading. In-situ CT-scans seems especially relevant for a PA11 specimen with a reduced amount of plasticizer and molecular weight (PW) and a small notch (e.g., R2). These specimens experienced a monotonic increase of volumetric strain until failure.

The degradation process should be more controlled to give further understanding of how the change of each parameter, i.e., reduction of plasticizer content and reduction of molecular weight, affects the response of the material.

Testing of strain-rate sensitivity and pressure sensitivity of the different PA11 variations, above and below the glass transition temperature, should also be done. These tests would give more information regarding the effect of the different types of degradation.

Numerical Simulation

It is possible to optimize the material parameters from the initial calibration with analytical software. For instance, LS-OPT is a graphical optimization tool that interfaces with the finite element software LS-DYNA.

Since there was no possibility of implementing the effect of temperature in the SPM, two material models had to be made for the same material at different temperatures. This was seemingly redundant. Moreover, a material model cannot be established for every possible temperature the material can be exposed to. Temperature is an essential factor for polymers, and a model that does not take it into account is severely weakened. Further work could include implementing a glass transition temperature parameter, due to the drastic differences when the temperature is above and below this point. A temperature dependence has been implemented in numerical models before, although for glassy polymers (Varghese and Batra 2009).

The plastic dilation parameter was not affected by the different stress states of the models, as Engebretsen (2017) also observed. Further, the parameter was assumed constant, which has been proven false in this thesis regarding PA11. A model with the inclusion of porosity may increase the quality of the simulation, e.g., the built-in porous metal plasticity model in Abaqus, which is based on Gurson's yield criterion.

References

4Subsea (2013). *Un-bonded flexible risers – recent field experience and actions for increased robustness*. Tech. rep.

Abaqus Analysis User's Manual (2010). Accessed: 2019-05-13. URL: https://www.sharcnet.ca/Software/Abaqus610/Documentation/docs/v6.10/books/usb/default.htm?startat=pt05ch20s03abm29.html.

Arkema (2011). *RILSAN® Polyamide 11 in Oil & Gas. Off-shore Fluids Compatibility Guide*.

Bartczak, Z. (2017). "Deformation of semicrystalline polymers – the contribution of crystalline and amorphous phases". In: *POLIMERY Journal* 11 - 12, pp. 785–799.

Bartczak, Z. and E. Lezak (2005). "Evolution of lamellar orientation and crystalline texture of various polyethylenes and ethylene-based copolymers in plane-strain compression". In: *Polymer* 46.16, pp. 6050–6063. ISSN: 0032-3861. DOI: https://doi.org/10.1016/j.polymer.2005.04.092. URL: http://www.sciencedirect.com/science/article/pii/S0032386105006981.

Bartczak, Zbigniew et al. (1999). "Toughness mechanism in semi-crystalline polymer blends: II. High-density polyethylene tough end with calcium carbonate filler particles". In: *Polymer* 40, pp. 2347–2365. DOI: 10.1016/S0032-3861(98)00444-3.

Boisot, Guillaume, Christophe Fond, et al. (2008). "Failure of polyamide 11 using a damage finite elements model". In: *ECF 17*, pp. 1554–1561.

Boisot, Guillaume, Lucien Laiarinandrasana, et al. (2011). "Experimental investigations and modeling of volume change induced by void growth in polyamide 11". In: *International Journal of Solids and Structures* 48.19, pp. 2642–2654.

Callister Jr, William D and David G Rethwisch (2012). *Fundamentals of materials science and engineering: an integrated approach*. John Wiley & Sons.

Chiffre, L. De et al. (2014). "Industrial applications of computed tomography". In: *CIRP Annals* 63.2, pp. 655–677. ISSN: 0007-8506. DOI: https://doi.org/10.1016/j.cirp.2014.05.011. URL: http://www.sciencedirect.com/science/article/pii/S0007850614001930.

Engebretsen, Rasmus (2017). "Modelling of PA in inner liner in flexible pipes". In:

Fagerholt, E, T Børvik, and OS Hopperstad (2013). "Measuring discontinuous displacement fields in cracked specimens using digital image correlation with mesh adaptation and crack-path optimization". In: *Optics and Lasers in Engineering* 51.3, pp. 299–310.

Galeski, A. et al. (1992). "Morphological alterations during texture-producing plastic plane strain compression of high-density polyethylene". In: *Macromolecules* 25.21, pp. 5705–5718. DOI: 10.1021/ma00047a023. eprint: https://doi.org/10.1021/ma00047a023. URL: https://doi.org/10.1021/ma00047a023.

Gargallo, Ligia and Deodato Radic (2009). *Physicochemical behavior and supramolecular organization of polymers*. Springer Science & Business Media.

Ghorbel, Elhem (2008). "A viscoplastic constitutive model for polymeric materials". In: *International Journal of Plasticity* 24.11, pp. 2032–2058. URL: http://www.sciencedirect.com/science/article/pii/S0749641908000119.

Hopperstad, Odd Sture and Tore Børvik (2017). *Lecture Notes, TKT4135 Mechanics of materials*.

Lewis, Peter Rhys (2016). "Chapter 2 - Sample Examination and Analysis". In: *Forensic Polymer Engineering (Second Edition)*. Ed. by Peter Rhys Lewis. Second Edition. Woodhead Publishing in Materials. Woodhead Publishing, pp. 33–69. ISBN: 978-0-08-101055-6. DOI: https://doi.org/10.1016/B978-0-08-101055-6.00002-1. URL: http://www.sciencedirect.com/science/article/pii/B9780081010556000021.

McCormick, Nick and Jerry Lord (2010). "Digital image correlation". In: *Materials today* 13.12, pp. 52–54.

Nishida, Masahiro, Rie Natsume, and Masayuki Hayashi (2014). "Strain Rate Dependence of Yield Condition of Polyamide 11". In: *Dynamic Behavior of Materials, Volume 1*. Ed. by Bo Song, Dan Casem, and Jamie Kimberley. Cham: Springer International Publishing, pp. 121–127. ISBN: 978-3-319-00771-7.

Ognedal, Anne Serine et al. (2014). "Void nucleation and growth in mineral-filled PVC – An experimental and numerical study". In: *International Journal of Solids and Structures* 51.7, pp. 1494–1506. ISSN: 0020-7683. DOI: https://doi.org/10.1016/j.ijsolstr.2013.12.042. URL: http://www.sciencedirect.com/science/article/pii/S0020768314000092.

Polanco-Loria, Mario et al. (2010). "Constitutive model for thermoplastics with structural applications". In: *International Journal of Impact Engineering* 37.12, pp. 1207–1219. ISSN: 0734-743X. DOI: https://doi.org/10.1016/j.ijimpeng.2010.06.006. URL: http://www.sciencedirect.com/science/article/pii/S0734743X10001065.

Raghava, Ram Singh (1972). "Macroscopic yielding behavior of polymeric materials". In:

Robson, Jack (2018). *Crystallinity and Filaments*. Accessed: 2019-05-13. URL: https://www.filaments.directory/en/blog/2018/08/01/crystallinity-and-filaments.

Rösler, Joachim, Martin Bäker, and Harald Harders (2007). "Mechanical behaviour of polymers". In: *Mechanical Behaviour of Engineering Materials*. Springer, pp. 257–293.

Schirrer, R., C. Fond, and A. Lobbrecht (1996). "Volume change and light scattering during mechanical damage in polymethylmethacrylate toughened with core-shell rubber particles". In: *Journal of Materials Science* 31.24, pp. 6409–6422. ISSN: 1573-4803. DOI: 10.1007/BF00356243. URL: https://doi.org/10.1007/BF00356243.

SIMLab (2015). *SIMLab Polymer Model (SPM) - Theory, user's and example manual*.

Varghese, A.G. and R.C. Batra (2009). "Constitutive equations for thermomechanical deformations of glassy polymers". In: *International Journal of Solids and Structures* 46.22, pp. 4079–4094. ISSN: 0020-7683. DOI: https://doi.org/10.1016/j.ijsolstr.2009.08.006. URL: http://www.sciencedirect.com/science/article/pii/S0020768309003035.

Ward, I.M (2004). *An introduction to the mechanical properties of solid polymers*. eng. Chichester.

Wright, D. C. and Limited Rapra Technology (2006). *Failure of Plastics and Rubber Products : Causes, Effects and Case Studies Involving Degradation*. Vol. [Rev. ed.] Rapra Technology Ltd. ISBN: 9781859575178. URL: http://search.ebscohost.com/login.aspx?direct=true&db=e230xww&AN=234954&site=ehost-live.

A Appendix

In this appendix, the conducted material tests are presented in depth. Every test has its own page with information regarding test conditions, calibrated parameters, plots from the tests, and an image from the DIC analysis.

The curves presented are:

- Force vs. displacement
- True stress vs. log. longitudinal strain
- Strain rate vs. log. longitudinal strain
- Log. volumetric strain vs. log. longitudinal strain
- Log. transverse strain vs. log. longitudinal strain

Results: 1 V-S-H

Table A.1: Test information for specimen 1: V-S-H

Test no.	Material	Load	Nominal strain-rate	Notch radius	Temp.
1	V	Tension	10^{-3} s^{-1}	-	20 °C

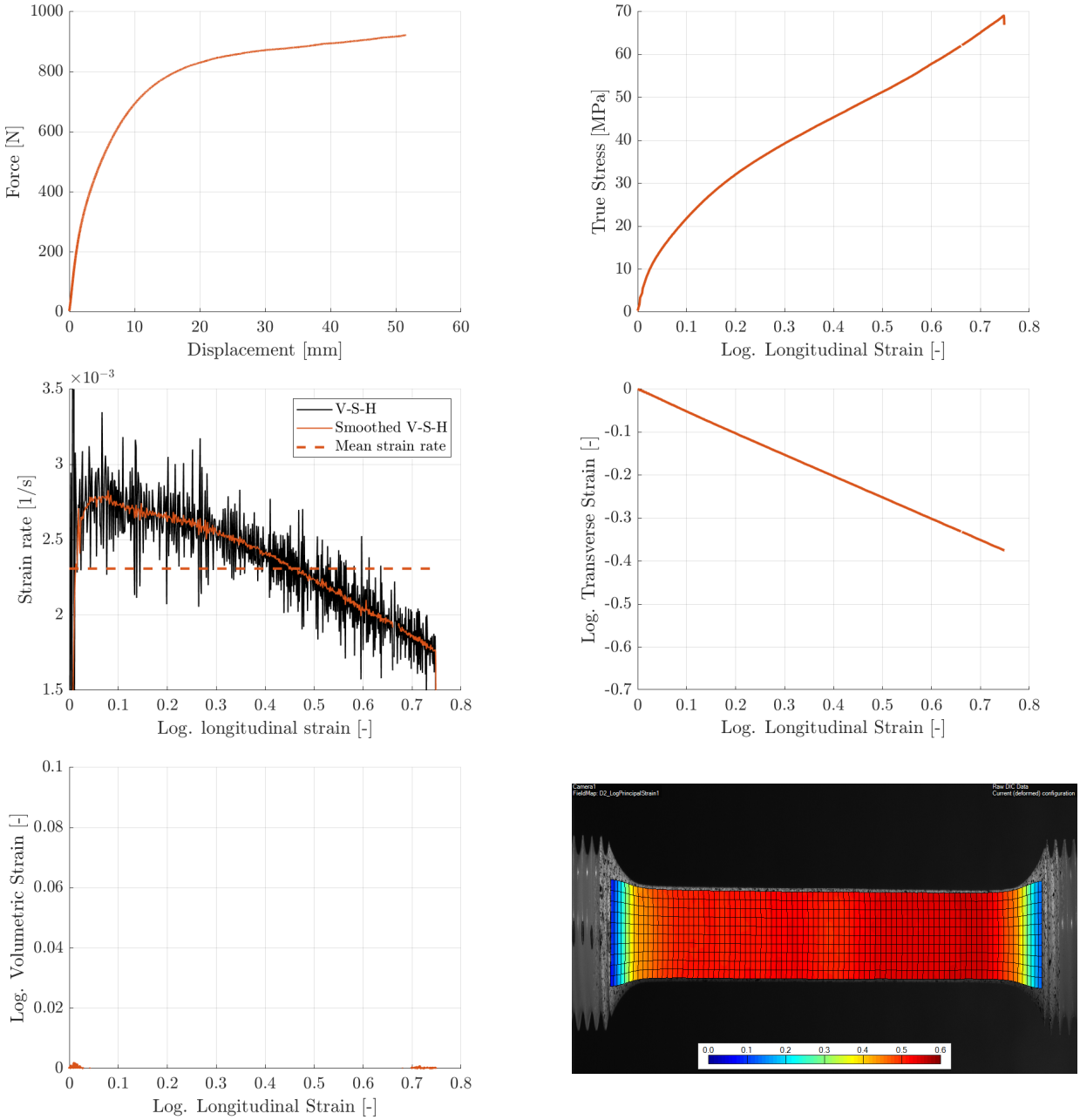

Figure A.1: Test results for specimen 1: V-S-H

Table A.2: Material properties for specimen 1: V-S-H

E	ν	σ_y	ε_y
472.9 MPa	0.5	9.2 MPa	0.022

Results: 2 V-S-H

Table A.3: Test information for specimen 2: V-S-H

Test no.	Material	Load	Nominal strain-rate	Notch radius	Temp.
2	V	Tension	10^{-3} s^{-1}	-	20 °C

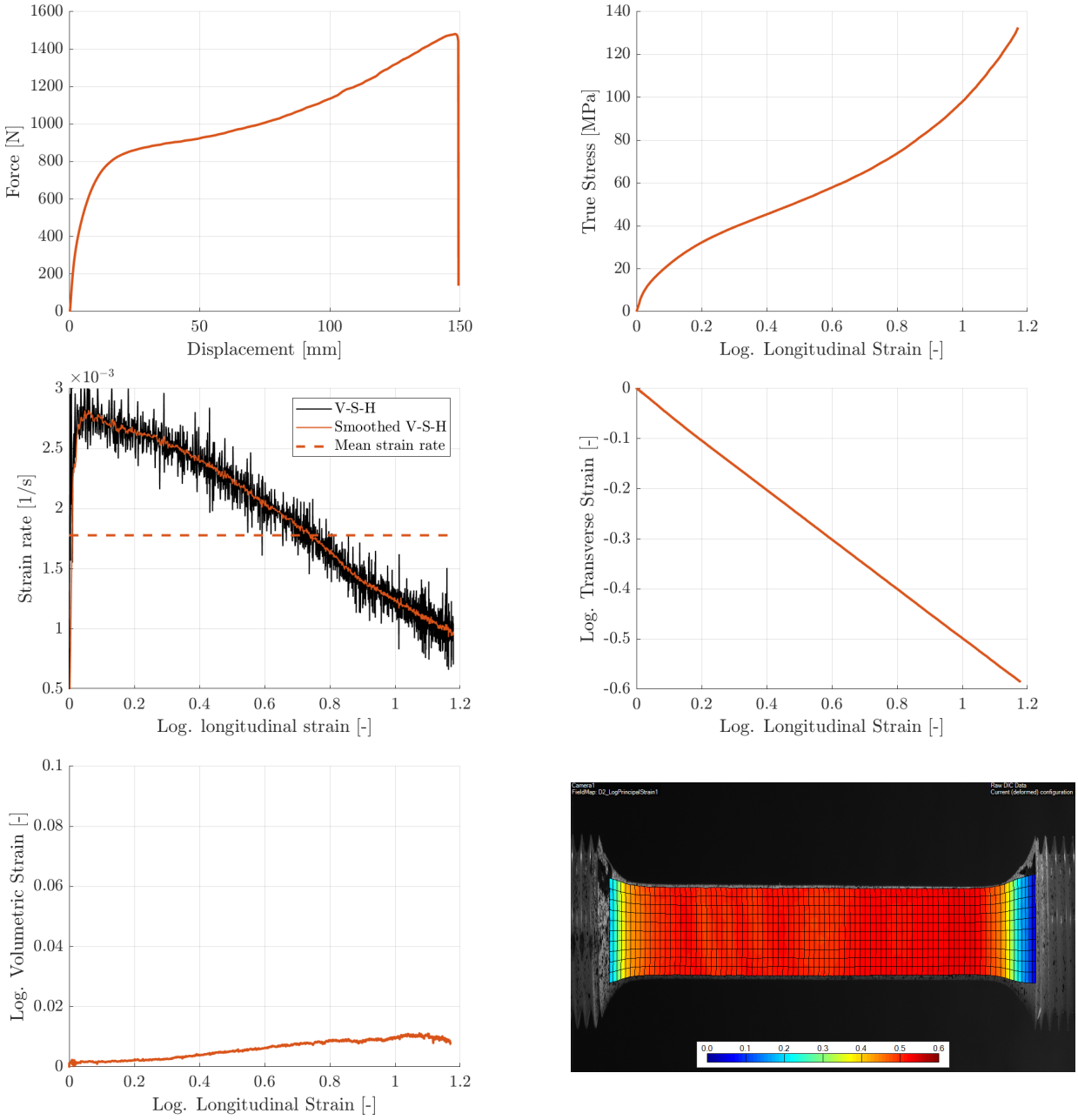

Figure A.2: Test results for specimen 2: V-S-H

Table A.4: Material properties for specimen 2: V-S-H

E	ν	σ_y	ε_y
490.1 MPa	0.5	9.2 MPa	0.022

Results: 3 V-R20-H

Table A.5: Test information for specimen 3: V-R20-H

Test no.	Material	Load	Nominal strain-rate	Notch radius	Temp.
3	V	Tension	10^{-3} s^{-1}	20 mm	20 °C

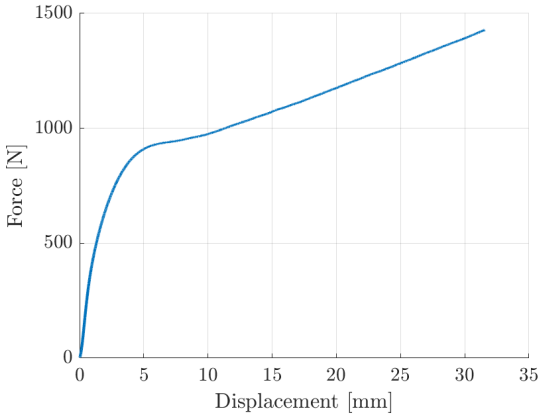

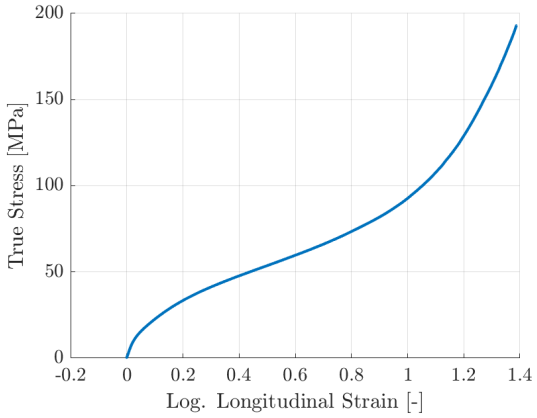

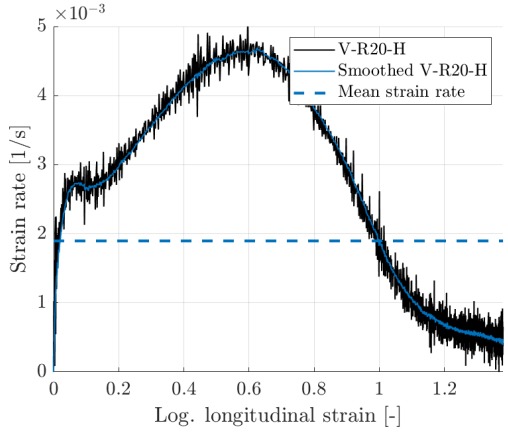

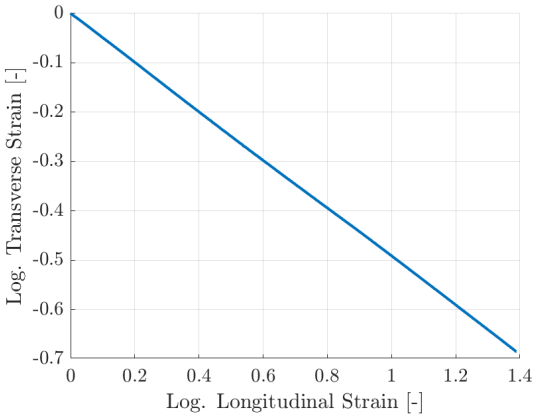

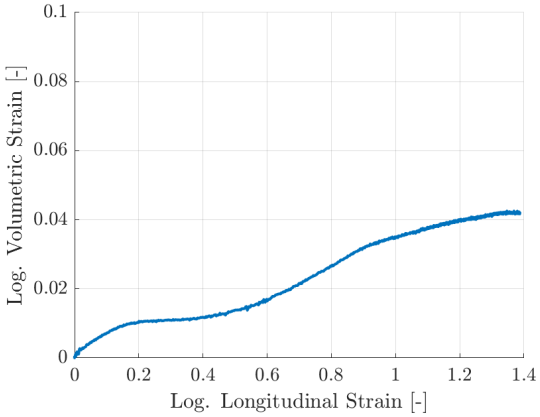

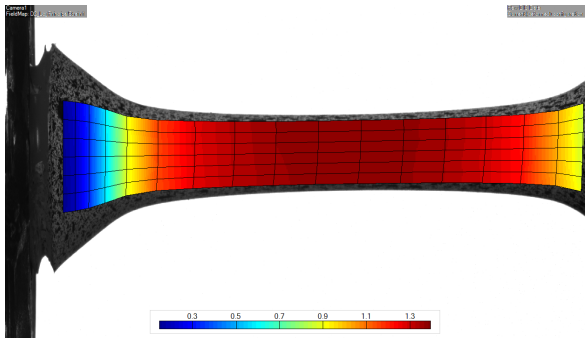

Figure A.3: Test results for specimen 3: V-R20-H

Table A.6: Material properties for specimen 3: V-R20-H

E	ν	σ_y	ε_y
443.3 MPa	0.46	10.5 MPa	0.026

Results: 4 V-R5-H

Table A.7: Test information for specimen 4: V-R5-H

Test no.	Material	Load	Nominal strain-rate	Notch radius	Temp.
4	V	Tension	10^{-3} s^{-1}	5 mm	20 °C

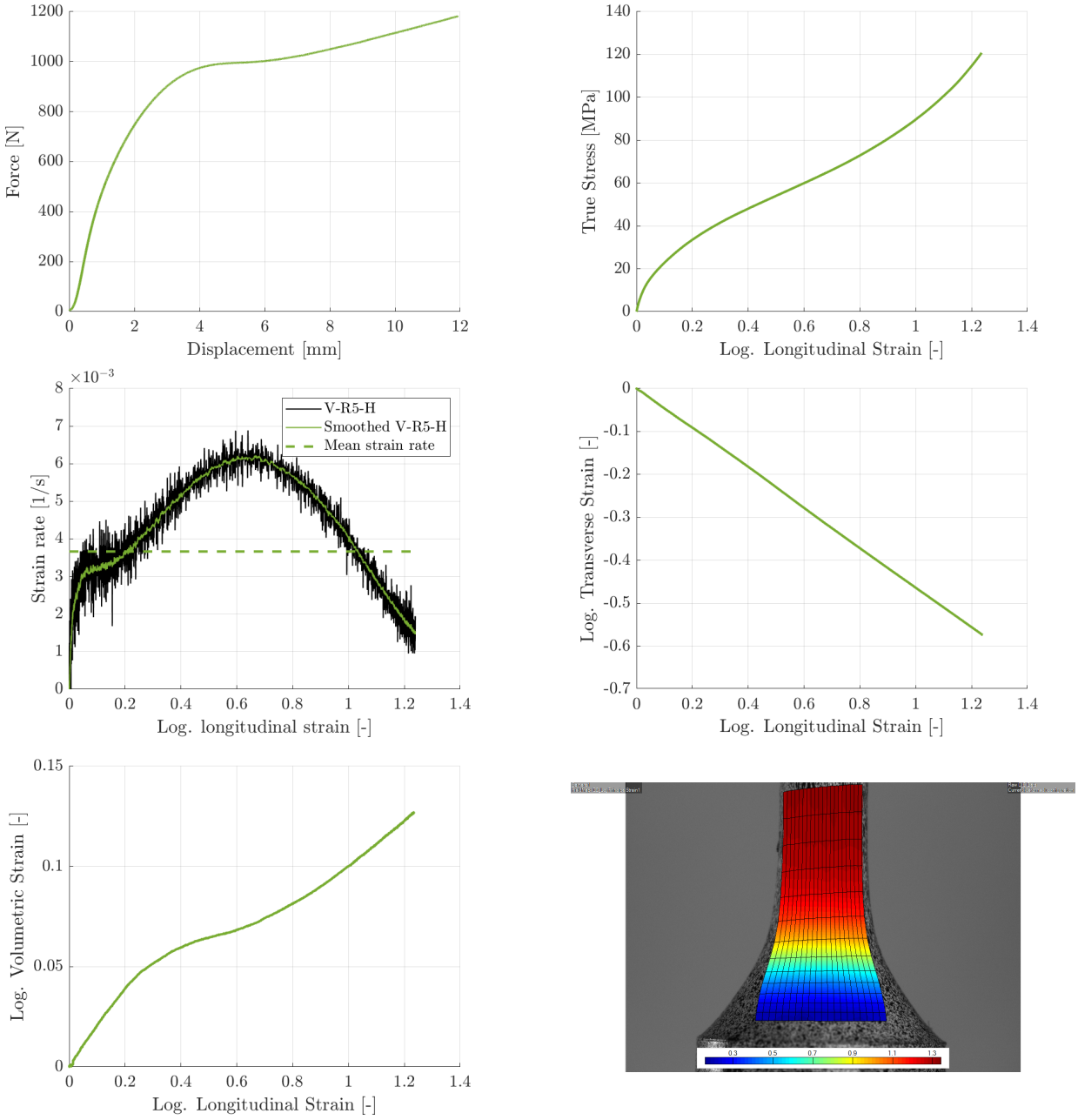

Figure A.4: Test results for specimen 4: V-R5-H

Table A.8: Material properties for specimen 4: V-R5-H

E	ν	σ_y	ε_y
511.0 MPa	0.46	8.5 MPa	0.020

Results: 5 V-R2-H

Table A.9: Test information for specimen 5: V-R2-H

Test no.	Material	Load	Nominal strain-rate	Notch radius	Temp.
5	V	Tension	10^{-3} s^{-1}	2 mm	20 °C

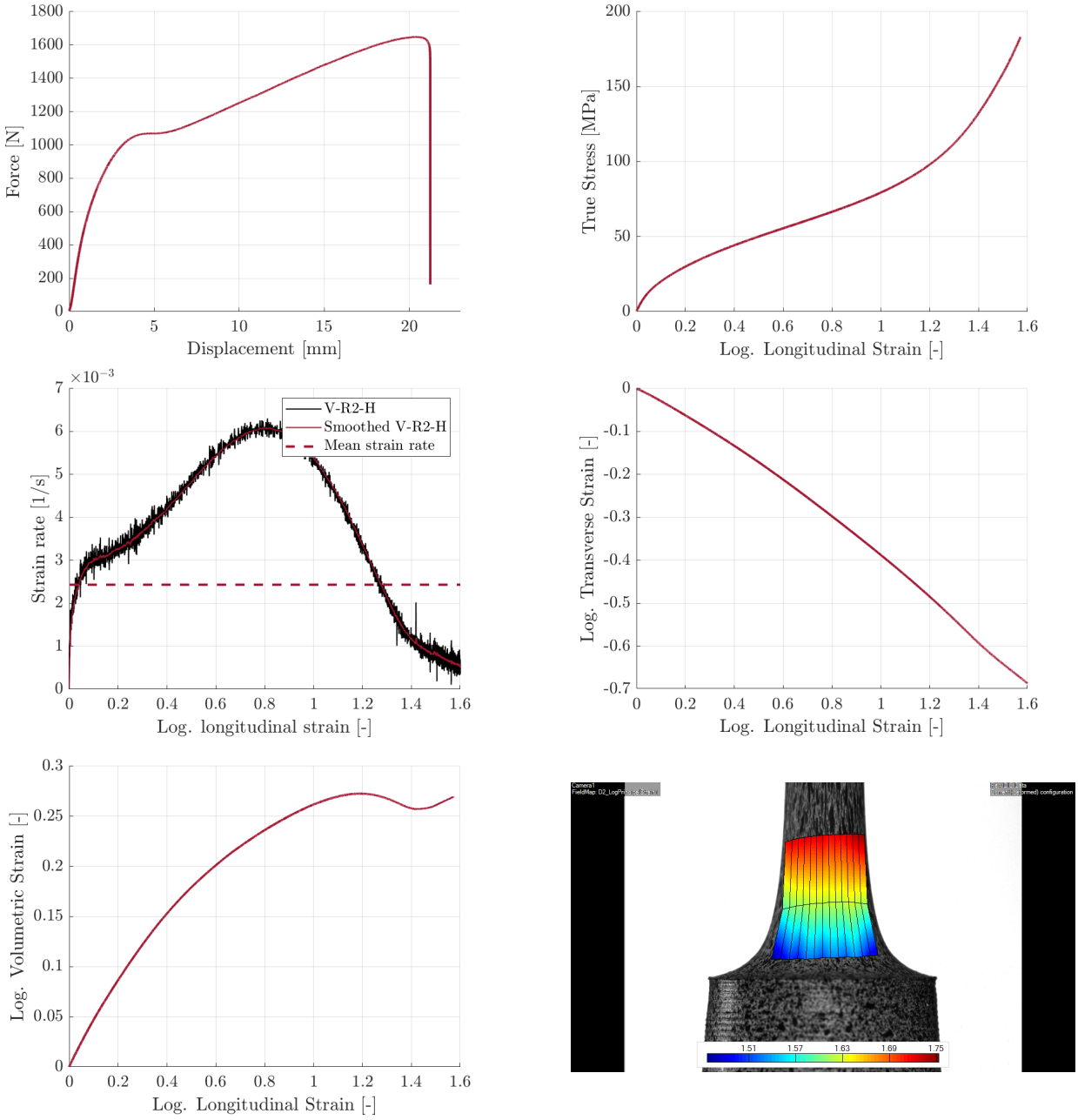

Figure A.5: Test results for specimen 5: V-R2-H

Table A.10: Material properties for specimen 5: V-R2-H

E	ν	σ_y	ε_y
301.6 MPa	0.25	10.4 MPa	0.036

Results: 6 V-R2-H

Table A.11: Test information for specimen 6: V-R2-H

Test no.	Material	Load	Nominal strain-rate	Notch radius	Temp.
6	V	Tension	10^{-3} s^{-1}	2 mm	20 °C

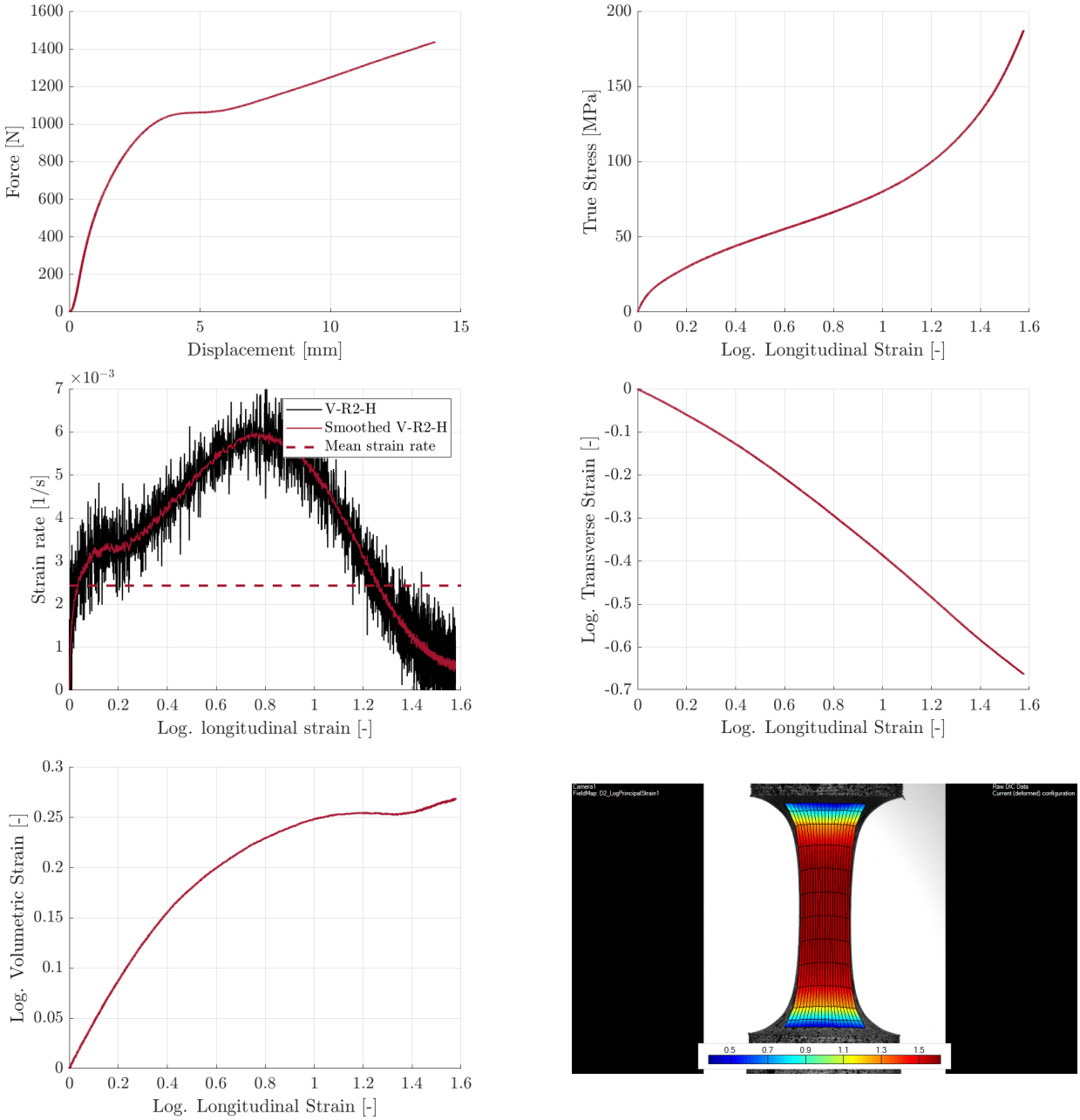

Figure A.6: Test results for specimen 6: V-R2-H

Table A.12: Material properties for specimen 6: V-R2-H

E	ν	σ_y	ε_y
344.8 MPa	0.25	9.1 MPa	0.029

Results: 7 V-R20-C

Table A.13: Test information for specimen 7: V-R20-C

Test no.	Material	Load	Nominal strain-rate	Notch radius	Temp.
7	V	Tension	10^{-3} s^{-1}	20 mm	-20 °C

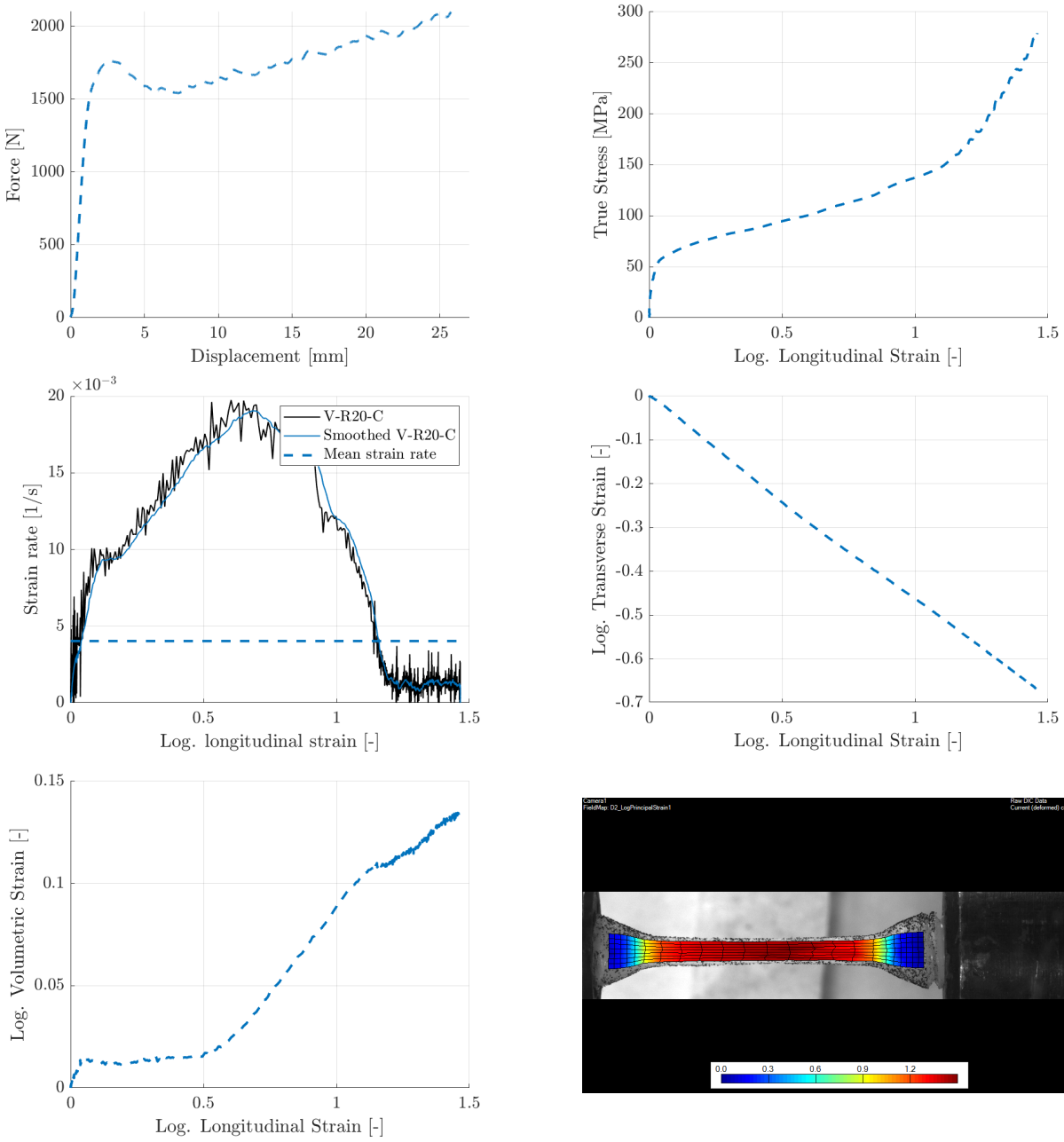

Figure A.7: Test results for specimen 7: V-R20-C

Table A.14: Material properties for specimen 7: V-R20-C

E	ν	σ_y	ε_y
1210.0 MPa	0.35	40 MPa	0.036

Results: 8 V-R20-C

Table A.15: Test information for specimen 8: V-R20-C

Test no.	Material	Load	Nominal strain-rate	Notch radius	Temp.
8	V	Tension	10^{-3} s^{-1}	20 mm	-20 °C

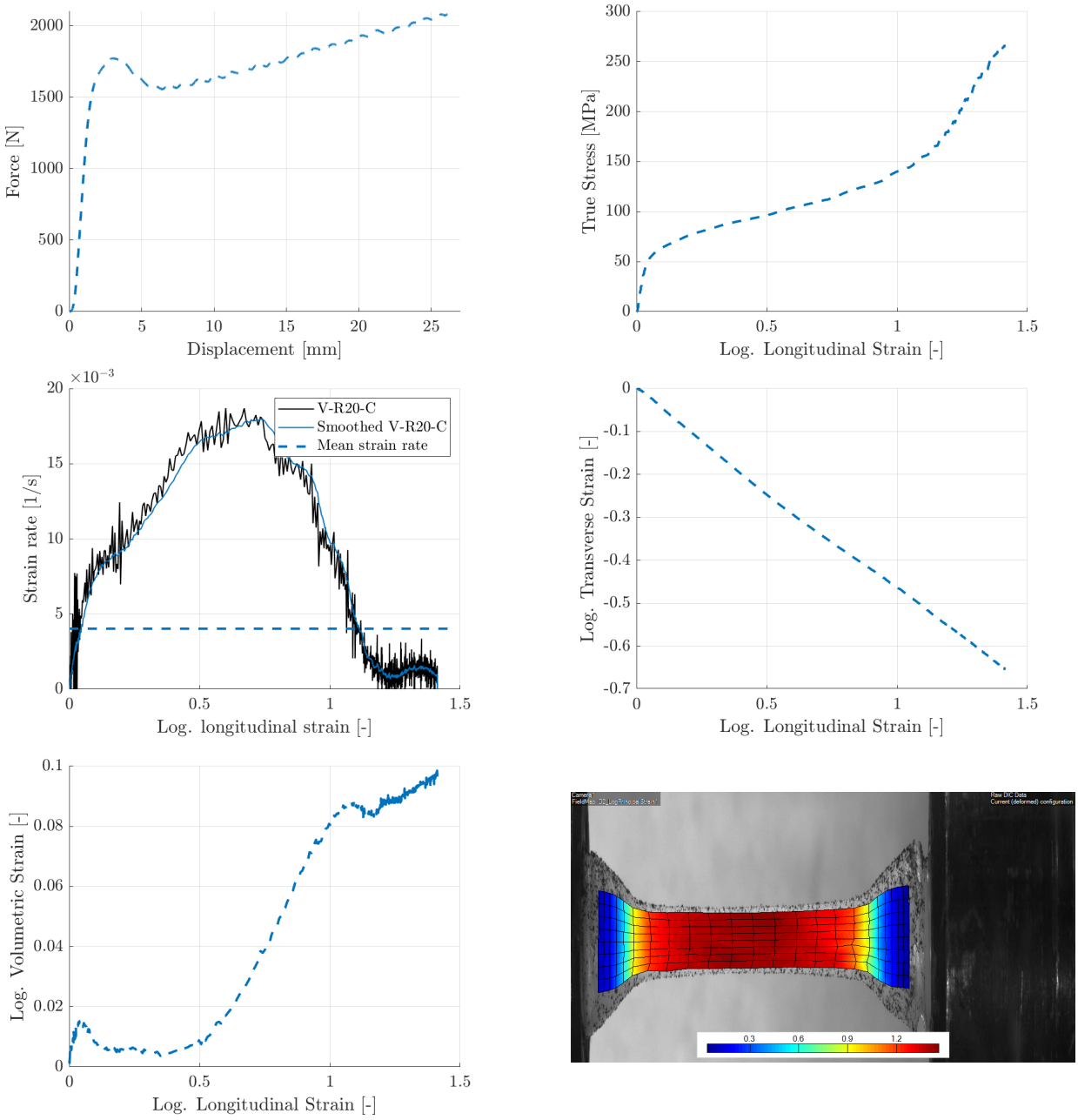

Figure A.8: Test results for specimen 8: V-R20-C

Table A.16: Material properties for specimen 8: V-R20-C

E	ν	σ_y	ε_y
1206.0 MPa	0.36	36 MPa	0.037

Results: 9 V-R2-C

Table A.17: Test information for specimen 9: V-R2-C

Test no.	Material	Load	Nominal strain-rate	Notch radius	Temp.
9	V	Tension	10^{-3} s^{-1}	2 mm	-20 °C

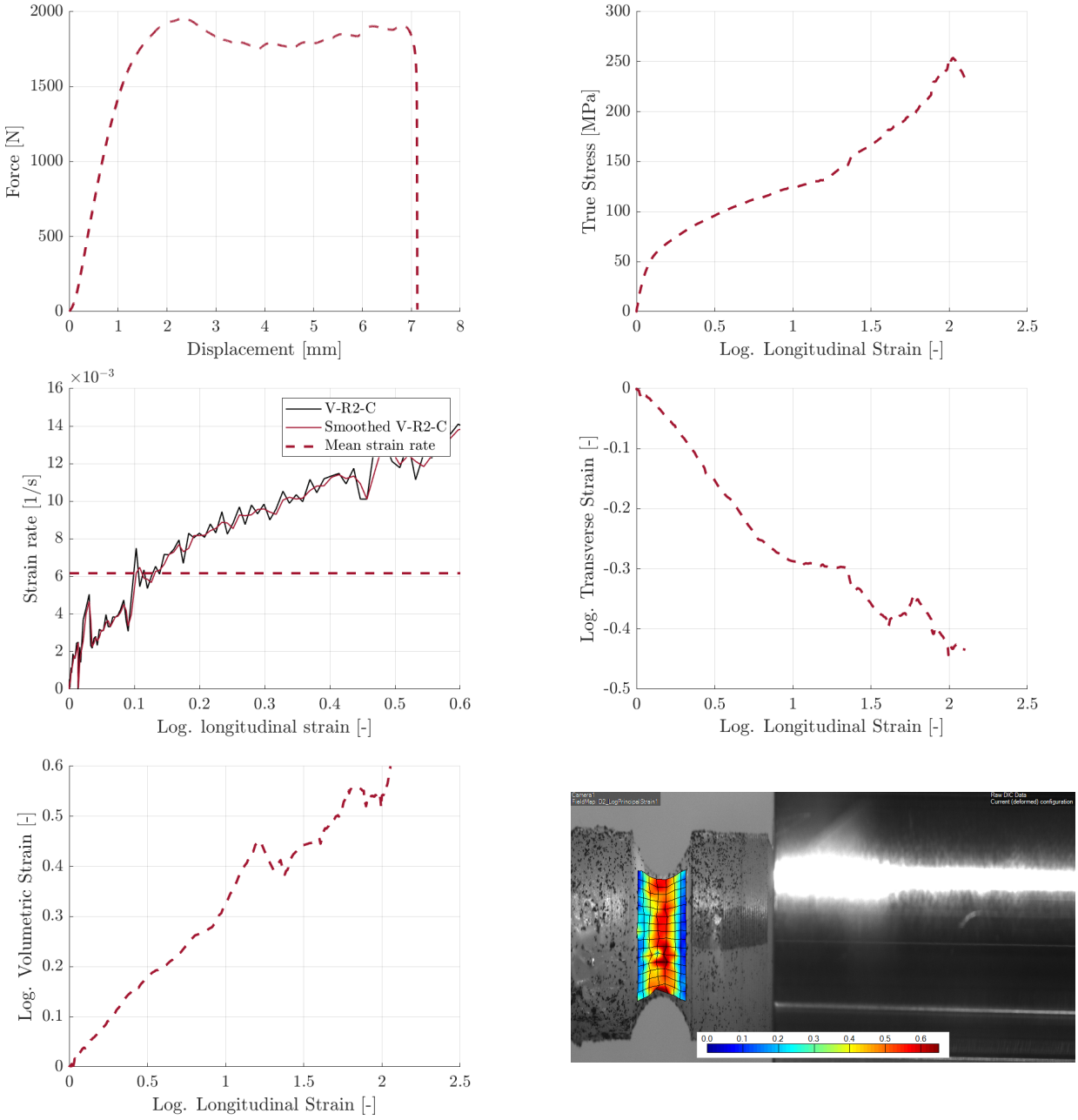

Figure A.9: Test results for specimen 9: V-R2-C

Table A.18: Material properties for specimen 9: V-R2-C

E	ν	σ_y	ε_y
982.3 MPa	0.2	20 MPa	0.024

Results: 10 V-S-H-Ra2

Table A.19: Test information for specimen 10: V-S-H-Ra2

Test no.	Material	Load	Nominal strain-rate	Notch radius	Temp.
10	V	Tension	10^{-2} s^{-1}	-	20 °C

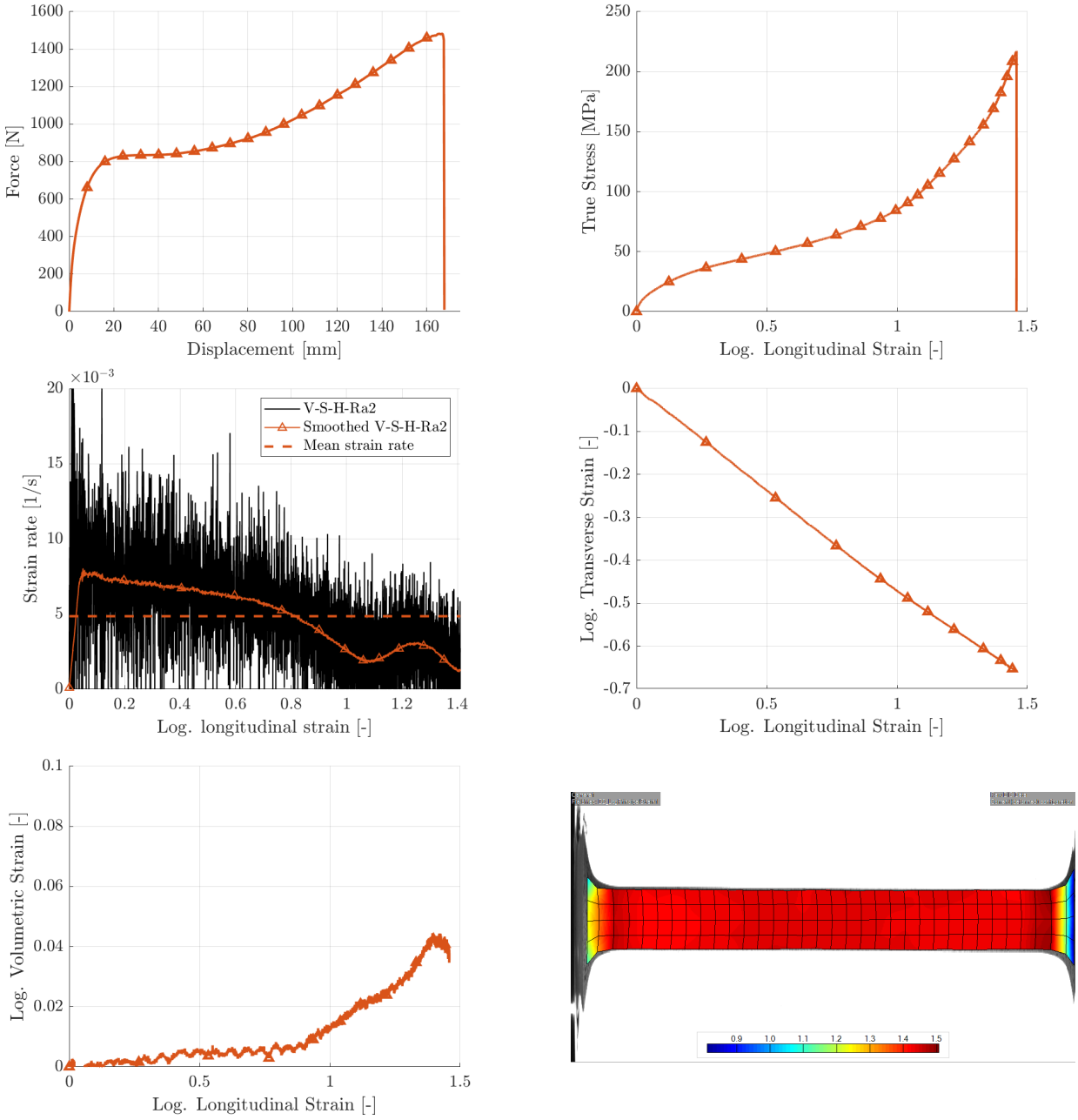

Figure A.10: Test results for specimen 10: V-S-H-Ra2

Table A.20: Material properties for specimen 10: V-S-H-Ra2

E	ν	σ_y	ε_y
557.6 MPa	0.43	8.5 MPa	0.019

Results: 11 V-S-H-Ra3

Table A.21: Test information for specimen 11: V-S-H-Ra3

Test no.	Material	Load	Nominal strain-rate	Notch radius	Temp.
11	V	Tension	10^{-1} s^{-1}	-	20 °C

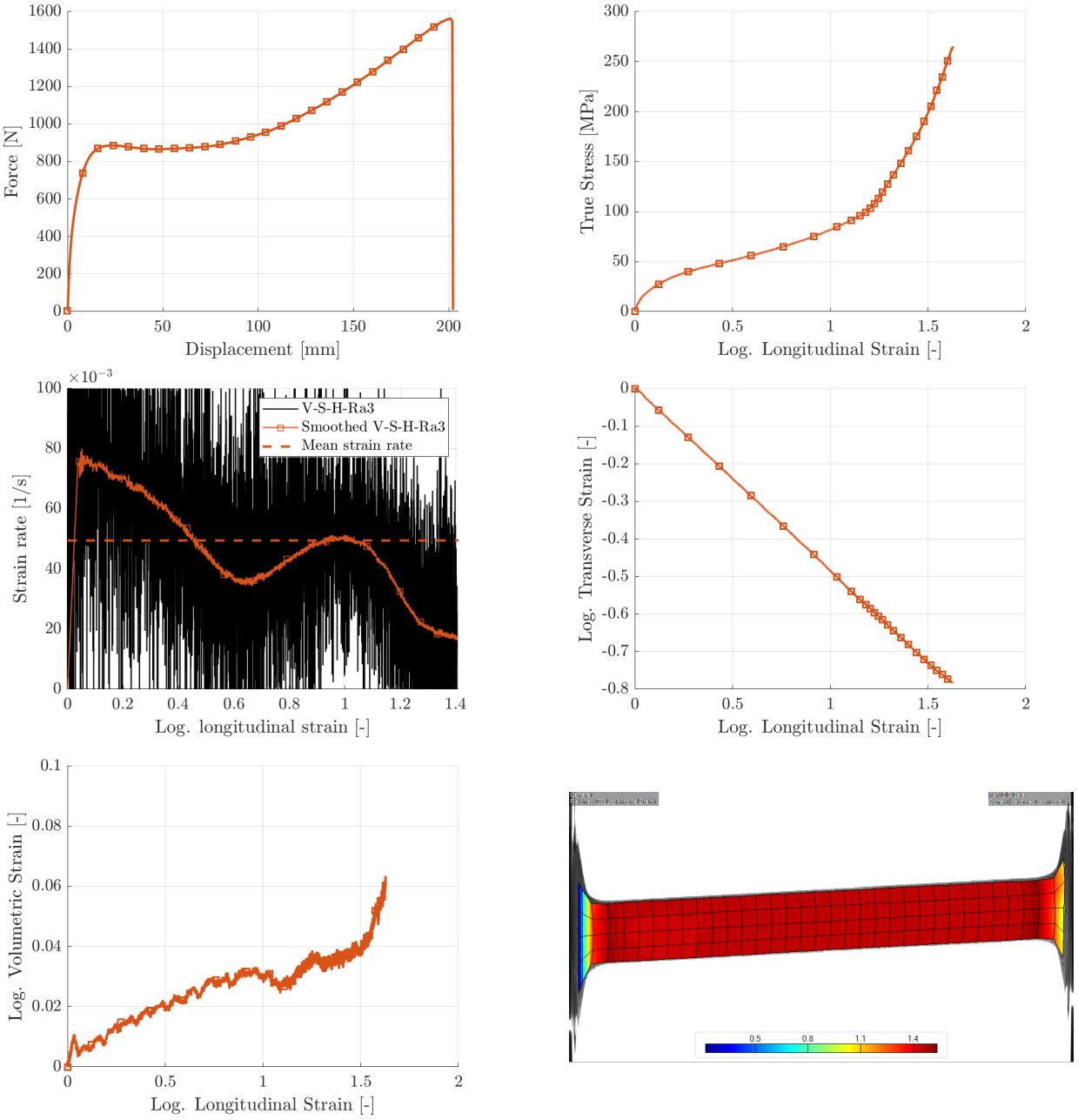

Figure A.11: Test results for specimen 11: V-S-H-Ra3

Table A.22: Material properties for specimen 11: V-S-H-Ra3

E	ν	σ_y	ε_y
437.6 MPa	0.35	14 MPa	0.033

Results: 12 V-R5-H-Ra2

Table A.23: Test information for specimen 12: V-R5-H-Ra2

Test no.	Material	Load	Nominal strain-rate	Notch radius	Temp.
12	V	Tension	10^{-2} s^{-1}	5 mm	20 °C

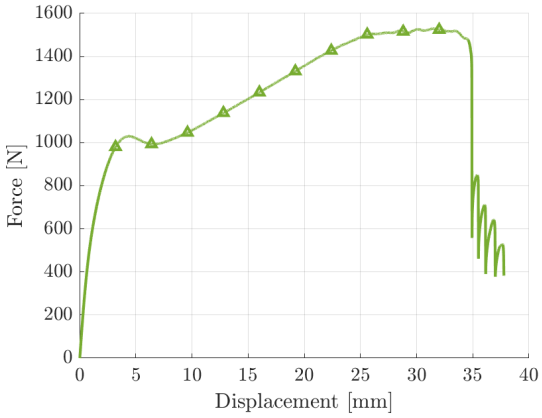

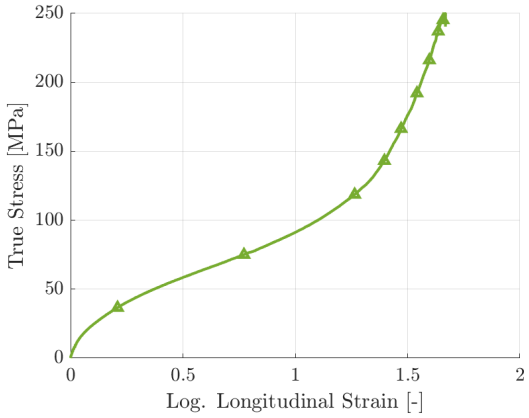

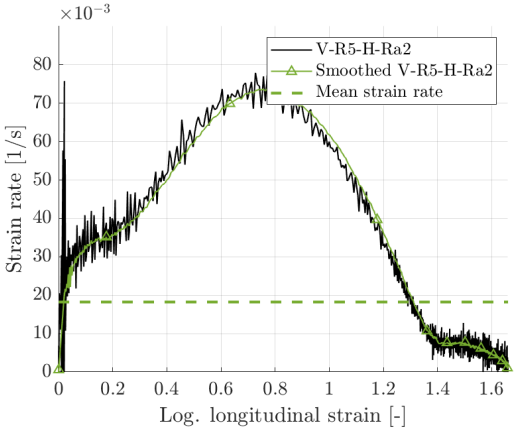

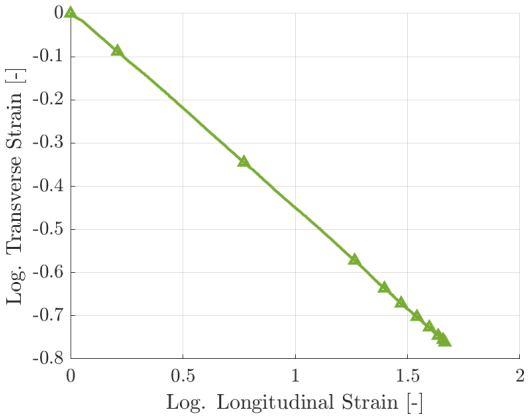

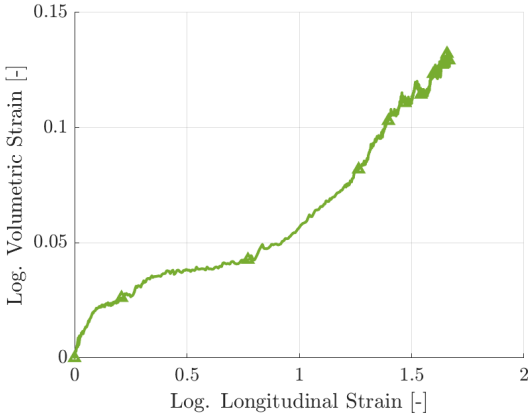

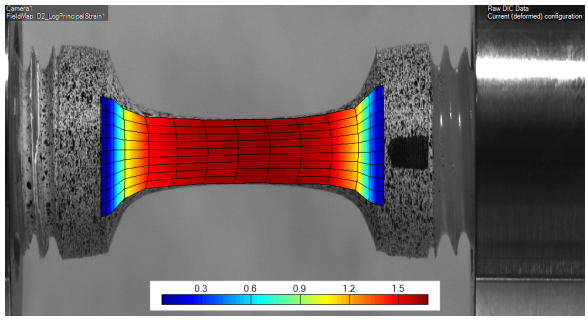

Figure A.12: Test results for specimen 12: V-R5-H-Ra2

Table A.24: Material properties for specimen 12: V-R5-H-Ra2

E	ν	σ_y	ε_y
412.4 MPa	0.37	11.3 MPa	0.028

Results: 13 V-R5-H-Ra3

Table A.25: Test information for specimen 13: V-R5-H-Ra3

Test no.	Material	Load	Nominal strain-rate	Notch radius	Temp.
13	V	Tension	10^{-1} s^{-1}	5 mm	20 °C

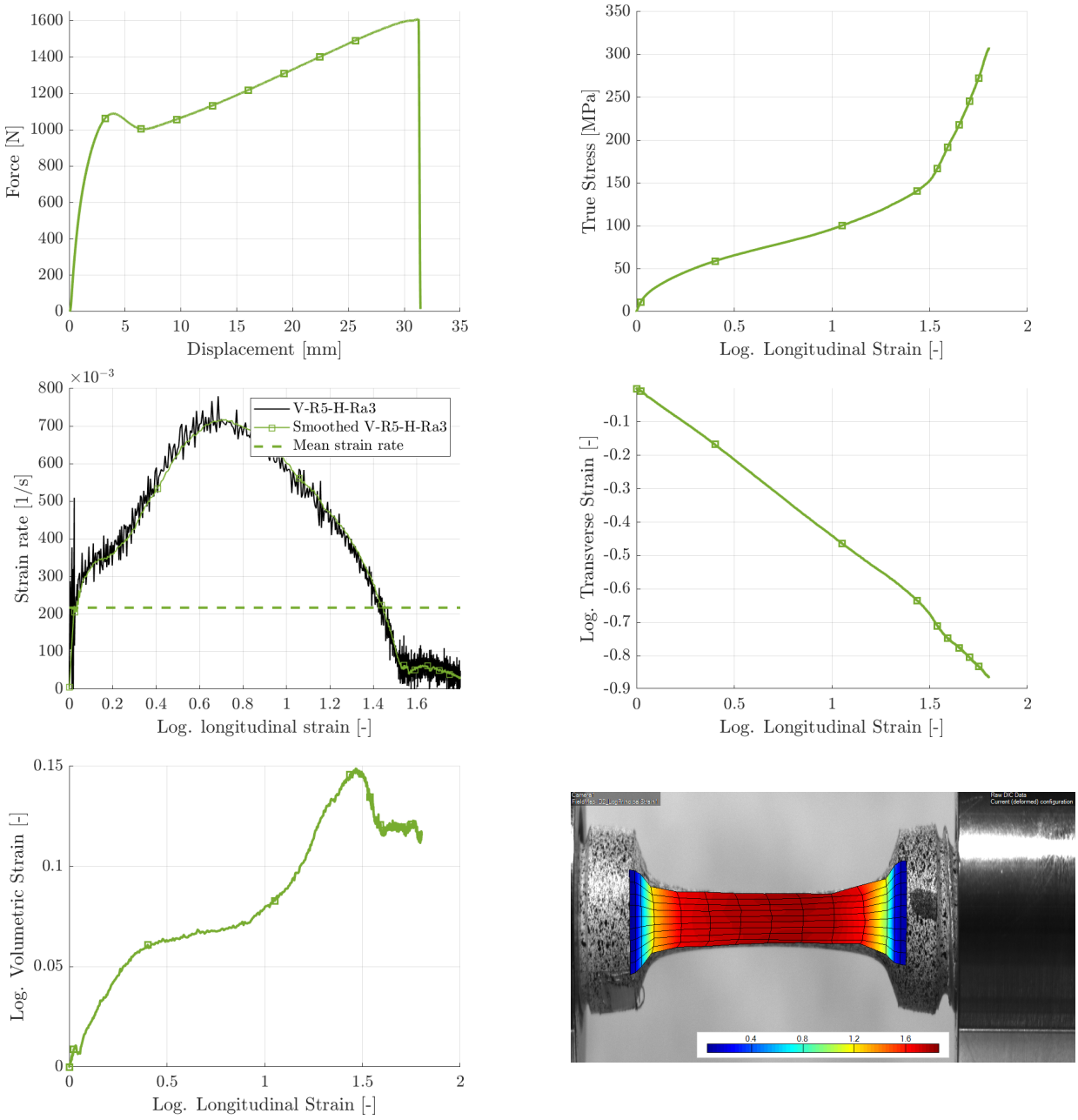

Figure A.13: Test results for specimen 13: V-R5-H-Ra3

Table A.26: Material properties for specimen 13: V-R5-H-Ra3

E	ν	σ_y	ε_y
474.0 MPa	0.37	15.4 MPa	0.034

Results: 14 P-R20-H

Table A.27: Test information for specimen 14: P-R20-H

Test no.	Material	Load	Nominal strain-rate	Notch radius	Temp.
14	P	Tension	10^{-3} s^{-1}	20 mm	20 °C

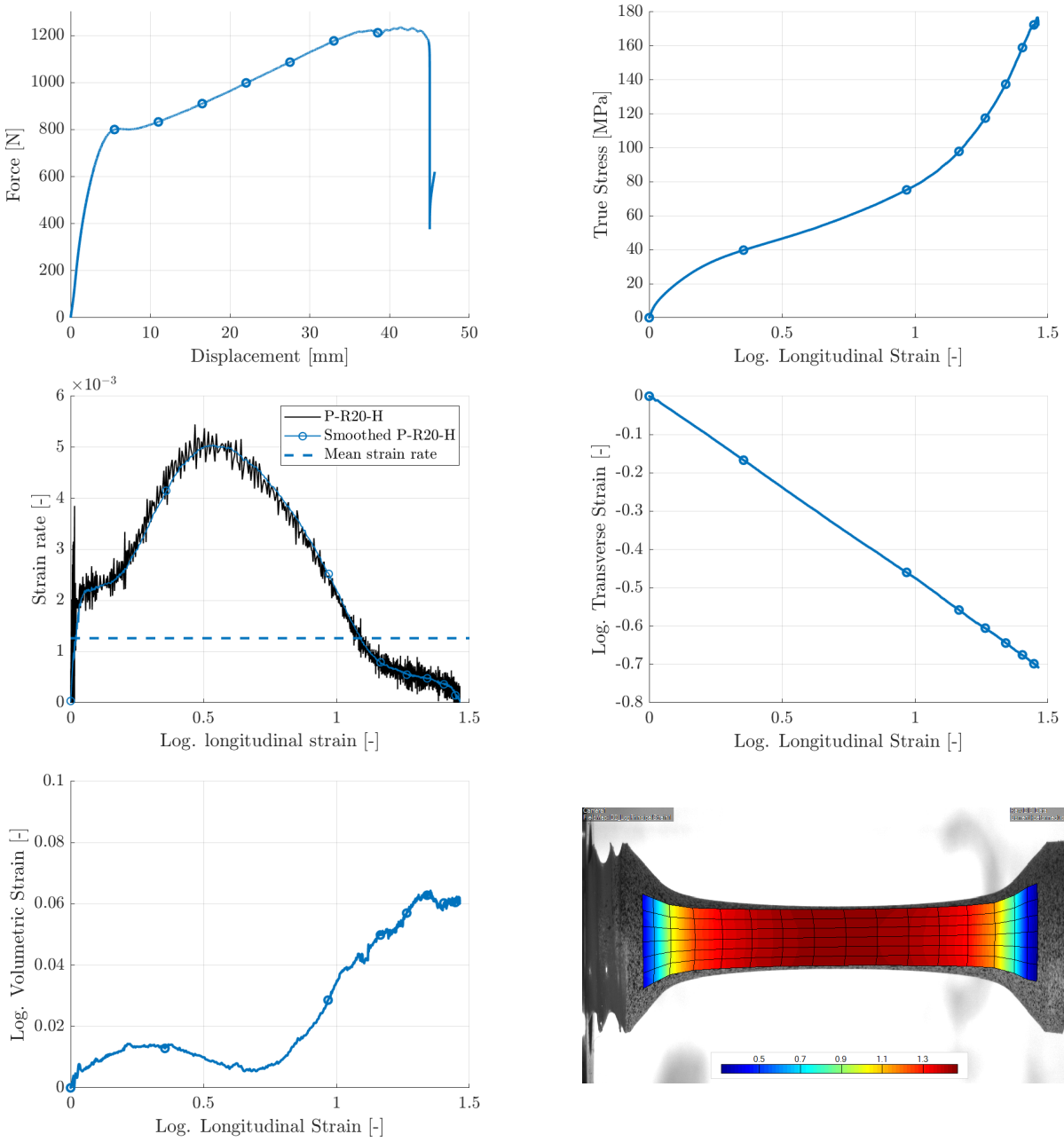

Figure A.14: Test results for specimen 14: P-R20-H

Table A.28: Material properties for specimen 14: P-R20-H

E	ν	σ_y	ε_y
337.3 MPa	0.4	9 MPa	0.029

Results: 15 PW-R20-H

Table A.29: Test information for specimen 15: PW-R20-H

Test no.	Material	Load	Nominal strain-rate	Notch radius	Temp.
15	PW	Tension	10^{-3} s^{-1}	20 mm	20 °C

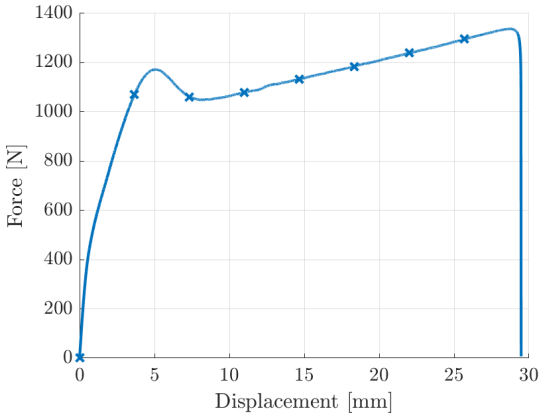

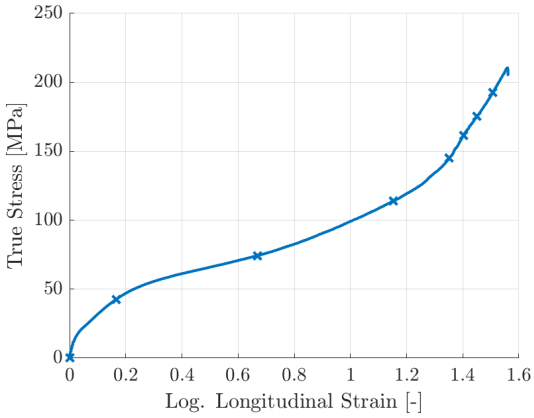

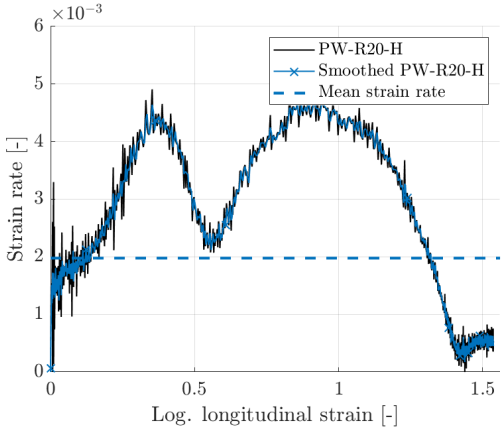

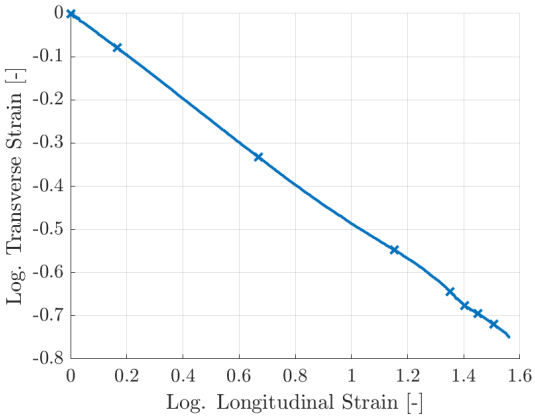

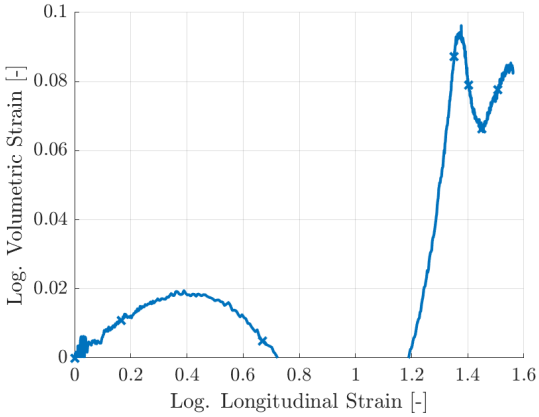

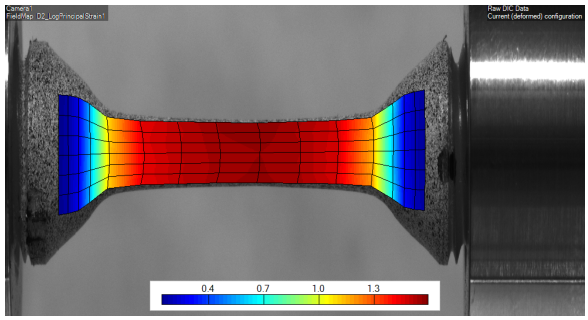

Figure A.15: Test results for specimen 15: PW-R20-H

Table A.30: Material properties for specimen 15: PW-R20-H

E	ν	σ_y	ε_y
865.7 MPa	0.4	13.7 MPa	0.019

Results: 16 W-R20-H

Table A.31: Test information for specimen 16: W-R20-H

Test no.	Material	Load	Nominal strain-rate	Notch radius	Temp.
16	W	Tension	10^{-3} s^{-1}	20 mm	20 °C

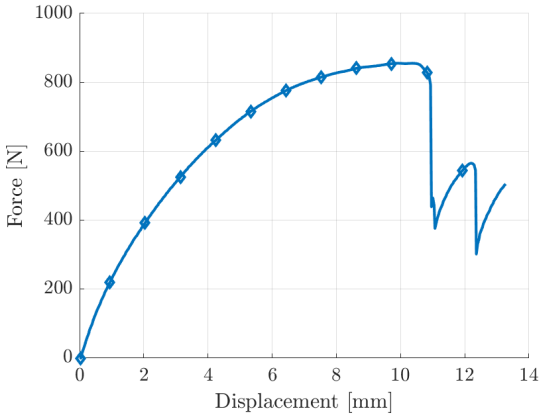

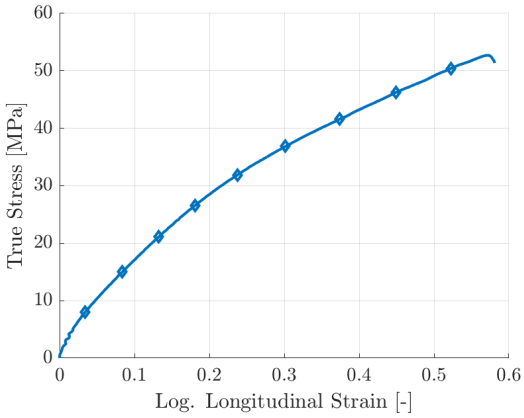

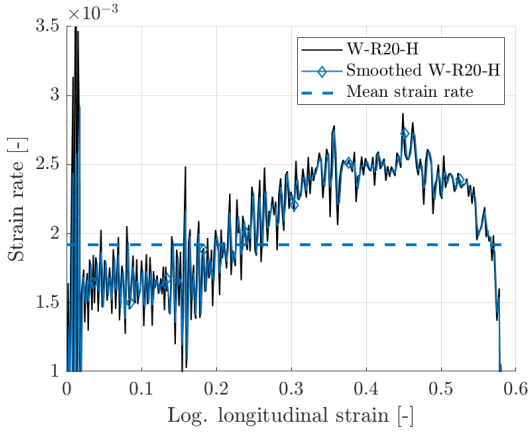

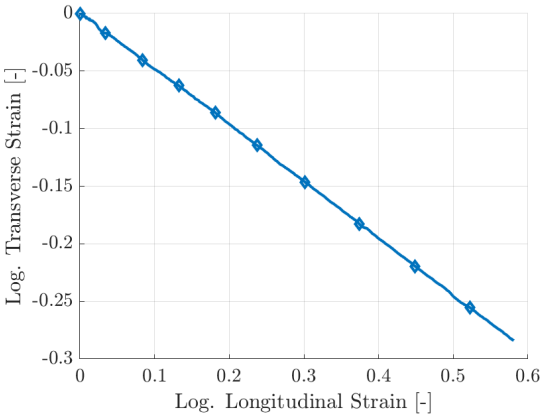

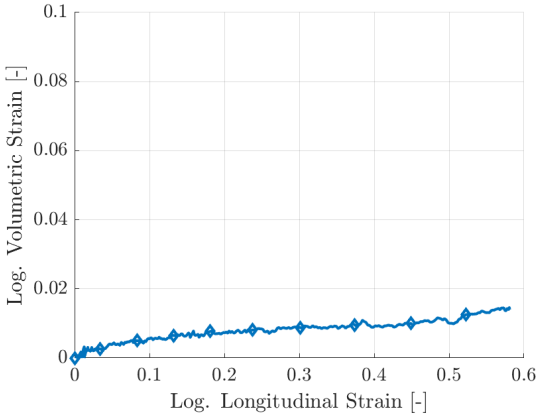

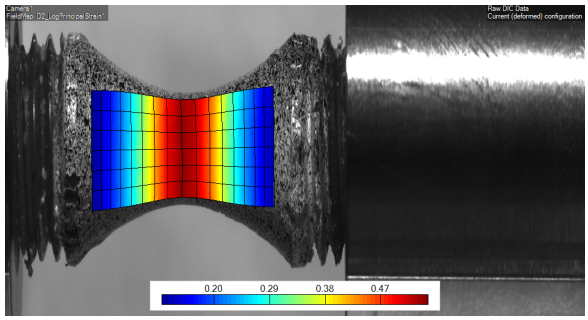

Figure A.16: Test results for specimen 16: W-R20-H

Table A.32: Material properties for specimen 16: W-R20-H

E	ν	σ_y	ε_y
288.4 MPa	0.45	6.6 MPa	0.026

Results: 17 P-R20-C

Table A.33: Test information for specimen 17: P-R20-C

Test no.	Material	Load	Nominal strain-rate	Notch radius	Temp.
17	P	Tension	10^{-3} s^{-1}	20 mm	-20 °C

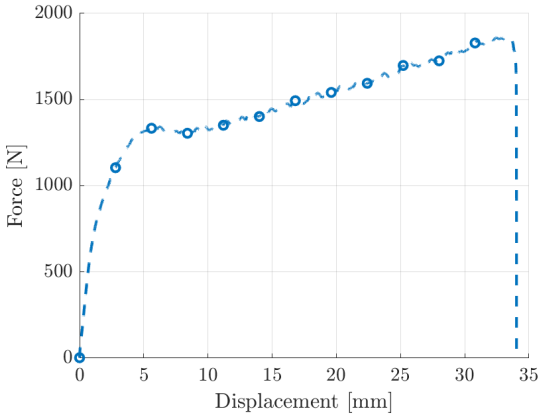

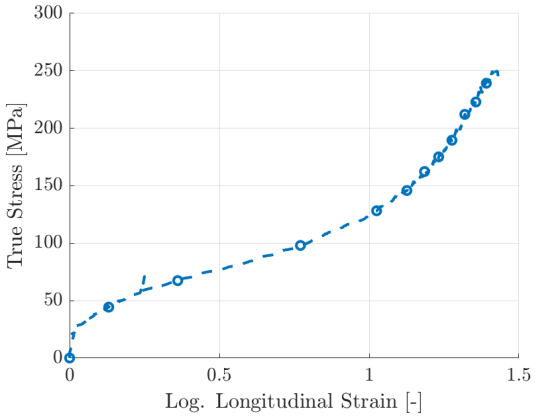

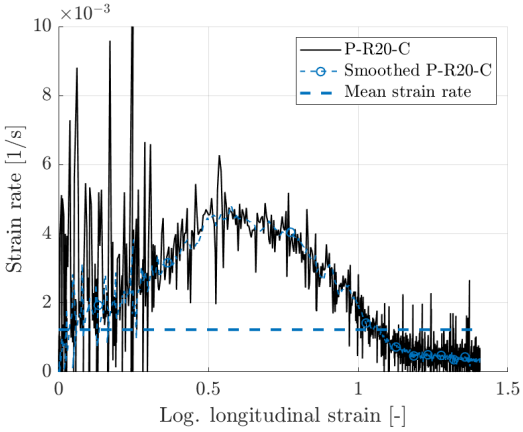

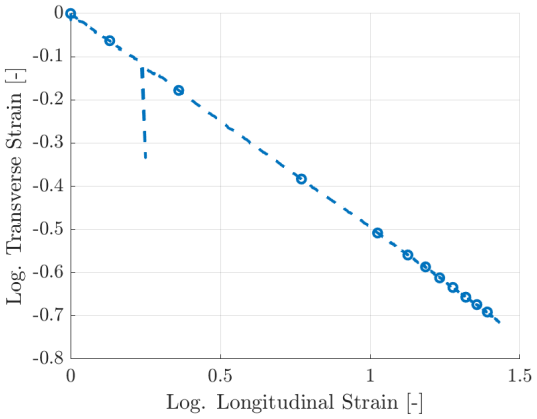

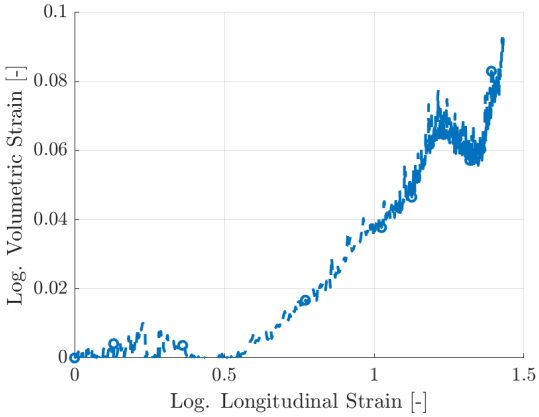

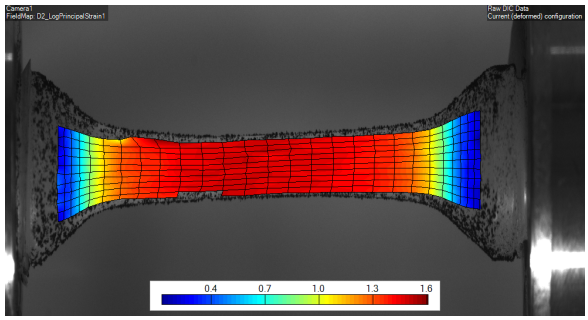

Figure A.17: Test results for specimen 17: P-R20-C

Table A.34: Material properties for specimen 17: P-R20-C

E	ν	σ_y	ε_y
1680.6 MPa	0.49	23 MPa	0.014

Results: 18 PW-R20-C

Table A.35: Test information for specimen 18: PW-R20-C

Test no.	Material	Load	Nominal strain-rate	Notch radius	Temp.
18	PW	Tension	10^{-3} s^{-1}	20 mm	-20 °C

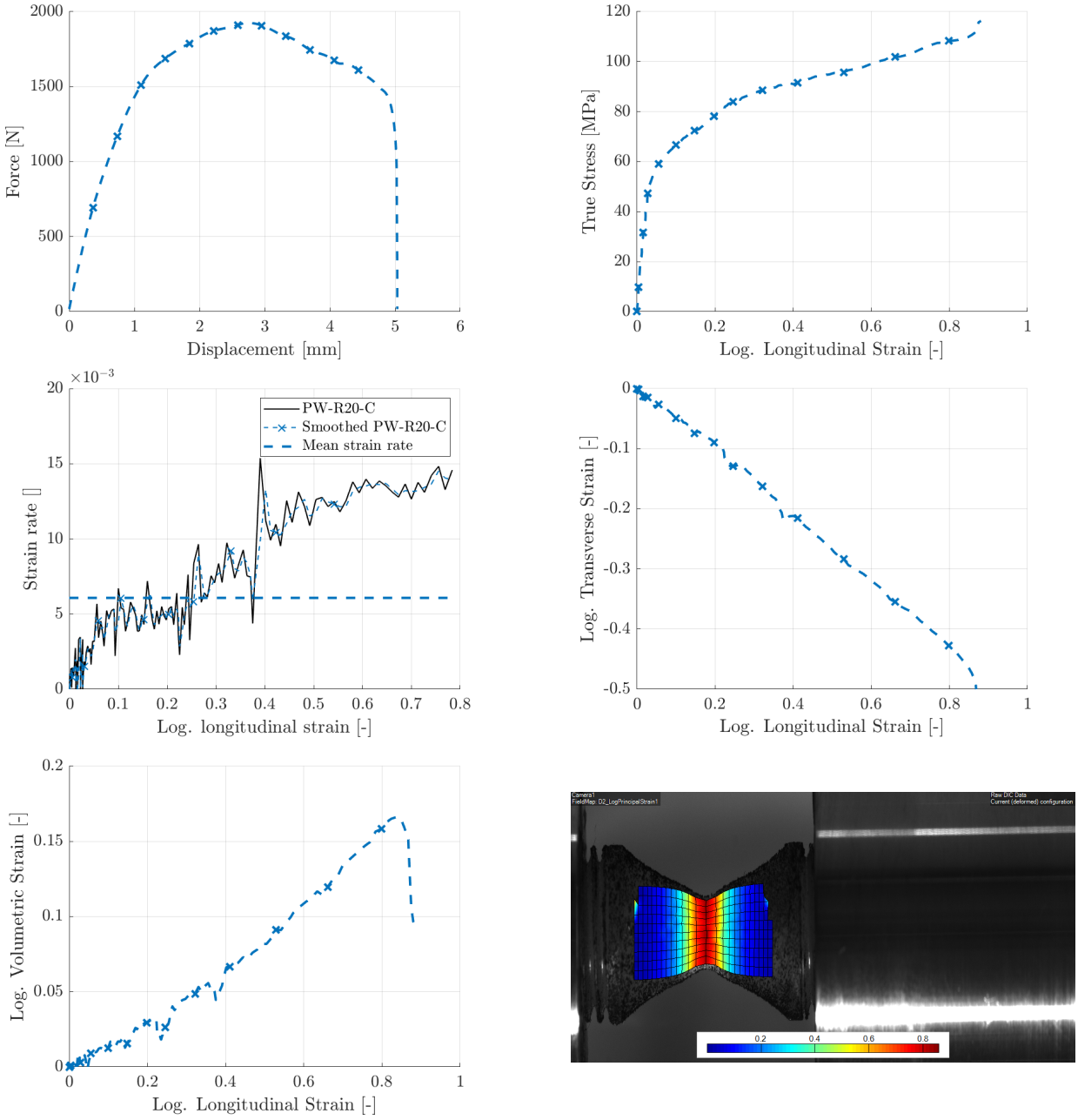

Figure A.18: Test results for specimen 18: PW-R20-C

Table A.36: Material properties for specimen 18: PW-R20-C

E	ν	σ_y	ε_y
1804.1 MPa	0.49	42 MPa	0.026

Results: 19 P-R2-H

Table A.37: Test information for specimen 19: P-R2-H

Test no.	Material	Load	Nominal strain-rate	Notch radius	Temp.
19	P	Tension	10^{-3} s^{-1}	2 mm	20 °C

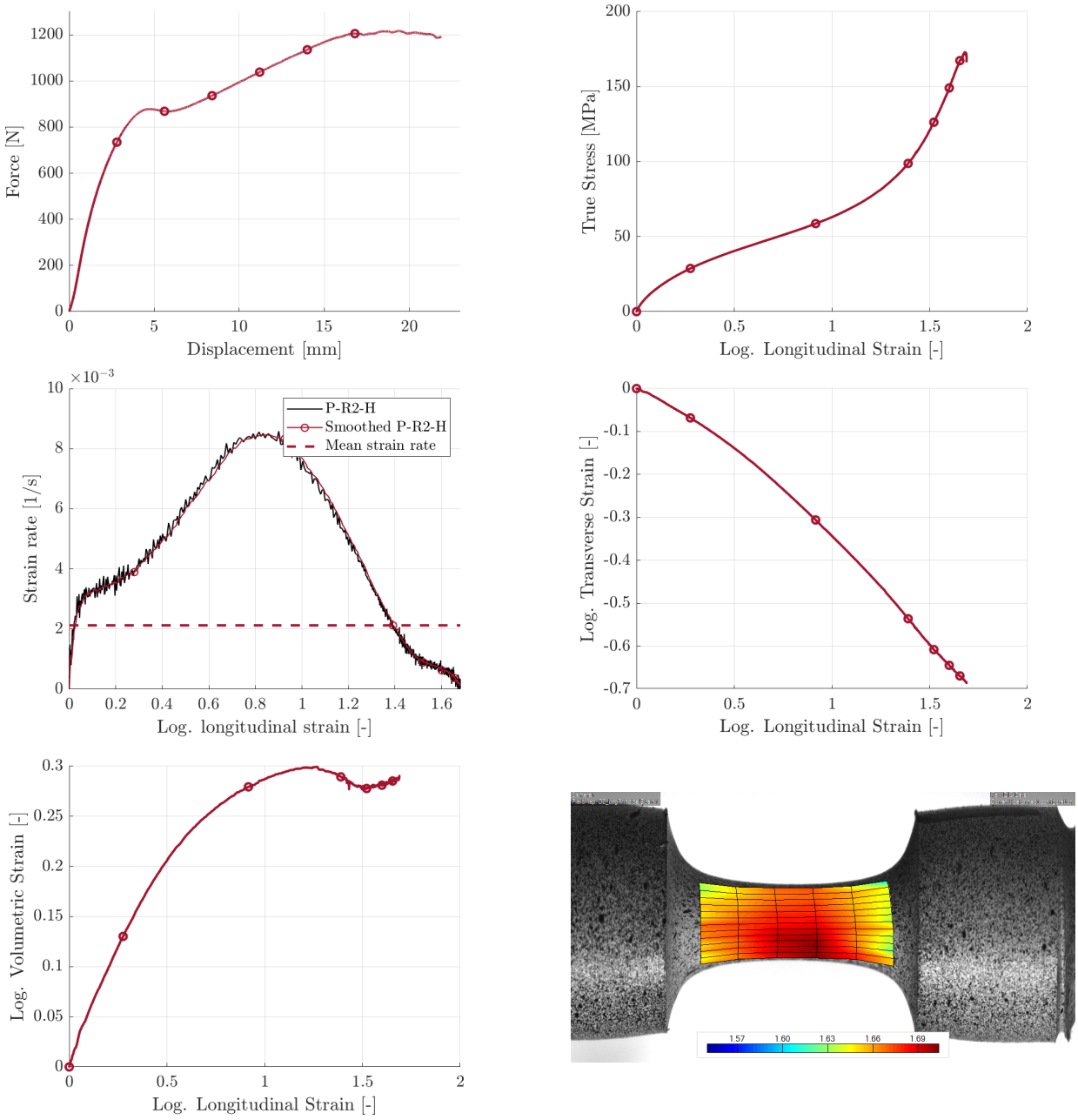

Figure A.19: Test results for specimen 19: P-R2-H

Table A.38: Material properties for specimen 19: P-R2-H

E	ν	σ_y	ε_y
257.0 MPa	0.2	5.5 MPa	0.024

Results: 20 PW-R2-H

Table A.39: Test information for specimen 20: PW-R2-H

Test no.	Material	Load	Nominal strain-rate	Notch radius	Temp.
20	PW	Tension	10^{-3} s^{-1}	2mm	20 °C

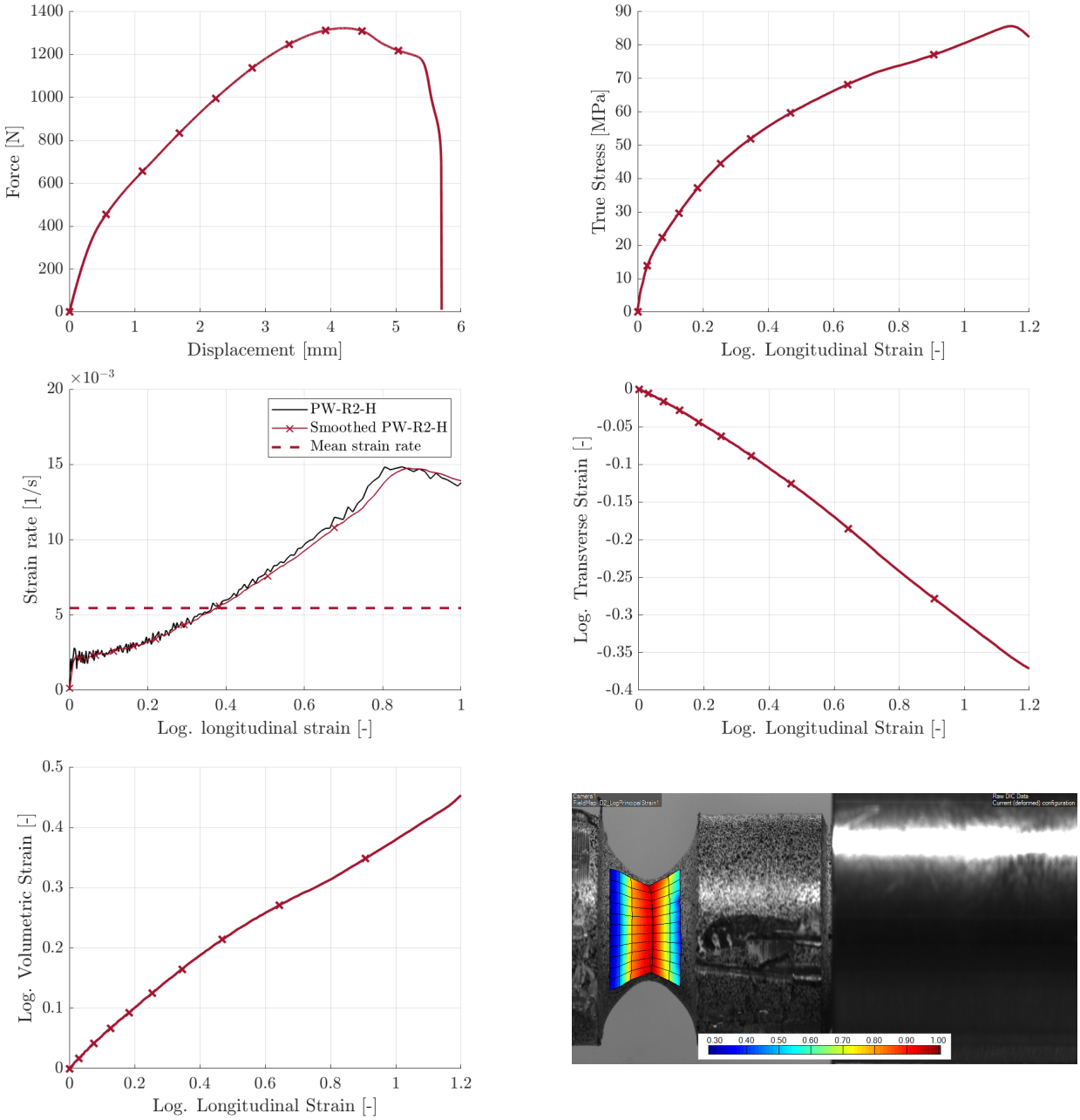

Figure A.20: Test results for specimen 20: PW-R2-H

Table A.40: Material properties for specimen 20: PW-R2-H

E	ν	σ_y	ε_y
535.1 MPa	0.2	13.3 MPa	0.028

Results: 21 W-R2-H

Table A.41: Test information for specimen 21: W-R2-H

Test no.	Material	Load	Nominal strain-rate	Notch radius	Temp.
21	W	Tension	10^{-3} s^{-1}	2 mm	20 °C

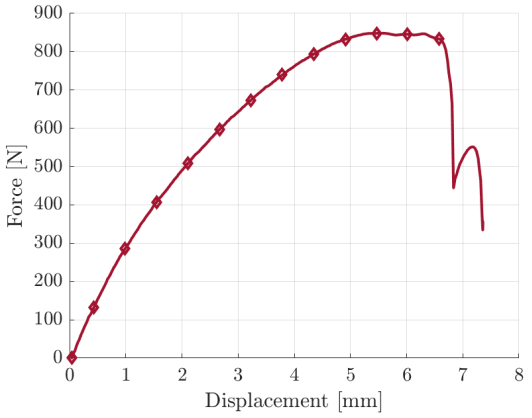

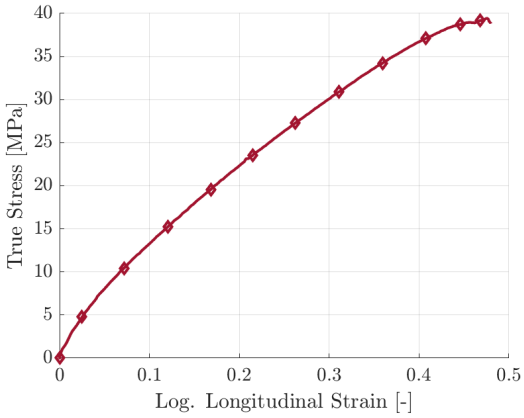

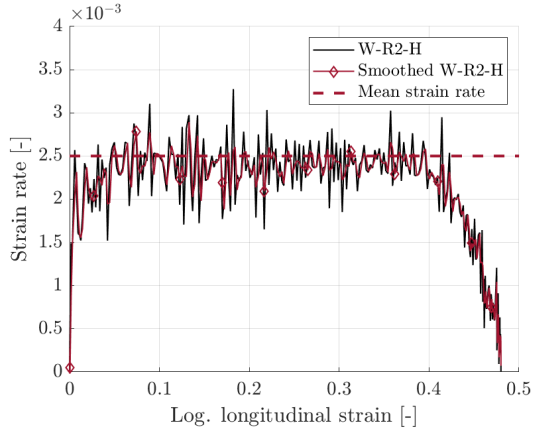

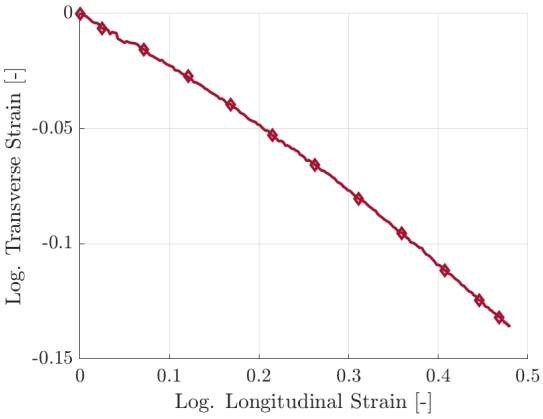

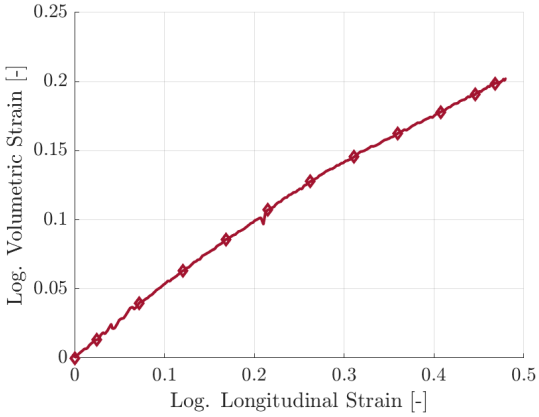

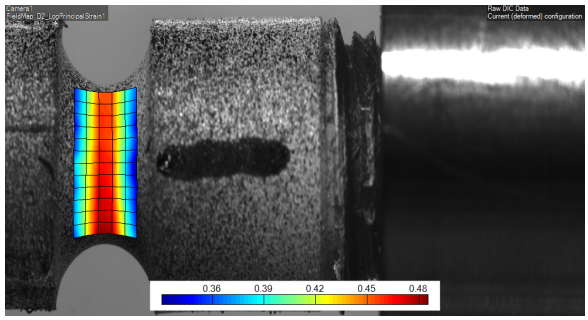

Figure A.21: Test results for specimen 21: W-R2-H

Table A.42: Material properties for specimen 21: W-R2-H

E	ν	σ_y	ε_y
196.0 MPa	0.2	5.9 MPa	0.033

Results: 22 P-R2-C

Table A.43: Test information for specimen 22: P-R2-C

Test no.	Material	Load	Nominal strain-rate	Notch radius	Temp.
22	P	Tension	10^{-3} s^{-1}	2 mm	-20 °C

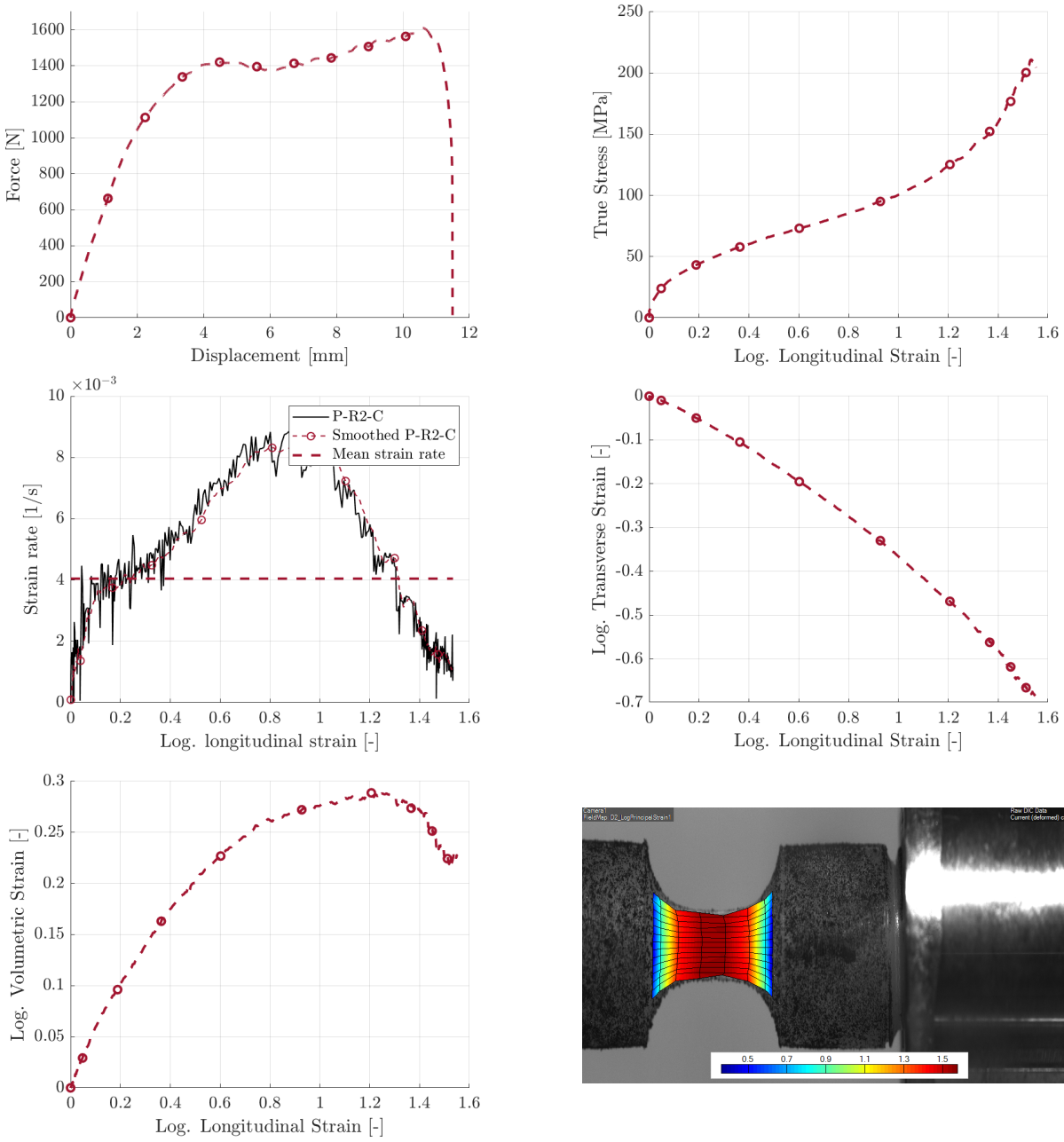

Figure A.22: Test results for specimen 22: P-R2-C

Table A.44: Material properties for specimen 22: P-R2-C

E	ν	σ_y	ε_y
548.7 MPa	0.2	14 MPa	0.0285

Results: 23 PW-R2-C

Table A.45: Test information for specimen 23: PW-R2-C

Test no.	Material	Load	Nominal strain-rate	Notch radius	Temp.
23	PW	Tension	10^{-3} s^{-1}	2 mm	-20 °C

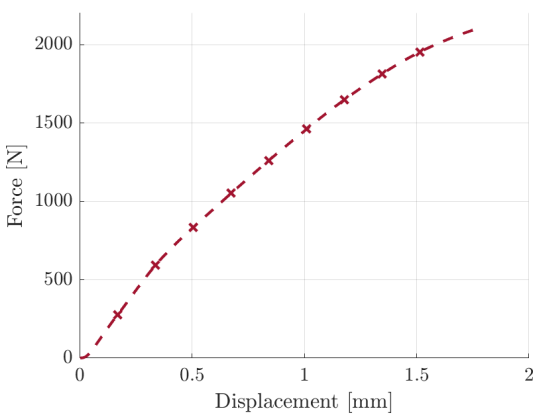

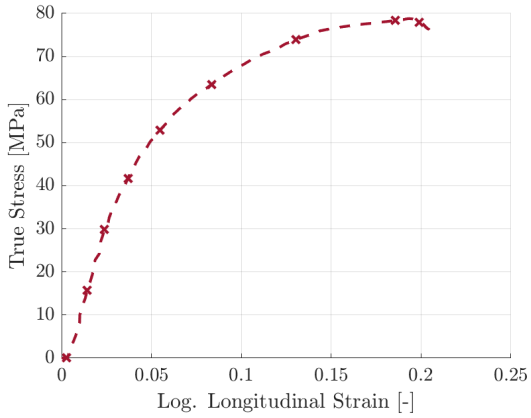

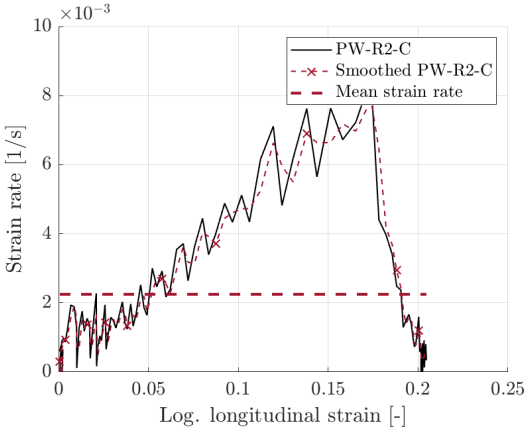

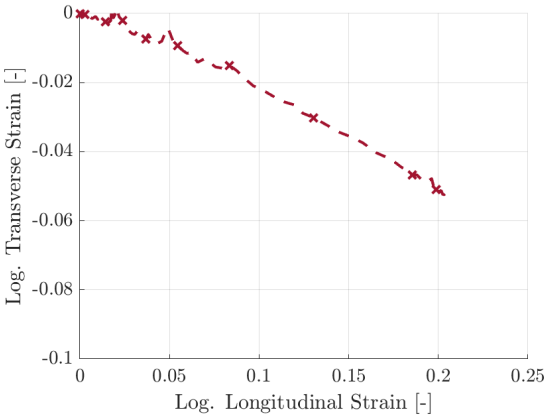

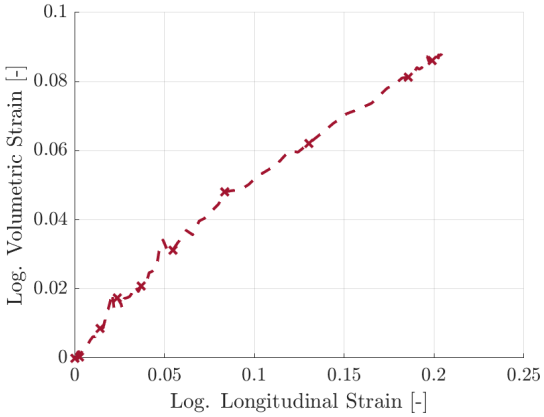

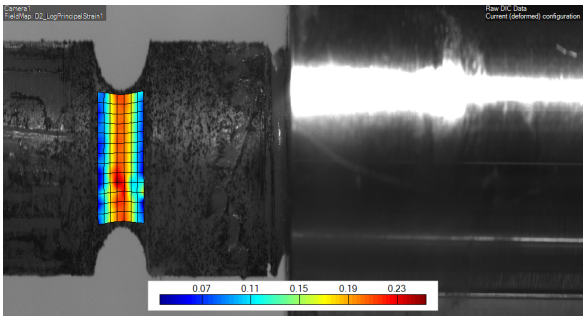

Figure A.23: Test results for specimen 23: PW-R2-C

Table A.46: Material properties for specimen 23: PW-R2-C

E	ν	σ_y	ε_y
1655 MPa	0.2	48 MPa	0.032

Results: 24 V-Cy-H

Table A.47: Test information for specimen 24: V-Cy-H

Test no.	Material	Load	Nominal strain-rate	Notch radius	Temp.
24	V	Compression	10^{-3} s^{-1}	-	20 °C

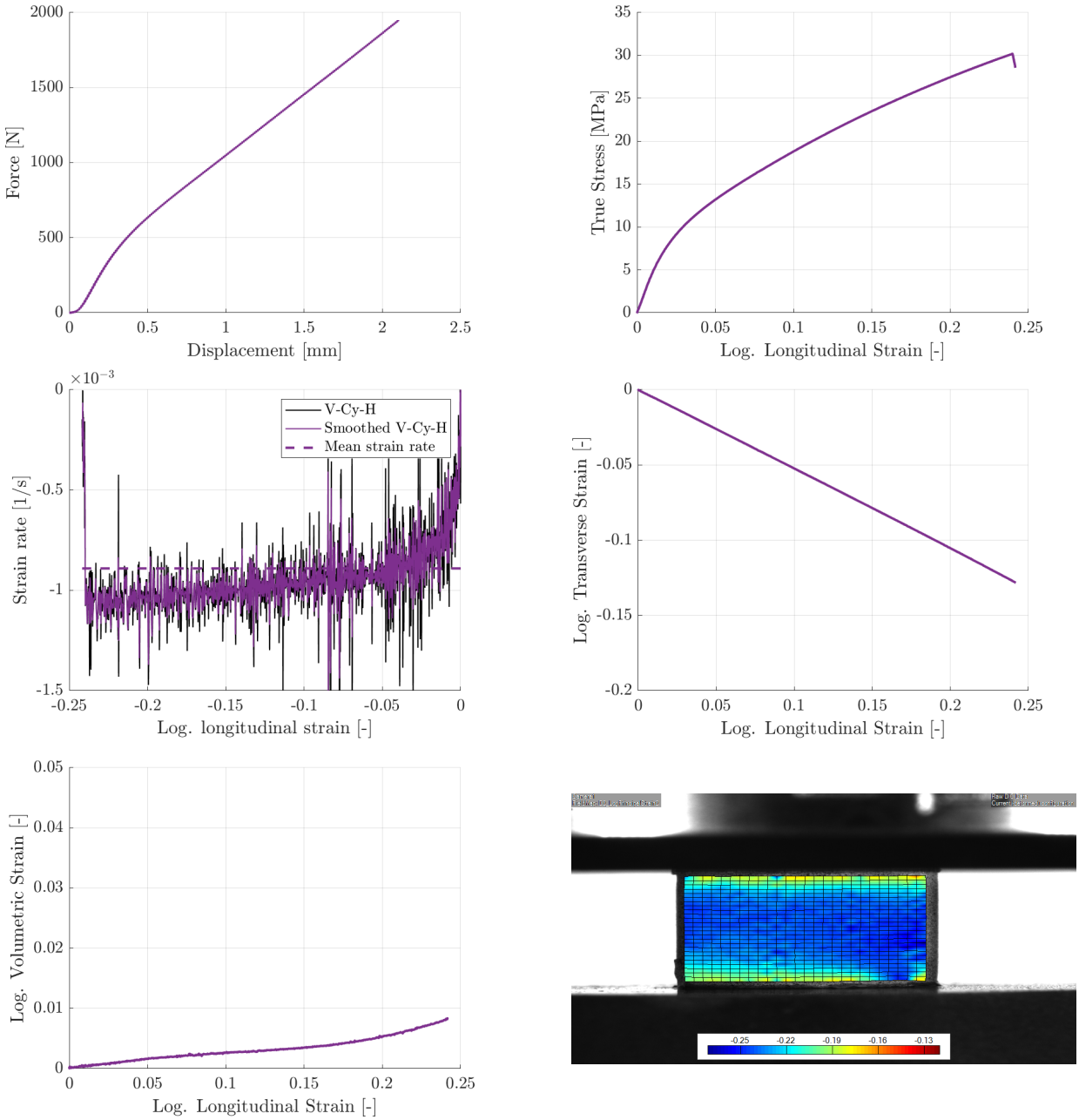

Figure A.24: Test results for specimen 24: V-Cy-H

Table A.48: Material properties for specimen 24: V-Cy-H

E	ν	σ_y	ε_y
464.5 MPa	0.5	7.8 MPa	0.0196

Results: 25 V-Cy-H

Table A.49: Test information for specimen 25: V-Cy-H

Test no.	Material	Load	Nominal strain-rate	Notch radius	Temp.
25	V	Compression	10^{-3} s^{-1}	-	20 °C

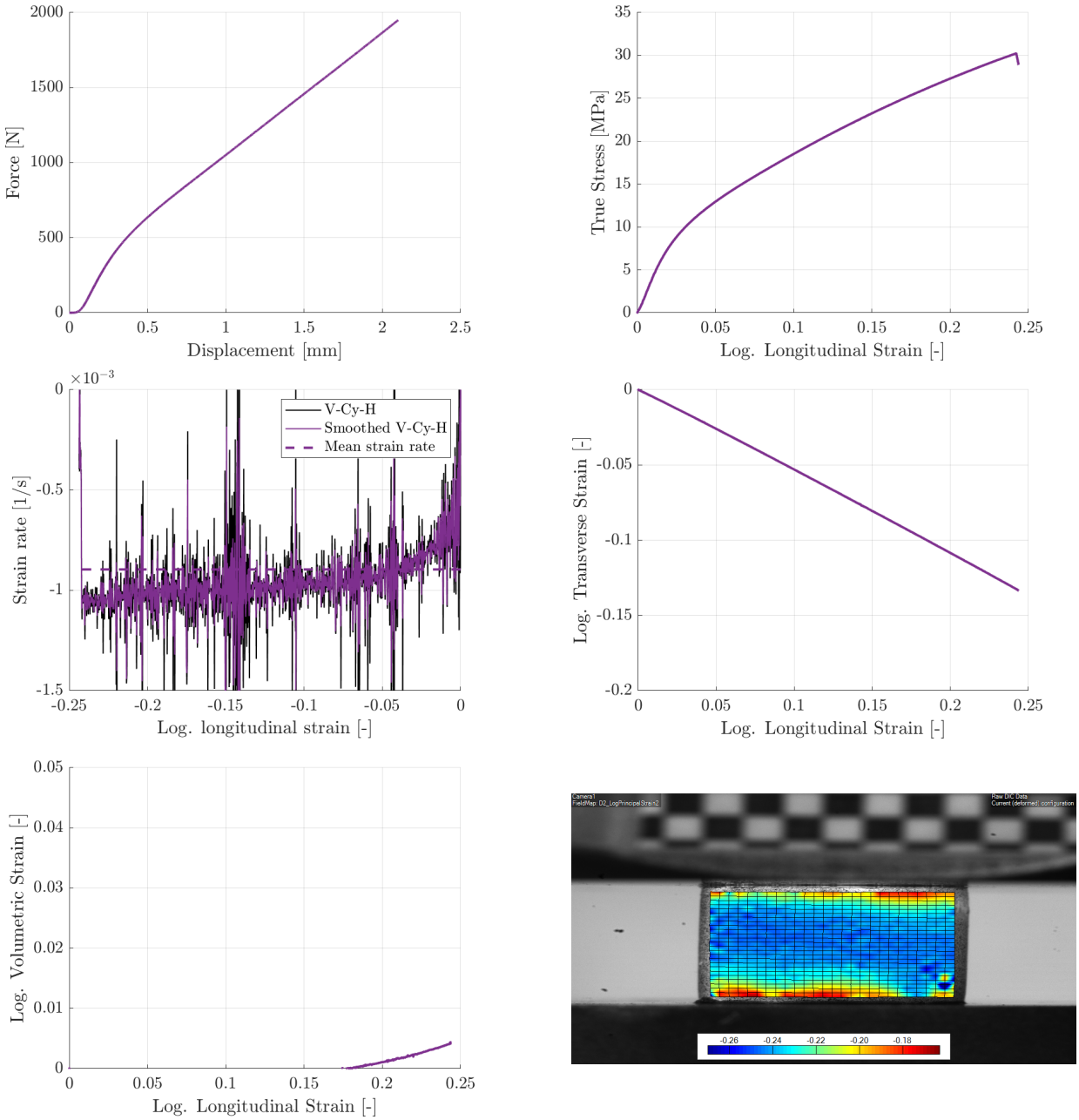

Figure A.25: Test results for specimen 25: V-Cy-H

Table A.50: Material properties for specimen 25: V-Cy-H

E	ν	σ_y	ε_y
416.7 MPa	0.5	8.39 MPa	0.023

Håkon Dahle and Ole Kristian Rønning

Thermomechanical Response of Virgin and Degraded PA11

NTNU
Norwegian University of
Science and Technology